A Technique for the Measurement of the Far-Infrared Radiative Properties of Metal and Superconducting Thin Films

by

Christopher Gregory Malone

Dip. Eng.
Saint Mary's University, Halifax, Nova Scotia (1987)

B. Eng., Mechanical Engineering
Technical University of Nova Scotia, Halifax, Nova Scotia (1990)

M. S., Mechanical Engineering
Massachusetts Institute of Technology, Cambridge, MA (1992)

Submitted to the Department of Mechanical Engineering
in Partial Fulfillment of the Requirements for the Degree of

DOCTOR OF PHILOSOPHY IN MECHANICAL ENGINEERING

at the

MASSACHUSETTS INSTITUTE OF TECHNOLOGY

September 1997

Signature of Author____
Department of Mechanical Engineering
September 1997

Certified by____
Professor Ernest G. Cravalho
Department of Mechanical Engineering
Thesis Supervisor

Accepted by____
Professor Ain A. Sonin
Department of Mechanical Engineering
Chairman, Graduate Committee

A Technique for the Measurement of the Far-Infrared Radiative Properties of Metal and Superconducting Thin Films

by

Christopher Gregory Malone

Submitted to the Department of Mechanical Engineering
on June 8, 1997 in partial fulfillment of the requirements for the
degree of Doctor of Philosophy in Mechanical Engineering

ABSTRACT

The absolute accuracy of reflectance measurements performed using Fourier-transform infrared (FT-IR) spectroscopy has been limited by standard single-reflection techniques to ±1% at best. This is primarily due to the photometric accuracy of the spectrometer and sample-positioning difficulties. Additionally, the absolute reflectance of the reference required for these techniques is typically not known to better than ±1%. The reflectance of materials such as metals and high-temperature superconductors approaches unity in the infrared, rendering standard techniques useless for the accurate measurement of this parameter. Accurate data are required to develop predictive models for the radiative properties of these materials which will be used to design devices exploiting their near-perfect reflectance.

Since the discovery of high-temperature superconductors, infrared spectroscopy has been used extensively to study these materials. Superconducting energy gaps may be discerned from changes in the dynamic conductivity caused by the condensation of charge carriers into superconducting electron pairs. The development of predictive models for the electromagnetic properties of high-temperature superconductors depends critically on the identification of the superconducting energy gap or gaps.

Further, accurate data for the infrared radiative properties of noble metals such as gold are required for the design of many applications, including infrared filters and optical components. There is a lack of such data, especially at cryogenic temperatures. Disagreements exist among previous experimental data, which may be attributed to the experimental technique or sample preparation.

High-accuracy reflectance measurements are performed on films of gold and (001)-orientation $YBa_2Cu_3O_7$ with an FT-IR spectrometer employing a silicon reflection Fabry-Pérot etalon as a multiple reflection technique for the spectral range from 400 to 100 cm^{-1} at cryogenic and room temperatures. This technique increases the measurement accuracy by one order of magnitude over single-reflection methods. Predictive models for the radiative properties of these materials are developed using these data. The performance of low-temperature radiation shields and far-infrared Fabry-Pérot resonators fabricated from $YBa_2Cu_3O_7$ are analyzed using a predictive model for the highest-quality materials presently available.

Thesis Supervisor: Ernest G. Cravalho
Title: Professor of Mechanical Engineering

To My Family,

Bernard, Carol Ann, Erin, and Ilie

ACKNOWLEDGMENTS

I would like to thank my advisor, Professor Ernie Cravalho, who has provided enthusiastic support and guidance throughout this endeavor. Thanks to Professor Joe Smith for advice and a home at the Cryogenic Engineering Laboratory. Dr. Alfredo Anderson provided valuable advice, critical experimental samples, and the use of his laboratory at Lincoln Laboratory.

Thanks to the technicians and fellow students at the Cryogenic Engineering Laboratory for help over the years. I would like to especially thank Leslie Regan at the Graduate Office of the Department of Mechanical Engineering and Professor Marcie Tyre of the Sloan School of Management for their kindness and help.

Bruker Instruments of Billerica, MA provided the experimental equipment and laboratory facilities which made this work possible. Dr. Thomas Tague was instrumental in establishing this collaboration and provided invaluable technical advice, along with support and friendship. Drs. Tim Johnson and Ralph Webber were critical to the success of this work. Thanks also to Dr. Dirk Laukien for providing support for this work and to the scores of other people at Bruker who helped me reach my goal.

Financial support came, in part, from the National Science Foundation, grant No. CTS-9007765, and the Natural Sciences and Engineering Research Council of Canada, through a Postgraduate Scholarship.

My mother, Carol Ann, father, Bernard, and sister, Erin, were, as always, a constant source of love, strength, and inspiration. Without the support of my family, I could not have reached this goal. My friends, especially Jeff Hebb, Jonathan Fox, and Darryl Gaines, provided many laughs and much encouragement.

Most importantly, thank you to my wife, Ilie, who has given me ceaseless love and encouragement over the past five years. You have given me so much. These few words cannot possibly capture the depth of my happiness at having you in my life.

TABLE OF CONTENTS

2. Theory of the Reflection Fabry-Pérot Etalon

3. Experimental Procedure

4. **Infrared Radiative Properties of Silicon**

5. **Infrared Radiative Properties of Gold**

6. **Infrared Radiative Properties of $YBa_2Cu_3O_7$**

6.3 Superconducting State Dielectric Function Models

6.7 Room-Temperature Experimental Results

6.8 Low-Temperature Experimental Results

7. Low-Temperature Radiation Shielding Fabricated from $YBa_2Cu_3O_7$

7.3 Dielectric Function Tensor Model for Superconducting $YBa_2Cu_3O_7$

8. Fabry-Pérot Resonators Fabricated from $YBa_2Cu_3O_7$

9. Summary and Future Work

LIST OF FIGURES

LIST OF TABLES

CHAPTER 1

INTRODUCTION

Radiation shields and Fabry-Pérot resonators are two important applications exploiting the near-unity reflectance of high-T_c superconducting films in the far-infrared spectral region. A quantitative assessment of the feasibility of these applications requires accurate knowledge of the material optical constants. This work investigates an experimental technique which enables the determination of these properties: the silicon reflection Fabry-Pérot etalon. This technique increases the measurement sensitivity by one order of magnitude over conventional methods.

According to the Bardeen-Cooper-Schrieffer (BCS) theory of superconductivity, a superconductor absorbs only photons possessing an energy greater than the energy gap between the normal and superconducting electron energy bands (Rose-Innes and Rhoderick, 1978). Cryogenic thermal radiation shields fabricated from high-T_c superconductors promise superior performance over existing shield materials because the energy-gap wavelength of these materials is short compared to the wavelength of maximum emissive power at temperatures below 30 K. For incident radiation wavelengths longer than the energy-gap wavelength, the reflectance of a superconductor is close to unity. The high-T_c superconductor is able to reflect a large portion of the low-temperature radiative energy providing highly effective radiation shields.

Far-infrared Fabry-Pérot resonators fabricated from high-T_c superconducting films also benefit from the near-perfect reflectance of the material. As the reflectance of the films approaches unity, the performance of the resonator improves. The reflectance of $YBa_2Cu_3O_7$ exceeds that of existing materials in the far-infrared spectral region, and so, a resonator fabricated from $YBa_2Cu_3O_7$ promises to offer better performance characteristics than existing devices.

There is also a lack of accurate data for the infrared radiative properties of metals such as gold, especially at cryogenic temperatures. The optical properties of metal films are required for the design of many applications, including infrared filters and optical components. The technique investigated here enables the accurate measurements of these properties, which is useful for engineering design and for theoretical work describing the absorption of electromagnetic radiation by metals.

The absolute accuracy of reflectance measurements performed using Fourier-transform infrared (FT-IR) spectroscopy has been limited by standard single-reflection techniques to ±1% at best. This is primarily due to the photometric accuracy of the spectrometer and sample-positioning difficulties. Additionally, the absolute reflectance of the reference required for these techniques is typically not known to better than ±1%. The reflectance of materials such as metals and high-temperature superconductors approaches unity in the infrared, rendering standard techniques useless for the accurate measurement of this parameter.

In this work, thin-film optics is employed to describe the reflectance of an ideal silicon-on-sample reflection Fabry-Pérot etalon. From this analysis, the absorptance of the sample is extracted. Departures from the analytical solution caused by surface roughness, deviations from parallelism, air gaps, etc., are considered and shown to be small for this experimental investigation. A method is presented for extracting meaningful absorptance data from experimental reflectance data badly skewed by sample-reference interchange difficulties. The radiative properties of the silicon etalon used in this work are characterized to determine the appropriateness of simplifications to the thin-film optics analysis.

Experimental measurements for the absorptance of gold films at room-temperature and 6 K are presented for the spectral range from 400 to 100 cm^{-1}. The 6 K data are the first available for the far-infrared spectral range. Predictive models are recommended based on a comparison with these data.

Finally, the absorptance of $YBa_2Cu_3O_7$ films at 6 K are measured for the spectral range from 400 to 100 cm^{-1}. These data are compared with the limited set of high-accuracy absorptance data available for this material. A predictive model for the data presented here is developed within the theoretical framework of the BCS theory of superconductivity.

CHAPTER 2

THEORY OF THE REFLECTION FABRY-PÉROT ETALON

2.1 Introduction

The infrared reflectance of a specular material is typically measured by reflecting infrared radiation off the surface of a sample and measuring the response of a detector. A reference is then placed in the same location and the detector response is re-measured. The ratio of these two responses is the reflectance. However, this 'single-bounce' technique suffers from sample and reference positioning errors, photometric error, lack of knowledge of the absolute reflectance of the reference, etc. As a result, the single-bounce technique enables the reflectance to be measured with an accuracy of ± 1%. When the material reflectance exceeds 99%, the single-bounce technique is ineffective at measuring this parameter.

The silicon reflection Fabry-Pérot etalon measurement technique overcomes the limitations of the single-bounce technique. Infrared radiation incident upon the stack suffers multiple reflections inside a transparent silicon layer. The resultant reflectance of the structure yields a series of resonance fringes. By applying thin-film optics to describe the propagation of the electromagnetic waves inside the stack, the radiative properties of the sample may be determined from the measured reflectance fringes with an accuracy approximately one order of magnitude better than with the single-bounce technique.

In this chapter, thin-film optics theory is applied to the silicon reflection Fabry-Pérot etalon structure and an approximate prediction for the absorptance of the sample layer is developed. An error analysis is applied to this prediction yielding an error estimate for the experimental measurements presented in this following chapters. Deviations from this prediction caused by air gaps between the sample and silicon etalon, surface roughness, departure from plane-parallelism, and the lack of a collimated infrared beam are also considered.

2.2 Theory

The ideal Fabry-Pérot etalon has been treated in many optics textbooks (Born and Wolf, 1980; Hecht and Zajac, 1974). Reflection Fabry-Pérot etalons have been studied extensively by Holden (1949) and Tolansky (1948). This analysis follows the approach of Genzel and coworkers (Genzel et al., 1993; Genzel et al., 1991).

The silicon reflection Fabry-Pérot etalon shown in Fig. 2.1 consists of a stack of a silicon layer and an opaque thin film deposited on a substrate. In this work, the thin film is either gold or $YBa_2Cu_3O_7$. The silicon is cut from a 2" diameter wafer of double-side polished (111) *n*-type silicon, 127±0.05 μm in thickness with a resistivity of 33.5±3.3 Ω-cm. The stack is roughly square, with lateral dimensions of approximately 10 mm. The wafer and film are pressed together and the stack is mounted between two 1/16-inch OFHC copper plates. On the silicon side, the copper plate has a 8 mm diameter center hole which exposes the stack to the FT-IR infrared beam. For low-temperature experiments, the assembly is fixed to the cold finger of the cryostat by four spring-loaded screws. Further details on the preparation of the stack are given in Chapter 3.

The theoretical analysis presented here is based on thin-film optics. Perfectly flat and plane-parallel surfaces are assumed. The interface between the $YBa_2Cu_3O_7$ or gold film and the silicon is assumed to be perfect. Departures from these ideal conditions are considered in Sections

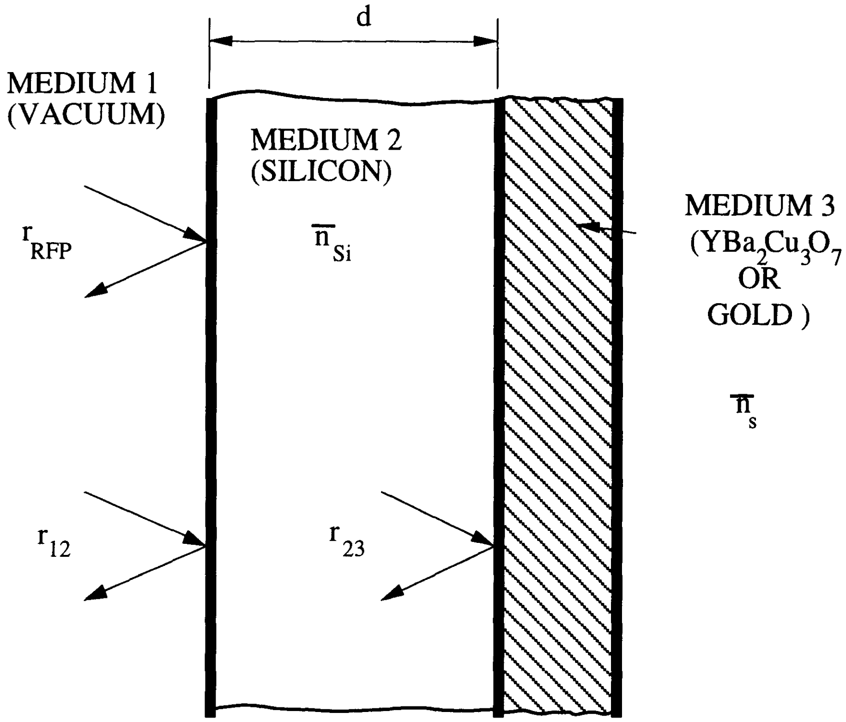

Figure 2.1 The silicon reflection Fabry-Pérot etalon.

2.6 and 2.7. These sections will show that the idealized analysis describes the actual experiment within the experimental error.

The expression for the reflection coefficient of the silicon reflection Fabry-Pérot etalon is derived by the summation of the amplitudes of successive reflections and refractions at the silicon-vacuum interface. The infrared beam is assumed to be collimated and vertically incident. The electromagnetic wave is assumed to be totally coherent in the second medium, the silicon wafer, and the third medium, the sample film, is assumed to be opaque. Consider a beam incident from the left of Fig. 2.1. The incident beam is partially reflected and partially transmitted at the first interface. The transmitted part is subsequently reflected back and forth between the first and second interfaces. At each interface, a portion of the incident energy is transmitted into the adjacent medium and the remainder is reflected. The etalon reflection coefficient, r_{RFP}, is obtained by adding the amplitudes of the successive reflected and transmitted rays, including the complex phase difference, $\bar{\phi}$, which accounts for the geometric path difference between any two successive reflected and transmitted rays,

$$r_{\mathrm{RFP}}(\nu) = \sqrt{R_{\mathrm{RFP}}}\, e^{i\phi_{\mathrm{RFP}}} = \frac{r_{12} + r_{23}\, e^{2i\bar{\phi}}}{1 + r_{12}\, r_{23}\, e^{2i\bar{\phi}}} \tag{2.1}$$

where R_{RFP} is the etalon reflectance, ϕ_{RFP} is the etalon phase change on reflection, r_{12} is the Fresnel amplitude reflection coefficient for the vacuum-silicon interface, and r_{23} is the Fresnel amplitude reflection coefficient for the silicon-sample interface.

The complex phase difference, $\bar{\phi}$, is defined as:

$$\bar{\phi} = 2\pi\nu\bar{n}_{\mathrm{Si}}d \tag{2.2}$$

where ν is the frequency, $\bar{n}_{\mathrm{Si}} = n_{\mathrm{Si}} + i\kappa_{\mathrm{Si}}$ is the complex index of refraction of the silicon wafer, labeled medium 2 in Fig. 2.1, n_{Si} is the index of refraction, κ_{Si} is the extinction coefficient, and d is the silicon wafer thickness.

For normal incidence, the *s*- and *p*-wave polarization reflectances at the interface between two isotropic media are identical. Following the Muller convention (Muller, 1969) for the coordinate system used for the derivation of the Fresnel reflection coefficients, the phase change on reflection appears to differ by 180° between the two polarizations. This is an artifact of the convention; their physical behavior is identical. The phase change on reflection is identified with the *s*-wave polarization in this analysis.

The Fresnel amplitude reflection coefficients r_{12} and r_{23} may be written as:

$$r_{12} = |r_{12}| e^{i\phi_{12}} = \sqrt{R_{12}}\, e^{i\phi_{12}} \tag{2.3}$$

$$r_{23} = |r_{23}| e^{i\phi_{23}} = \sqrt{R_{23}}\, e^{i\phi_{23}} \tag{2.4}$$

where $|r_{12}|$ and $|r_{23}|$ are the magnitudes of the reflection coefficients and $\sqrt{R_{12}}$ and $\sqrt{R_{23}}$ are the reflectance values at the respective interfaces.

Substituting Eqs. (2.2), (2.3), and (2.4) into Eq. (2.1) and taking $R_{\mathrm{RFP}} = |r_{\mathrm{RFP}}|^2$ yields:

$$R_{\mathrm{RFP}}(\nu) = |\mathrm{r}_{\mathrm{RFP}}|^2 = \frac{R_{12} + K^2 R_{23} + 2K\sqrt{R_{12}R_{23}}\cos(2\phi + \phi_{23} - \phi_{12})}{1 + K^2 R_{12} R_{23} + 2K\sqrt{R_{12}R_{23}}\cos(2\phi + \phi_{23} + \phi_{12})} \tag{2.5}$$

where $\phi = 2\pi\nu n_{\mathrm{Si}} d$ is the real component of the complex phase difference $\bar{\phi}$, and $K = \exp[-4\pi\nu\,\kappa_{\mathrm{Si}}\, d]$ accounts for the damping of the wave as it is travels back and forth across the silicon wafer.

At the interface between a non-absorbing medium, $\kappa = 0$, and vacuum, the phase change upon reflection for the *s*-wave polarization is $-\pi$. The phase change upon reflection for the *s*-wave polarization at the interface between two absorbing media is given by (Bennett, 1995):

$$\tan(\phi_{\mathrm{ij}} + \pi) = \frac{2(n_{\mathrm{j}}k_{\mathrm{i}} - n_{\mathrm{i}}k_{\mathrm{j}})}{n_{\mathrm{i}}^2 - n_{\mathrm{j}}^2 + k_{\mathrm{i}}^2 - k_{\mathrm{j}}^2} \tag{2.6}$$

where the reflected beam originates in medium i, with a complex index of refraction of $\bar{n}_i = n_i + i\kappa_i$ and the second medium j has a complex index of refraction of $\bar{n}_j = n_j + i\kappa_j$,

Considering the finite extinction coefficient of the silicon, κ_{Si}, the phase change upon reflection at the vacuum-silicon interface, ϕ_{12} is given by:

$$\tan(\phi_{12} + \pi) = \frac{-2n_1k_{Si}}{n_1^2 - n_{Si}^2 - k_{Si}^2} \tag{2.7}$$

where n_1 is the index of refraction of medium 1, the vacuum space.

For the spectral range where the reflection Fabry-Pérot is employed, ~400-100 cm^{-1}, the absorptance of high-resistivity silicon is small. There is a multiphonon absorption band centered at ~600 cm^{-1}. The wing of this band contributes a nearly negligible absorptance for wavenumbers below 400 cm^{-1} (Johnson, 1959). Experimental measurements presented in Chapter 4 show this to be true for the silicon used in this work. As a result, $\phi_{12} \approx -\pi$ and Eq. (2.3) may be approximated as,

$$r_{12} \approx -\sqrt{R_{12}} \tag{2.8}$$

Substituting $\phi_{12} \approx -\pi$ and Eq. (2.8) into Eq. (2.5),

$$R_{RFP}(\nu) = |r_{RFP}|^2 = \frac{R_{12} + K^2 R_{23} - 2K\sqrt{R_{12}R_{23}}\cos(2\phi + \phi_{23})}{1+K^2 R_{12} R_{23} - 2K\sqrt{R_{12}R_{23}}\cos(2\phi + \phi_{23})} \tag{2.9}$$

Sharp reflectance minima R_{RFP0}, or absorptance maxima, A_{RFP0}, occur at resonance when

$$2\phi + \phi_{23} = m \cdot 2\pi \tag{2.10}$$

where m = 0,1,2,3... is the order of interference. It is equal to the equivalent path difference, measured in wavelengths, between two successive beams. The resonance frequencies are given by:

$$\nu_m = \frac{1}{2n_{Si}d}\left(m - \frac{1}{2\pi}\phi_{23}\right) \tag{2.11}$$

Since medium 3, the sample layer, is opaque, $A_{\mathrm{RFP0}} = 1 - R_{\mathrm{RFP0}}$. The maximum absorptance is:

$$A_{\mathrm{RFP0}} = \frac{(1-R_{12})(1-K^2 R_{23})}{\left(1-K\sqrt{R_{12}R_{23}}\right)^2} \tag{2.12}$$

When the absorptance of the silicon is small, the magnitude of A_{RFP0} is determined mostly by the absorptance of the superconducting sample layer. Writing the frequency-dependent absorptance in terms of A_{RFP0},

$$A_{\mathrm{RFP}}(\nu) = 1 - R_{\mathrm{RFP}}(\nu) = \frac{A_{\mathrm{RFP0}}}{1+F\sin^2\left(\frac{1}{2}(2\phi+\phi_{23})\right)} \tag{2.13}$$

where F is the coefficient of finesse,

$$F = \frac{4\sqrt{K^2 R_{12}R_{23}}}{\left(1-\sqrt{K^2 R_{12}R_{23}}\right)^2} \tag{2.14}$$

The term,

$$\frac{1}{1+F\sin^2\left(\frac{1}{2}(2\phi+\phi_{23})\right)} \tag{2.15}$$

in Eq. (2.13) is the familiar Airy function.

Another quantity of interest is the reflectivity finesse, $\mathfrak{F}$, a measure of the sharpness of the interference fringes. It is the ratio of the free spectral range, which is the separation between adjacent orders of interference, to the fringe width at half-intensity,

$$\mathfrak{F} = \frac{\pi\sqrt{F}}{2} = \frac{\pi\sqrt[4]{K^2 R_{12}R_{23}}}{1-\sqrt{K^2 R_{12}R_{23}}} \tag{2.16}$$

Equation (2.12) may be written in terms of the minimum reflectance R_{RFP0} to solve for $K\sqrt{R_{23}}$:

$$K\sqrt{R_{23}} = \frac{\sqrt{R_{\mathrm{RFPO}}} + \sqrt{R_{12}}}{1 + \sqrt{R_{\mathrm{RFPO}} R_{12}}} \tag{2.17}$$

Substituting for $K\sqrt{R_{23}}$ allows the reflectivity finesse, Eq. (2.16), to be written in terms of the experimentally measured quantities $\sqrt{R_{\mathrm{RFPO}}}$ and $\sqrt{R_{12}}$:

$$\Im = \frac{\pi\sqrt[4]{R_{12}}\sqrt{\sqrt{R_{\mathrm{RFPO}}} + \sqrt{R_{12}}}\sqrt{1 + \sqrt{R_{\mathrm{RFPO}} R_{12}}}}{1 - R_{12}} \tag{2.18}$$

The Fresnel reflection coefficient at the interface between the sample from the etalon stack and vacuum is:

$$r_s = \frac{1 - \bar{n}_s}{1 + \bar{n}_s} \tag{2.19}$$

where $\bar{n}_s$ is the complex refractive index of the sample.

The Fresnel reflection coefficients for the reflection Fabry-Pérot etalon vacuum-silicon interface r_{12} and the silicon-sample interface r_{23} are:

$$r_{12} = \frac{n_1 - \bar{n}_{\mathrm{si}}}{n_1 + \bar{n}_{\mathrm{si}}} \tag{2.20}$$

$$r_{23} = \frac{\bar{n}_{\mathrm{si}} - \bar{n}_s}{\bar{n}_{\mathrm{si}} + \bar{n}_s} \tag{2.21}$$

Substituting Eqs. (2.20) and (2.21) into Eq. (2.19) gives:

$$r_s = \frac{r_{12} + r_{23}}{1 + r_{12} r_{23}} \tag{2.22}$$

Substituting Eqs. (2.3), and (2.4) for r_{12} and r_{23}, respectively, into Eq. (2.22) gives:

$$R_s(\nu) = |\mathrm{r}_s|^2 = \frac{R_{12} + R_{23} + 2\sqrt{R_{12} R_{23}}\cos(\phi_{23} - \phi_{12})}{1 + R_{12} R_{23} + 2\sqrt{R_{12} R_{23}}\cos(\phi_{23} + \phi_{12})} \tag{2.23}$$

As mentioned above, the absorptance in the silicon film is very small, so from Eq. (2.7), $\phi_{12} \approx -\pi$. With this approximation, Eq. (2.23) reduces to:

$$R_s(\nu)=|r_s|^2=\frac{R_{12}+R_{23}-2\sqrt{R_{12}R_{23}}\cos(\phi_{23})}{1+R_{12}R_{23}-2\sqrt{R_{12}R_{23}}\cos(\phi_{23})} \tag{2.24}$$

The absorptance of the opaque sample is:

$$A_s(\nu)=1-R_s(\nu)=\frac{(1\text{-}R_{12})(1-R_{23})}{\left(1+\sqrt{R_{12}R_{23}}\right)^2-4\sqrt{R_{12}R_{23}}\cos^2\left(\frac{\phi_{23}}{2}\right)} \tag{2.25}$$

Equation (2.17) is employed to rewrite Eq. (2.25) in terms of the experimentally measured quantities R_{RFP0} and R_{12}, K, and ϕ_{23}. The absorptance of the sample at the resonance frequencies for the etalon is:

$$A_s(\nu_{\mathrm{RFP0}})=\frac{(1\text{-}R_{12})\left(K^2\left(1+\sqrt{R_{\mathrm{RFP0}}R_{12}}\right)^2-\left(\sqrt{R_{\mathrm{RFP0}}}+\sqrt{R_{12}}\right)^2\right)}{\left[\begin{array}{l}\left(K\left(1+\sqrt{R_{\mathrm{RFP0}}R_{12}}\right)+\sqrt{R_{12}}\left(\sqrt{R_{\mathrm{RFP0}}}+\sqrt{R_{12}}\right)\right)^2\\ -4K\sqrt{R_{12}}\left(\sqrt{R_{\mathrm{RFP0}}}+\sqrt{R_{12}}\right)\left(1+\sqrt{R_{\mathrm{RFP0}}R_{12}}\right)\cos^2\left(\frac{\phi_{23}}{2}\right)\end{array}\right]} \tag{2.26}$$

In the spectral range investigated in this experiment, $K \approx 1$ and $\phi_{23} \approx -\pi$ for most metals and superconductors. With these approximations, Eq. (2.26) reduces to:

$$A_s(\nu_{\mathrm{RFP0}})=\frac{(1\text{-}R_{12})^2(1-R_{\mathrm{RFP0}})}{\left(1+2\sqrt{R_{\mathrm{RFP0}}R_{12}}+R_{12}\right)^2} \tag{2.27}$$

The minimum absorptance A_{RFPmin} occurs between resonance peaks, i.e., $2\phi+\phi_{23}=m\cdot 2\pi\pm\pi$. From Eq. (2.13), A_{RFPmin} may be written as:

$$A_{\mathrm{RFP\,min}}=A_{\mathrm{RFP0}}\frac{\left(1-\sqrt{K^2R_{12}R_{23}}\right)^2}{\left(1+\sqrt{K^2R_{12}R_{23}}\right)^2} \tag{2.28}$$

Comparing Eq. (2.5), the expression for the reflectance of the reflection Fabry-Pérot etalon $R_{\mathrm{RFP0}}(\nu)$, to Eq. (2.24), the expression for the reflectance of the sample $R_s(\nu)$, gives:

$$\frac{R_{\mathrm{RFP}}(\nu)}{R_{\mathrm{s}}(\nu)} = \frac{\dfrac{R_{12} + K^2 R_{23} + 2K\sqrt{R_{12}R_{23}}\cos(2\phi + \phi_{23} - \phi_{12})}{1+K^2 R_{12} R_{23} + 2K\sqrt{R_{12}R_{23}}\cos(2\phi + \phi_{23} + \phi_{12})}}{\dfrac{R_{12} + R_{23} - 2\sqrt{R_{12}R_{23}}\cos(\phi_{23})}{1+R_{12} R_{23} - 2\sqrt{R_{12}R_{23}}\cos(\phi_{23})}} \tag{2.29}$$

If the assumptions that $K \approx 1$, $\phi_{12} \approx -\pi$, and $\phi_{23} \approx -\pi$ are valid, Eq. (2.29) reduces to unity at the resonance maxima. The reflectance maxima equal the sample reflectance, $R_{\mathrm{RFP}}(\nu_{\mathrm{RFPmin}}) = R_{\mathrm{s}}(\nu_{\mathrm{RFPmin}})$.

2.3 Validity of Assumptions for the Reflection Fabry-Pérot Etalon Theory

Verification of the assumption that $\phi_{12} \approx -\pi$ and $K \approx 1$ requires the complex refractive index of the silicon used in this work. Chapter 4 analyses the optical properties of this silicon at length. This analysis determines an index of refraction of 3.42 and an absorption coefficient $\alpha = 4\pi\nu\kappa_{\mathrm{Si}} = 0.20$ cm^{-1} for the spectral range from 400 to 100 cm^{-1}.

Using these data in Eq. (2.7), the phase change upon reflection at the vacuum-silicon interface, ϕ_{12} is almost exactly -180°. Thus, the term $e^{i\phi_{12}}$ from Eq. (2.3) is very closely approximated by -1.

The term $K = \exp[-4\pi\nu\,\kappa_{\mathrm{Si}}\,d] = \exp[-\alpha d]$ which accounts for the damping of the wave as it is reflected back and forth across the silicon wafer decreases from unity as the absorption coefficient increases from zero. For $\alpha = 0.20$ cm^{-1}, $K \approx 0.9999$. Examining Eq. (2.26), it is evident that for the silicon used in this work, the approximation $K = 1$ is valid.

To estimate the phase change upon reflection at the silicon-sample interface, ϕ_{23}, requires the complex refractive index of the sample in addition to $\bar{n}_{\mathrm{Si}}$. For the estimate, a room-temperature gold film is used as the sample. Predictive models for the complex refractive index of gold as a function of temperature are presented in Chapter 5. The absorptance of gold is largest at room temperature and decreases with temperature, resulting in an increasing extinction coefficient with decreasing temperature. The absorptance also decreases with decreasing frequency. Therefore, the deviation of ϕ_{23} from $-\pi$ will be largest at room temperature at the high-frequency limit of the experiments, 400 cm^{-1}. From the analysis in Chapter 5, the room-temperature refractive index and extinction coefficient of gold at 400 cm^{-1} are approximately $n = 48$ and $\kappa = 150$. These parameters were determined using the anomalous skin effect theory with completely diffuse electron scattering at the metal surface, i.e., $p = 0$, which is found to best match the experimental data measured in this work.

The complex index of refraction for gold and silicon are used in Eq. (2.6) to determine ϕ_{23}, yielding $\phi_{23} = -177.6^\circ \approx -180^\circ$. The term ϕ_{23} appears in Eq. (2.26) as $\cos^2\left(\frac{\phi_{23}}{2}\right)$, which is nearly zero. Therefore, the assumption that $\phi_{23} = -\pi$ is correct for this work and the simplified expression for $A_s(\nu_{\mathrm{RFP0}})$ given in Eq. (2.27) is valid.

2.4 Uncertainty Analysis

The absorptance of the sample $A_s(\nu_{\mathrm{RFP0}})$ is determined using the simplified expression Eq. (2.27), which depends on R_{12}, the reflectance of the silicon used in the etalon and R_{RFP0}, the reflectance at the etalon resonance minima. The relative uncertainty in the sample absorptance is dependent on the uncertainty interval for these two quantities δR_{12} and δR_{RFP0}, and is given by,

$$\frac{\delta A_s(\nu_{\mathrm{RFP0}})}{A_s(\nu_{\mathrm{RFP0}})} = \frac{1}{A_s(\nu_{\mathrm{RFP0}})}\sqrt{\left(\frac{\partial A_s(\nu_{\mathrm{RFP0}})}{\partial R_{12}}\delta R_{12}\right)^2 + \left(\frac{\partial A_s(\nu_{\mathrm{RFP0}})}{\partial R_{\mathrm{RFP0}}}\delta R_{\mathrm{RFP0}}\right)^2} \tag{2.30}$$

where:

$$\frac{\partial A_s(\nu_{\mathrm{RFP0}})}{\partial R_{12}} = -\frac{2(1-R_{\mathrm{RFP0}})(1-R_{12})\left[\left(1+2\sqrt{R_{\mathrm{RFP0}}R_{12}}+R_{12}\right)+(1-R_{12})\left(\sqrt{\frac{R_{\mathrm{RFP0}}}{R_{12}}}+1\right)\right]}{\left(1+2\sqrt{R_{\mathrm{RFP0}}R_{12}}+R_{12}\right)^3}$$

(2.31)

$$\frac{\partial A_s(\nu_{\mathrm{RFP0}})}{\partial R_{\mathrm{RFP0}}} = -\frac{(1-R_{12})^2\left[\left(1+2\sqrt{R_{\mathrm{RFP0}}R_{12}}+R_{12}\right)+2(1-R_{\mathrm{RFP0}})\left(\sqrt{\frac{R_{12}}{R_{\mathrm{RFP0}}}}\right)\right]}{\left(1+2\sqrt{R_{\mathrm{RFP0}}R_{12}}+R_{12}\right)^3} \tag{2.32}$$

The reflectance at the vacuum-silicon interface may be determined using Eq. (2.20) and the complex refractive index for silicon determined in Chapter 4. Ignoring the small extinction coefficient and letting $n_{\mathrm{si}} = 3.42$ gives $R_{12} = 30.0\%$.

The experimentally measured values for R_{RFP0} ranged from approximately 90% to 98%. With $R_{12} = 30.0\%$, this corresponds to a range of A_s values from 0.897% to 0.173%. To determine an estimate of the experimental error for this technique, the uncertainty intervals δR_{12} and δR_{RFP0} are set at ±1%. This is an upper bound for δR_{12}, because the uncertainty interval for the silicon reflectance is less than ±1%. For $A_s = 0.897\%$, the relative uncertainty is ±11.71%. For a single-bounce reflectance measurement, the equivalent accuracy would be ±0.105%, which is virtually impossible to achieve. For $A_s = 0.173\%$, the relative uncertainty is ±50.7%, which corresponds to a single-bounce reflectance measurement accuracy of ±0.088%.

To determine the error for the experimental measurements, δR_{RFP0} is set at the larger of either ± 1% or twice the absorptance determined using Eq. (2.27). This sets an upper bound for the experimental error.

2.5 Correction for Spectra Distortion

To extract the optical constants from the reflection Fabry-Pérot etalon reflectance data, the reflectance minima R_{RFP0} must first be determined. The uncertainty interval for the reflectance minima,δR_{RFP0}, is largely determined by the experimental error in determining R_{RFP0}. Due to the difficulty in placing the sample and reference in the same location in the infrared beam, the reflectance spectra are often skewed. This work develops an approximate method to extract R_{RFP0} using the near-unity reflectance of the samples being investigated.

From Eq. (2.29) it is evident that the reflectance maxima equals the single-bounce reflectance of the sample being investigated. For the samples investigated here, the reflectance is nearly 100%. Ideal etalon reflectance data consists of equally spaced maxima and minima, with reflectance maxima of nearly 100% and little skew across the spectrum being investigated. The minima can be read directly from the experimental data in this instance.

In actual experimental measurements, the spectra are often severely skewed and the maxima frequently will deviate significantly from 100% due to alignment difficulties. To determine R_{RFP0} from distorted spectra, the minima are divided by the arithmetic average of the maxima on either side of the minima. The procedure is equivalent to dividing the value for R_{RFP0} by the reflectance of the material at that frequency. The uncertainty interval δR_{RFP0} is determined in part by the reflectance of the material. That is, for a material with a reflectance of 99%, this method increases the measured value for R_{RFP0} by approximately 1%.

To confirm the validity of this technique, measurements were performed at room temperature in which the ratio of the single-beam measurements for the sample and reference resulted in a flat spectra and a skewed spectra. The results are shown in Figs. 2.2, 2.3, and 2.4.

Figure 2.2 shows the reflectance spectra for a reflection Fabry-Pérot etalon sample consisting of a gold film, labeled BI#9, and the silicon etalon. Sample BI#9 was prepared at Lincoln Laboratory and consists of a 3000 Å thick film, deposited on a 100 Å Ti buffer layer on an atomically smooth silicon. The measurement is performed using the room-temperature reflectance accessory, which is described in Chapter 3. This accessory minimizes positioning errors caused by the interchange of the sample and the gold reference mirror. The reflectance maxima equal approximately 101.5% across the investigated spectral range, possibly due to a small positioning error or to thermal drift.

Figure 2.3 shows the reflectance spectra for sample BI#9 measured using the low-temperature reflectance accessory, which is also described in detail in Chapter 3. The sample is

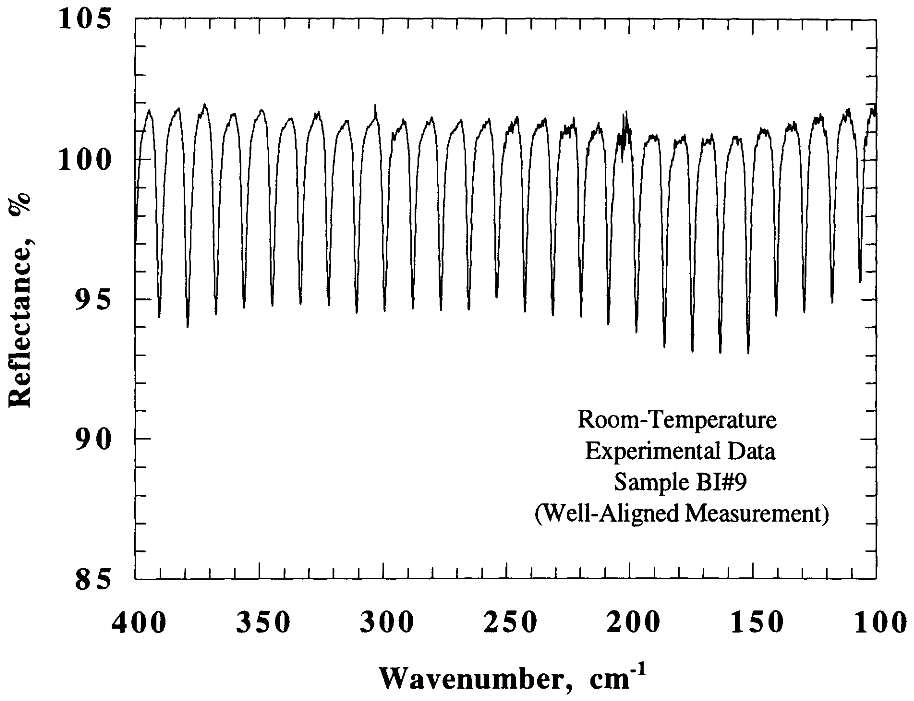

Figure 2.2 Reflectance of a silicon-on-gold Fabry-Pérot etalon (gold sample BI#9) performed using the room-temperature reflectance accessory.

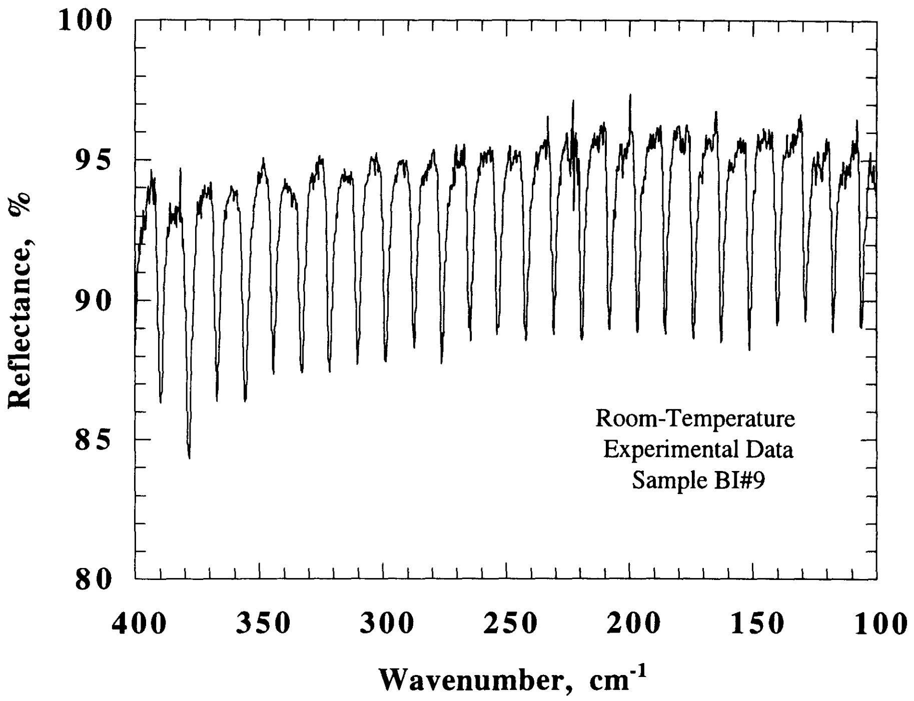

Figure 2.3 Reflectance of a silicon-on-gold Fabry-Pérot etalon (gold sample BI#9) performed using the low-temperature reflectance accessory.

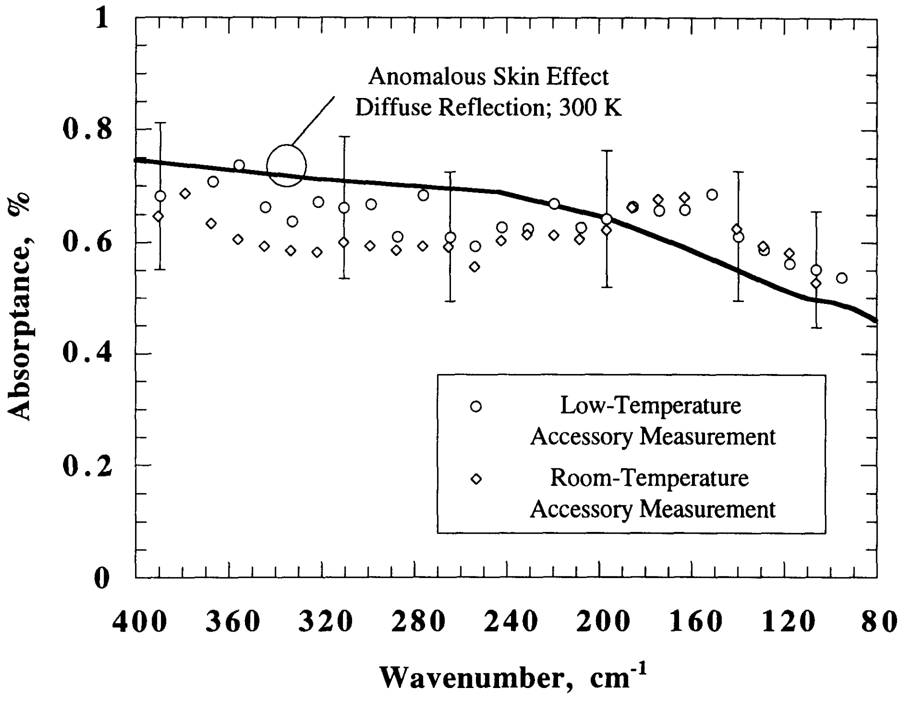

Figure 2.4 Absorptance of gold sample BI#9 determined using the room-temperature reflectance accessory and the low-temperature reflectance accessory.

fixed to the cold finger of the cryostat. With this experimental arrangement, it is very difficult to ensure that the sample and reference are placed in the same position in the infrared beam. Thus, the reflectance data exhibits a slope, with the reflectance maxima increasing from ~93% at the high-frequency limit to ~95% at the low-frequency limit of the experiment.

The sample and gold background single-beam spectra used in Figs. 2.2 and 2.3 are obtained using the standard far-infrared experimental arrangement used for all experiments in this work. The arrangement is described briefly here, with more details provided in Chapter 3. The infrared beam incidence angle is approximately 10°. A Glowbar ceramic source is used with an aperture of 1 mm. The beamsplitter is fabricated from 6 μm-thick polyethylene . The detector is a liquid-helium cooled silicon bolometer with an NEP of ~1 x 10^{-13} W/Hz$^{1/2}$. The measurement resolution is 0.25 cm^{-1}, with a zero-filling factor of 4. The FT-IR optical path is evacuated to ~1 x 10^{-3} torr. The duration of each measurement is approximately 2.6 hrs., consisting of 8000 scans at a scan speed of 100 Khz. The interferogram is multiplied by the Blackman-Harris four-term apodization function for all measurements to minimize the artificial side lobes caused by the limited resolution of the instrument. Allowing for signal stabilization and sufficient evacuation, the elapsed time for the sample and reference measurements was approximately 7 hrs.

Figure 2.4 shows the absorptance of gold film BI#9 for both reflectance accessories assessed from the experimental data in Figs. 2.2 and 2.3 using Eq. (2.27) along with a absorptance prediction made using the anomalous skin effect, with diffuse electron scattering at the metal surface. The error bars are determined using Eq. (2.30), and equal approximately 20% of the absorptance values. The data derived using the technique described here from the skewed spectra agree within the experimental error with the data from the flat spectra.

This method potentially eliminates the need for reference measurements to be performed. Provided that the material is a very good reflector, without any spectral features that vary significantly between the reflectance peaks, the R_{RFP0} data could be extracted directly from the single-beam measurement for the sample. This approach would significantly reduces the experimental time and effort.

It is difficult to extract useful reflectance data from single-reflection reflectance data that exhibit a slope. Additionally, thermal drift can change the reflectance data measured using single-reflection techniques by as much as 5% per degree change in ambient temperature (McBride et al., 1997). The signals measured by the thermal detectors used in FT-IR spectroscopy are susceptible to changes in ambient temperature, or, for purged systems, changes in the temperature of the purge gas. If the ambient temperature fluctuates by a few degrees between sample and reference measurements, the reflectance determined by the ratio of sample and reference single beam measurements will be significantly in error. The method described above for the reflection Fabry-Pérot etalon measurements is free of the effects of thermal drift because all of the information is derived from the sample single-beam measurement. Thus, if the signal changes as a result of thermal drift, the reflectance maxima and minima change by the same amount.

2.6 Air Gap Between Silicon Etalon and Sample

The reflection Fabry-Pérot etalon sample stack is formed by carefully placing the silicon etalon on top of the sample and clamping them together with two copper plates. Prior to this, both surfaces are cleaned of dust using blasts of dry nitrogen. Other more rigorous procedures involving chemical cleaning and preparation in a clean room yielded similar results. The silicon and sample are observed to stick firmly together, indicating a close mating between the materials.

Despite these precautions, stray dust particles, surface curvature, and surface roughness present obstacles to achieving perfect contact between the silicon and the sample. Air gaps between the two surfaces may result, which might alter the measured reflectance minima from that predicted by thin-film optics.

The flatness of the silicon etalon, the gold films, and the $YBa_2Cu_3O_7$ films are verified using a quartz optical flat, with a flatness specification of $\lambda/20$. The films are mounted on a copper plate used for the measurements and held against the flat with approximately the same force used for the silicon-sample stack. The samples are observed to detect the presence of Newton's Rings which indicate a change in thickness (Guenther, 1990). All samples appear black through the flat, indicating that the films were flat to within approximately $\lambda/4$, or ~0.15 μm. The flatness of the $SrTiO_3$ substrates on which the $YBa_2Cu_3O_7$ films were deposited was measured prior to the deposition process using a non-contact laser interferometric technique. The measurements indicted that the substrate varied from perfect flatness by 0.2 μm at the edges.

The surface roughness of a $YBa_2Cu_3O_7$ film deposited under conditions similar to those used for the films examined in this work was measured using a profilometer. The rms roughness was determined to be $\eta = 319$ Å ± 25 Å. The roughness of the gold films was not measured, but the films are specular, so the surface roughness is much less than 0.4 μm (Brewster, 1992). The roughness of the silicon etalon also was not measured, but the thickness specification for the material is 127 μm ± 0.05 μm. Thus, the roughness of the silicon is much less than 0.05 μm, with local variations of ~4 Å. In comparison to the other materials, the silicon can be assumed to be perfectly smooth.

The approximate surface roughness of the materials used in this work are much less than 0.4 μm, and the wavelength investigated in this work ranges between 20 μm and 100 μm. The ratio of the surface roughness to the shortest infrared wavelength is much less than unity. Thus, the surfaces may be modeled as perfectly smooth (Beckmann and Spizzichino, 1977), satisfying one of the requirements for the validity of the thin-film optics analysis.

However, a thin air gap between the silicon and the sample may exist as a result of the sample surface roughness or the presence of dust, etc. An air gap created by surface roughness is illustrated in Fig. 2.5. Based on the experimental measurements presented above, the air gap thickness is expected to be much less than 0.2 μm.

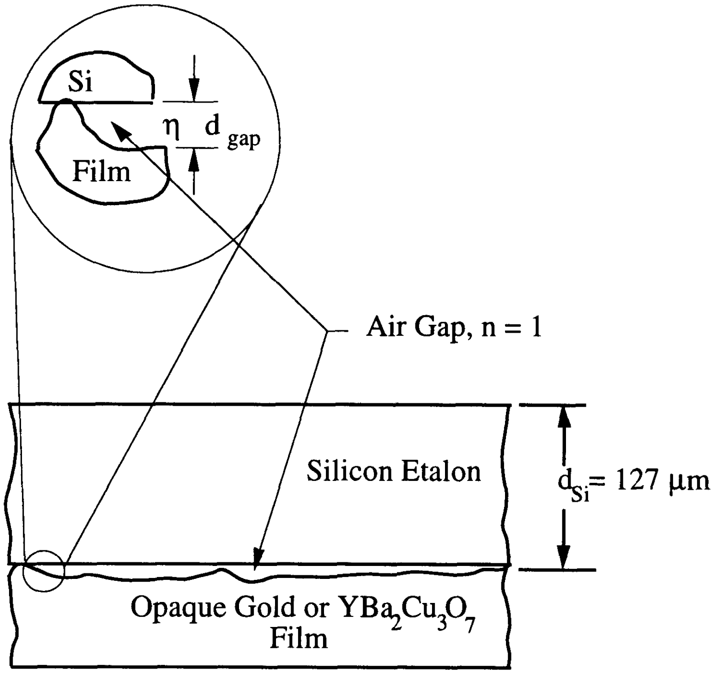

Figure 2.5 Air gap between the silicon etalon and the sample caused by surface roughness.

The effect of an air gap on the reflectance minima is analyzed using multilayer thin-film optics for the geometry pictured in Fig. 2.6. The stack consists of the silicon etalon, an air gap of varying thickness d_{gap} and an opaque sample. The surfaces are assumed to be smooth and plane-parallel. The incident infrared beam travels normal to the silicon surface. The theory for the prediction of the reflectance and transmittance of a multilayer thin film stack is described in Appendix A.

Figure 2.7 shows the change in the reflectance minimum δR_{RFP0} for a resonance with a frequency of approximately 396 cm^{-1} from the value predicted with no gap. The influence of the air gap on the predicted R_{RFP0} is largest at the high-frequency limit of the experimental measurements, ~400 cm^{-1}. The sample surface for the prediction is gold. The anomalous skin effect theory with diffuse electron reflection is used to determine the optical properties of the gold. The spacing is varied between 0 μm and 0.5 μm. For spacings of approximately 0.2 μm, the effect of the air gap is negligible. For gaps as large as 0.4 μm, the air gap effect is much less than the experimental error. Thus, the air gap is determined to be a small source of error for the experiments presented in this work.

2.7 Performance Limitations of the Reflection Fabry-Pérot Etalon

In addition to the source of error discussed in the previous section, the experimental performance of the reflection Fabry-Pérot etalon is limited by imperfections in the materials of the etalon stack, the departure from perfect collimation and non-vertical incidence of the FT-IR infrared beam, experimental resolution limitations, etc. Deviations from theoretical performance have been treated by numerous authors, including notable reviews by Hernandez (1986), Steel (1967), and Vaughan (1989).

The parameters which cause the largest deviations from the theoretical prediction are the surface roughness and deviation from parallelism of the silicon and sample films and the range of angles that may pass through the experimental arrangement. Each of these parameters has an

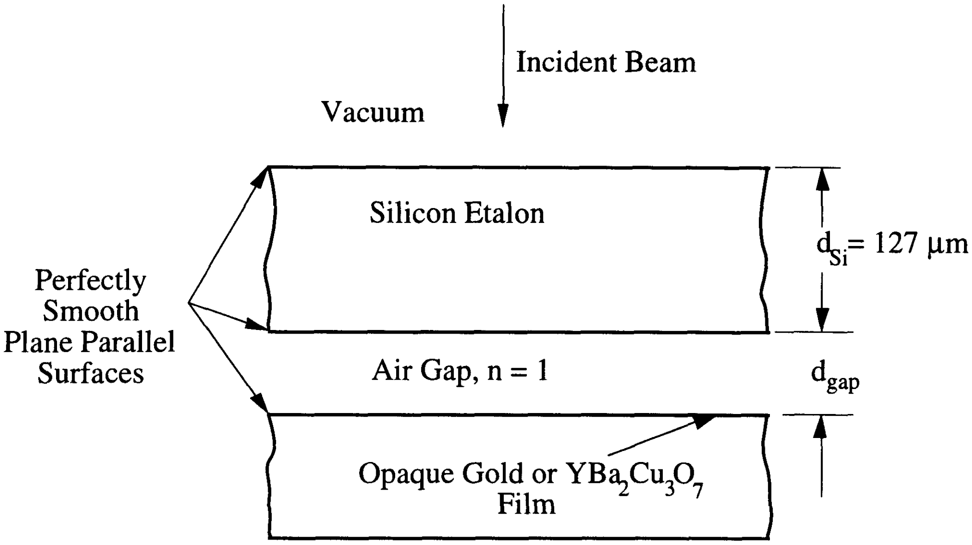

Figure 2.6 Idealized representation of the air gap between the silicon etalon and the sample caused by surface roughness.

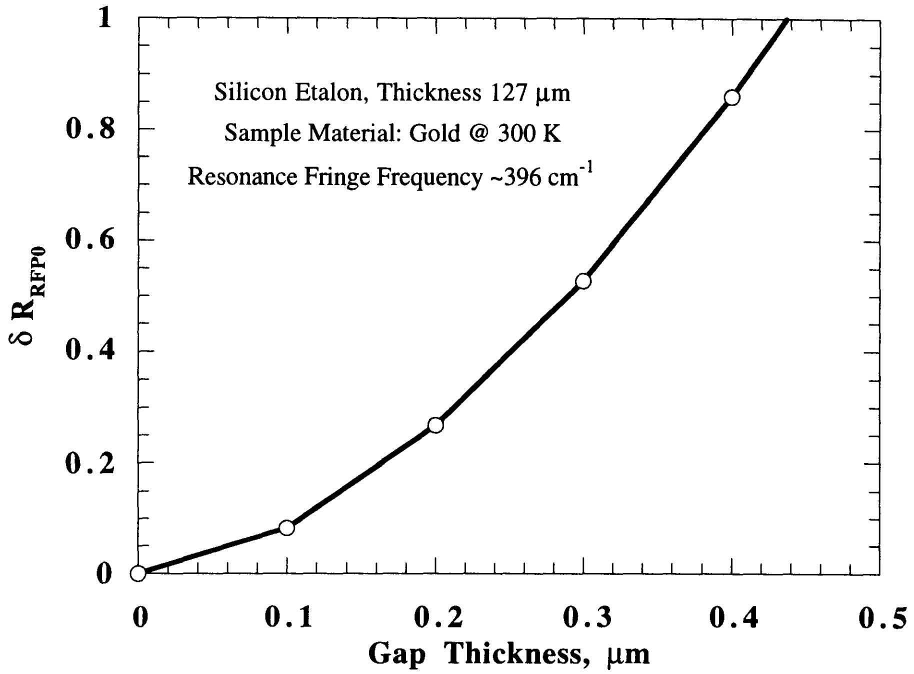

Figure 2.7 Change in the predicted reflectance minimum with gap thickness for the multilayer shown in Fig. 2.6.

associated finesse. To examine the performance of the experimental system used in this work, the overall finesse of the system, $\Im_{\mathrm{SYS}}$, is determined according to the relation (Moore et al., 1989),

$$\frac{1}{\Im_{\mathrm{SYS}}^2}=\frac{1}{\Im_{\mathrm{T}}^2}+\frac{1}{\Im_{\mathrm{F}}^2}+\frac{1}{\Im_{\mathrm{P}}^2}+\frac{1}{\Im_{\mathrm{NC}}^2} \tag{2.33}$$

where $\Im_{\mathrm{T}}$ is the theoretical finesse, $\Im_{\mathrm{F}}$ is the flatness-limited finesse, $\Im_{\mathrm{P}}$ is the parallelism-limited finesse, and $\Im_{\mathrm{NC}}$ is the finesse limitation due to the lack of collimation of the infrared beam. This analysis assumes that there is no air gap between the silicon and the sample.

To estimate $\Im_{\mathrm{T}}$ using Eq. (2.18) requires the reflectance of the silicon wafer, R_{12}, and reflectance of the etalon at resonance, R_{RFP0}. Ignoring any loses in the silicon and using $n_{\mathrm{Si}} = 3.42$ yields $R_{12} \approx 30\%$. Experimental values for R_{RFP0} range between 0.9 and ~0.99. Choosing $R_{\mathrm{RFP0}} = 0.99$ determines the upper bound for the theoretical finesse. From Eq. (2.18), $\Im_{\mathrm{T}} = 5.13$.

To examine the effects mentioned above on the finesse, the spread of the frequency of the absorption maximum due to each effect is determined. The ratio of the free spectral range of the etalon to this quantity gives the finesse for each effect. The free spectral range, ν, for an etalon of thickness d is:

$$\Delta\nu=\frac{1}{2n_{\mathrm{Si}}d} \tag{2.34}$$

When the absorptance of a sample is small, i.e., $\kappa_{\mathrm{s}} \gg n_{\mathrm{s}}$, $\phi_{23} \approx \pi$. The expression for the etalon resonance frequencies, Eq. (2.11), reduces to:

$$\nu_{\mathrm{m}} \approx \frac{1}{2n_{\mathrm{Si}}d}\left(m+\frac{1}{2}\right) \tag{2.35}$$

The surface roughness of the silicon and the sample determines the flatness-limited finesse, $\Im_{\mathrm{F}}$. The actual surface roughness of the silicon sample is much less than 0.05 μm. The thickness deviation specification was given for a two-inch wafer, including the surface roughness and deviation from parallelism. The sample surfaces are specular, indicating that the surface roughness is much less than 0.4 μm. To determine a minimum value for $\Im_{\mathrm{F}}$, the 0.4 μm limit is chosen as a maximum surface roughness Δs for the silicon-vacuum and the silicon-sample etalon interfaces. The average error in the etalon thickness is $\sqrt{2}\Delta s$. This results in a spread in the frequency of maximum transmission of:

$$\Delta \nu_{\mathrm{m,F}} \approx \frac{\Delta s}{\sqrt{2} n_{\mathrm{Si}} d^2}\left(m+\frac{1}{2}\right) \approx \frac{\sqrt{2}\, \nu_{\mathrm{m}} \Delta s}{d} \tag{2.36}$$

The resultant flatness-limited finesse is:

$$\Im_{\mathrm{F}} = \frac{\Delta \nu}{\Delta \nu_{\mathrm{m,F}}} = \frac{\Delta \nu\, d}{\sqrt{2}\, \nu_{\mathrm{m}} \Delta s} = \frac{1}{2\sqrt{2}\, \nu_{\mathrm{m}} \Delta s} \tag{2.37}$$

The flatness-limited finesse is smallest at the high-frequency limit of the experiment, $\nu \approx 400$ cm^{-1}. At this frequency, $\Im_{\mathrm{F}} = 22$.

The silicon and the sample may not be randomly rough and the flatness specification used above may represent an average deviation from parallelism. The minimum parallelism-limited finesse $\Im_{\mathrm{P}}$ may be estimated by assuming a deviation from parallelism of Δs over the lateral dimension of the etalon, ~5 mm. The spread in the frequency of maximum transmission due to the deviation from parallelism is,

$$\Delta \nu_{\mathrm{m,P}} \approx \frac{\Delta s}{2 n_{\mathrm{Si}} d^2}\left(m+\frac{1}{2}\right) \approx \frac{\nu_{\mathrm{m}} \Delta s}{d} \tag{2.38}$$

The parallelism-limited finesse is,

$$\Im_{\mathrm{P}} = \frac{\Delta \nu}{\Delta \nu_{\mathrm{m,P}}} = \frac{\Delta \nu\, d}{2\, \nu_{\mathrm{m}} \Delta s} = \frac{1}{2\, \nu_{\mathrm{m}} \Delta s} \tag{2.39}$$

At the high-frequency limit of the experiment, $\nu \approx 400$ cm^{-1}, $\Im_{\mathrm{P}} = 31$.

To determine the finesse limitation due to the lack of collimation of the infrared beam, $\Im_{\mathrm{NC}}$, requires an estimation of the angular width 2β of the infrared beam focused onto the sample and the maximum angular spread of rays passing through the FT-IR, $\Delta\beta$. Figure 2.8 shows a paraxial ray approximation of the FT-IR and sample holder optics with the parameters required for these estimations.

Figure 2.9 shows a simplified ray trace of the optics used to focus the infrared beam onto the sample. The focal length of the mirror focusing the beam onto the sample f_{samp} is approximately 153 mm. The mirror diameter D is approximately 40 mm. Employing the paraxial ray approximation, the angular width of the focused beam is $\beta \approx D/2f_{\mathrm{samp}} = 7.5^\circ$.

Figure 2.8 shows the ray trace through the spectrometer for a point source. A point source is physically impossible. In the spectrometer, the source is focused onto an aperture wheel with a range of circular aperture sizes, from 0.25 mm to 12 mm. The size of the source is effectively given by the chosen aperture size. The source is re-imaged onto the sample and, finally, onto the detector. The source of diameter w_{s} subtends an angle $2\Delta\beta_{\mathrm{s}}$ at the collimating lens of focal length $f_{\mathrm{s}} = 153.7$ mm. The detector element of diameter w_{d} subtends an angle $2\Delta\beta_{\mathrm{d}}$ at the focusing lens of focal length $f_{\mathrm{d}} \approx 100$ mm. In the experiments presented here, the image of the source at the sample position is smaller than the sample diameter w_{s}. The maximum angular spread of rays passing through the system is the smaller of the two angles.

In this experiment, w_{s} is minimized to minimize phase variations across the beam diameter in order to improve the collimation of the infrared beam and to limit the range of angles incident on the reflection Fabry-Pérot etalon. Noise limitations require $w_{\mathrm{s}} = 1$ mm for the experiments. The detector element of the bolometer has an effective diameter of $w_{\mathrm{d}} \approx 3$ mm. Thus, the angular width of the beam passing through the spectrometer $2\Delta\beta$ is limited by the source aperture and given by $2\Delta\beta \approx w_{\mathrm{s}}/f_{\mathrm{s}} \approx 0.4^\circ$.

The maximum range of incidence angles for the reflection Fabry-Pérot etalon is the sum of the half-angle of the beam focused onto the sample, β, and the maximum half-angle spread of rays passing through the system, $\beta + \Delta\beta \approx 7.7^\circ$. This value is an overestimate because the small

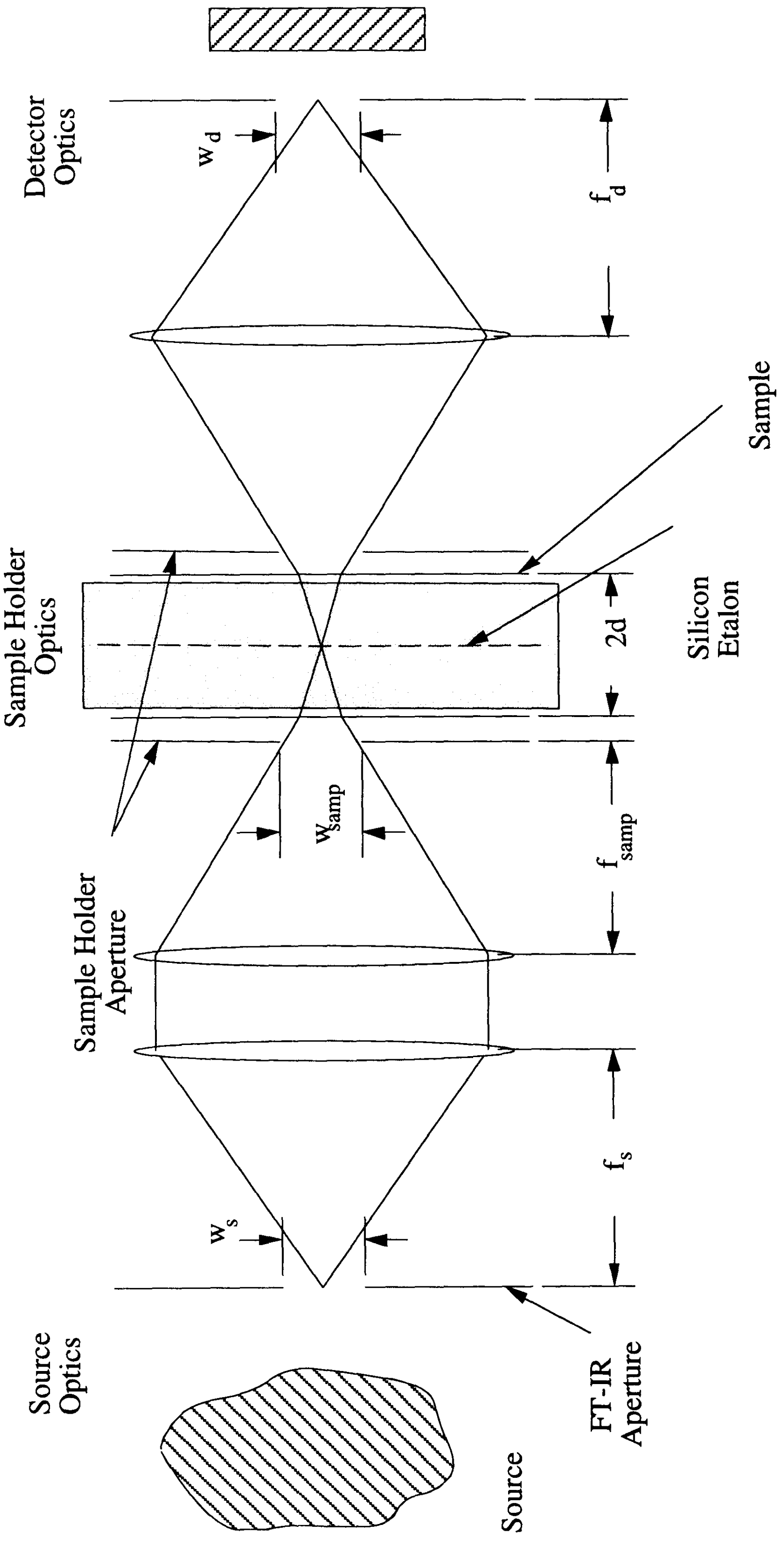

Figure 2.8 Simplified paraxial ray schematic of the FT-IR and sample holder optics.

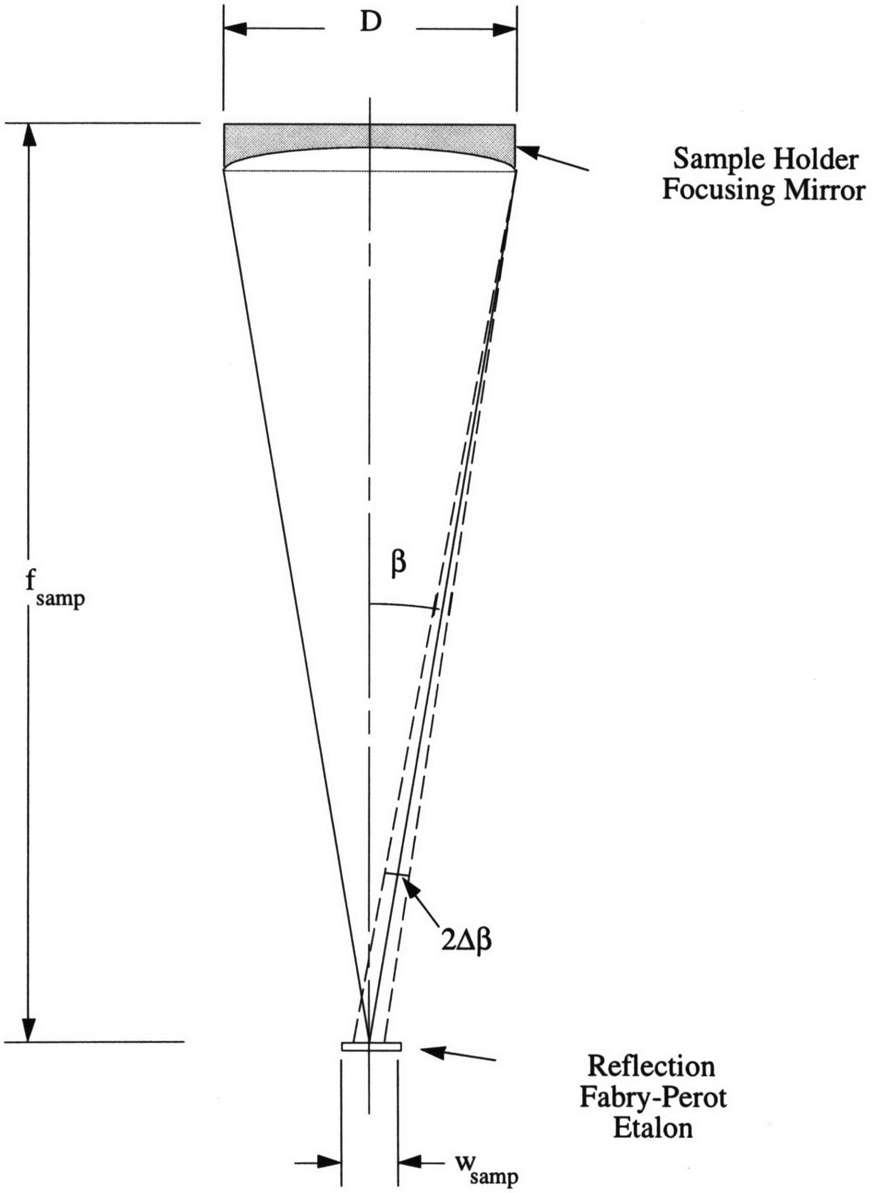

Figure 2.9 Range of angles convergent upon the reflection Fabry-Pérot sample.

aperture setting decreases β by a factor of two because the beam size on the focusing mirror is roughly one-half the mirror diameter D.

By Snell's law, the large refractive index of the silicon, $n_{\mathrm{Si}} = 3.42$, reduces the angular width of the rays inside the silicon, which effectively improves the collimation of the interfering waves and increases the finesse of the etalon. This phenomenon is illustrated in Fig. 2.10. According to Snell's law, at the interface between a vacuum space and silicon, the angular width inside the silicon is , $\beta_{\mathrm{Si}} = 2.2°$.

The finesse limitation due to the lack of collimation of the infrared beam, $\Im_{\mathrm{NC}}$, is determined by estimating the spread in the frequency of the absorption maxima associated with the angular width inside the silicon, β_{Si}. To account for this, the real part of the complex phase difference, ϕ, is written as a function of β_{Si}:

$$\phi = 2\pi \nu n_{\mathrm{Si}} d \cos\beta_{\mathrm{Si}} \tag{2.40}$$

Rewriting Eq. (2.11) to account for off-normal incidence,

$$\nu_{\mathrm{m}} = \frac{1}{2n_{\mathrm{Si}} d \cos\beta_{\mathrm{Si}}}\left(m - \frac{1}{2\pi}\phi_{23}\right) \tag{2.41}$$

The spread in the frequency of the absorption maxima is:

$$\Delta\nu_{\mathrm{m,NC}} \approx \nu_{\mathrm{m}} \frac{\beta_{\mathrm{Si}}^2}{2} \tag{2.42}$$

Writing $\Im_{\mathrm{NC}}$ as the ratio of the free spectral range, $\Delta\nu$, for an etalon of thickness d to $\Delta\nu_{\mathrm{m,NC}}$ gives,

$$\Im_{\mathrm{NC}} = \frac{\Delta\nu}{\Delta\nu_{\mathrm{m,NC}}} = \frac{1}{\nu_{\mathrm{m}} n_{\mathrm{Si}} d \beta_{\mathrm{Si}}^2} \tag{2.43}$$

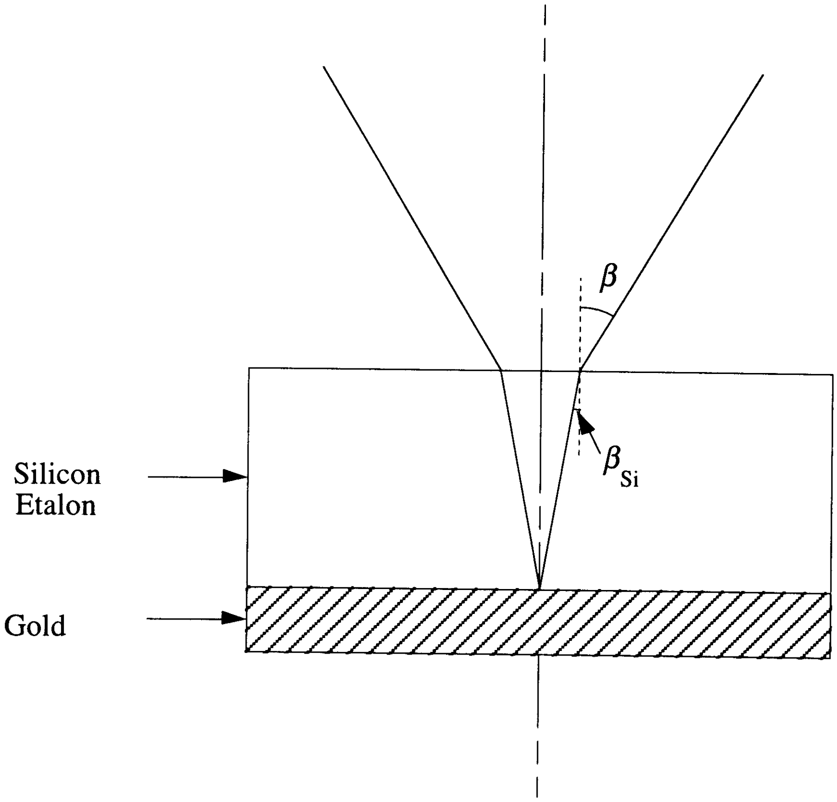

Figure 2.10 Range of angles inside silicon etalon.

The smallest $\Im_{NC}$ occurs at the high-frequency limit of the experiment, $\nu \approx 400\ \mathrm{cm}^{-1}$. Assuming there is a resonance at this frequency, $\Im_{NC} = 39$.

With estimates for the individual contributions to the overall finesse of the reflection Fabry-Pérot etalon, $\Im_{SYS}$ may be determined using Eq. (2.30). Based on this analysis, $\Im_{SYS} \approx 5$, compared to a theoretical finesse $\Im_T$ of 5.13. Given that $\Im_{SYS} \approx \Im_T$, the experimental results are closely approximated by the theoretical predictions made using thin-film optics. The effects considered here may be ignored.

2.8 Conclusions

Thin-film optics is used to extract the radiative properties of the sample layer from a silicon-on-sample reflection Fabry-Pérot etalon. The errors introduced by air gaps between the silicon and the sample, surface roughness, deviation from parallelism, and non-collimated radiation are examined. Based on this analysis, the predictions made by thin-film optics agree well with experimental results.

A method for extracting meaningful radiative property data from distorted reflection Fabry-Pérot etalon reflectance data is presented. The single-beam spectra for the etalon for metallic systems contains information which might eliminate the need to perform a reference measurement.

CHAPTER 3

EXPERIMENTAL PROCEDURE

3.1 Introduction

In this section, the methods used for preparing a silicon reflection Fabry-Pérot etalon sample are outlined. The FT-IR spectrometer is briefly described. Finally, the experimental apparatus used to perform the measurements presented here are described.

3.2 Silicon Reflection Fabry-Pérot Etalon Sample Preparation

To test the effect of preparation conditions on the measured spectra for the etalon stack sample, samples are prepared in two different ways: 1) in a class-1000 clean room with careful chemical cleaning procedures; and, 2) at the FT-IR bench, under normal room conditions and without chemical cleaning.

For the clean room preparation, the gold and silicon samples are first cut from wafers to the appropriate size using a diamond scribe. The $YBa_2Cu_3O_7$ samples are deposited on 10 mm square substrates and thus don't require cutting. The cutting procedure usually left one side of the sample covered with sample particles.

To remove these particles and other foreign contaminants, the gold and silicon samples undergo a chemical cleaning procedure. First, the samples are placed in a beaker of 111-trichloroethylene for one minute. Next, the samples undergo a five-minute ultrasonic cleaning procedure in a beaker of de-ionized 18 MΩ resistance water. Following this, the samples are placed in acetone and finally, methanol. The $YBa_2Cu_3O_7$ samples do not undergo any chemical cleaning process because of the potential for damaging the samples. These samples are cleaned of dust particles using dry nitrogen gas.

Samples prepared at the FT-IR bench are also cut to size with a diamond scribe. Particles on the film surfaces are removed using dry nitrogen gas.

The silicon-on-sample etalon stack is made in the same way for both preparation techniques. The sample is placed on a 1/16" thick, 5/8" square OFHC copper blank. A small amount of Apiezon N grease is placed on the copper prior to this step to ensure good thermal contact at the interface between the copper and the sample. The silicon etalon is placed on the sample and a 5/8" square OFHC copper blank with a 5 mm diameter center hole is placed on top of the silicon. The stack is firmly pressed together using four nuts and bolts. A photograph of the structure is shown in Fig. 3.1.

Reflectance measurement on samples prepared using both techniques show no appreciable difference. Given the relative simplicity of preparing samples at the FT-IR bench, most samples are prepared without chemical cleaning and in a regular room environment.

3.3 Fourier-Transform Infrared Spectrometer

3.3.1 General Arrangement

Figure 3.2 shows a schematic of the major components of the FT-IR bench used for this work, as well as the optical path of the infrared beam. Infrared radiation emitted by the source is

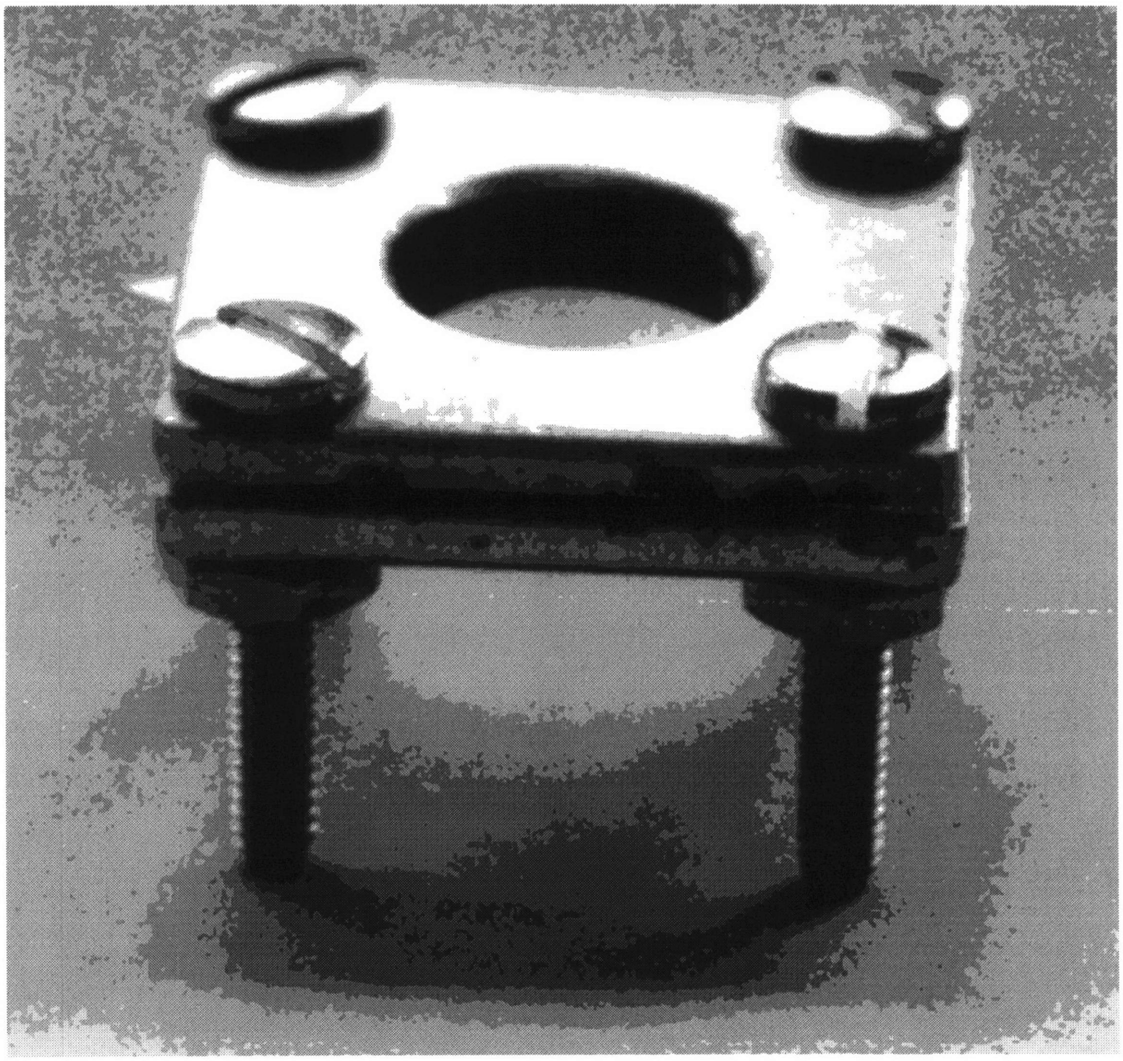

Figure 3.1 Reflection Fabry-Pérot etalon sample.

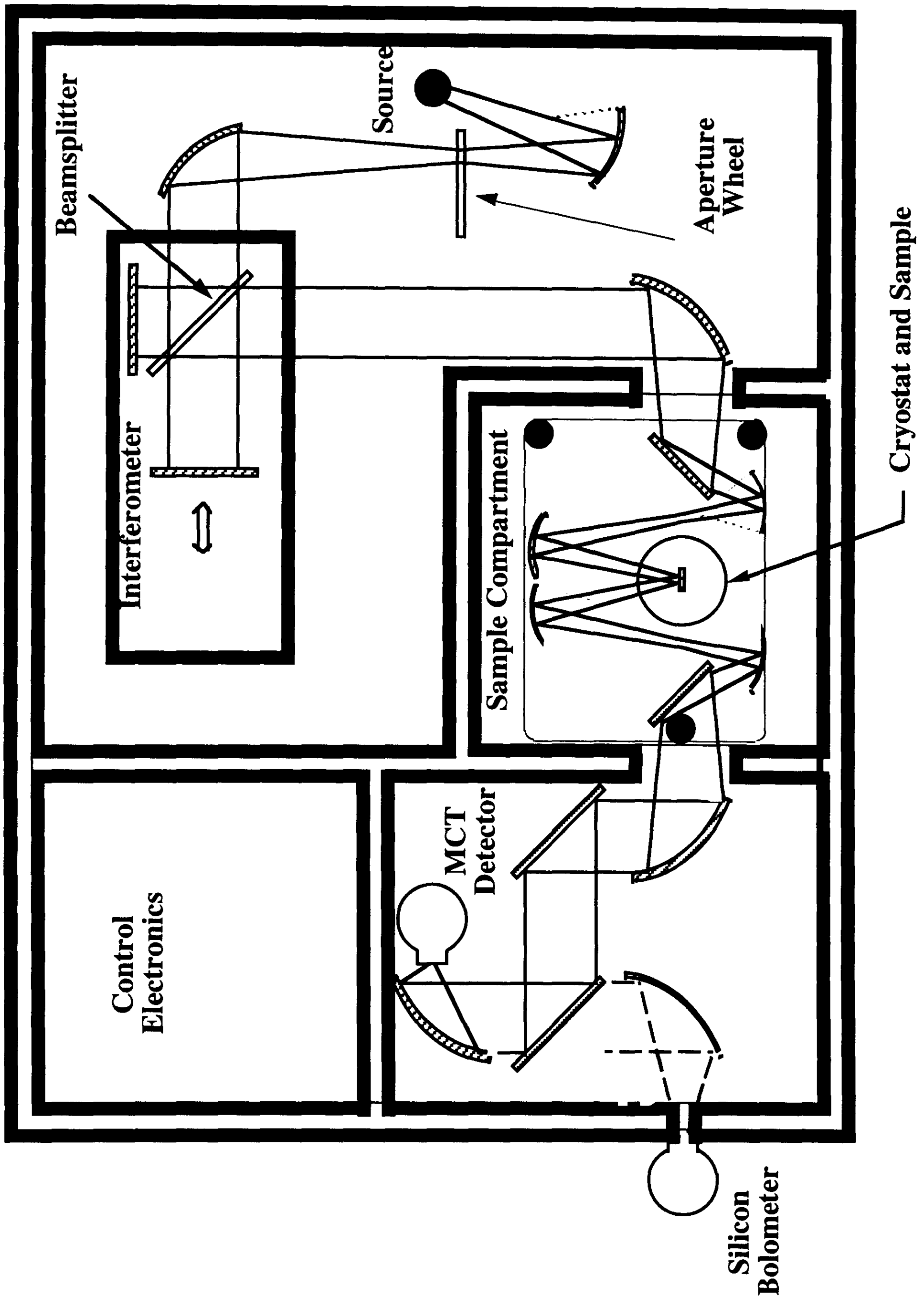

Figure 3.2 Schematic of the FT-IR.

focused onto the aperture wheel, where circular apertures between 0.25 mm and 12 mm can be selected. The aperture defines the spot size in the sample chamber. The beam passes through the Michelson interferometer, where it is modulated at audio frequencies. A He-Ne laser beam travels along the center of the infrared beam. Measuring the laser fringes enables the position of the moving mirror in the interferometer to be tracked. After the interferometer, the beam is focused onto the sample and re-focused onto the detector, where the interferogram is measured. Performing a Fourier transform on the interferogram yields the detector response as a function of frequency. The operation of an FT-IR is described in detail by Griffiths and de Haseth (1986).

A Bruker Instruments IFS-66v Fourier-Transform infrared spectrometer is used for all the experimental measurements. The entire bench shown in Fig. 3.2 is evacuated to ~1 x 10^{-3} torr to eliminate the very strong far-infrared water and CO_2 absorption bands from obscuring the signal. Evacuating the bench also improved the photometric accuracy of the instrument. McBride et al. (1997) showed that the photometric accuracy of nitrogen-purged FT-IR benches was strongly influenced by the room temperature. Signal stability experiments with the IFS-66v FT-IR show a signal drift of less than 0.5% over a 10-hr. period. Purged systems exhibit signal drifts of 2% or greater over a similar time period.

Far-infrared measurements for the silicon reflection Fabry-Pérot etalon samples are made using the following combination of FT-IR components: a 1500 K Glowbar source, a 6 μm Mylar beamsplitter, and a liquid helium cooled silicon bolometer with an NEP of ~1 x 10^{-13} W/$Hz^{1/2}$. This combination covers the spectral range from ~400 to 80 cm^{-1} with an excellent signal-to-noise ratio.

3.3.2 Measurement Accessories

A ray trace for the beam conditioning optics used for the room-temperature and low-temperature reflectance measurements is shown in Fig. 3.3. The optics are mounted on a

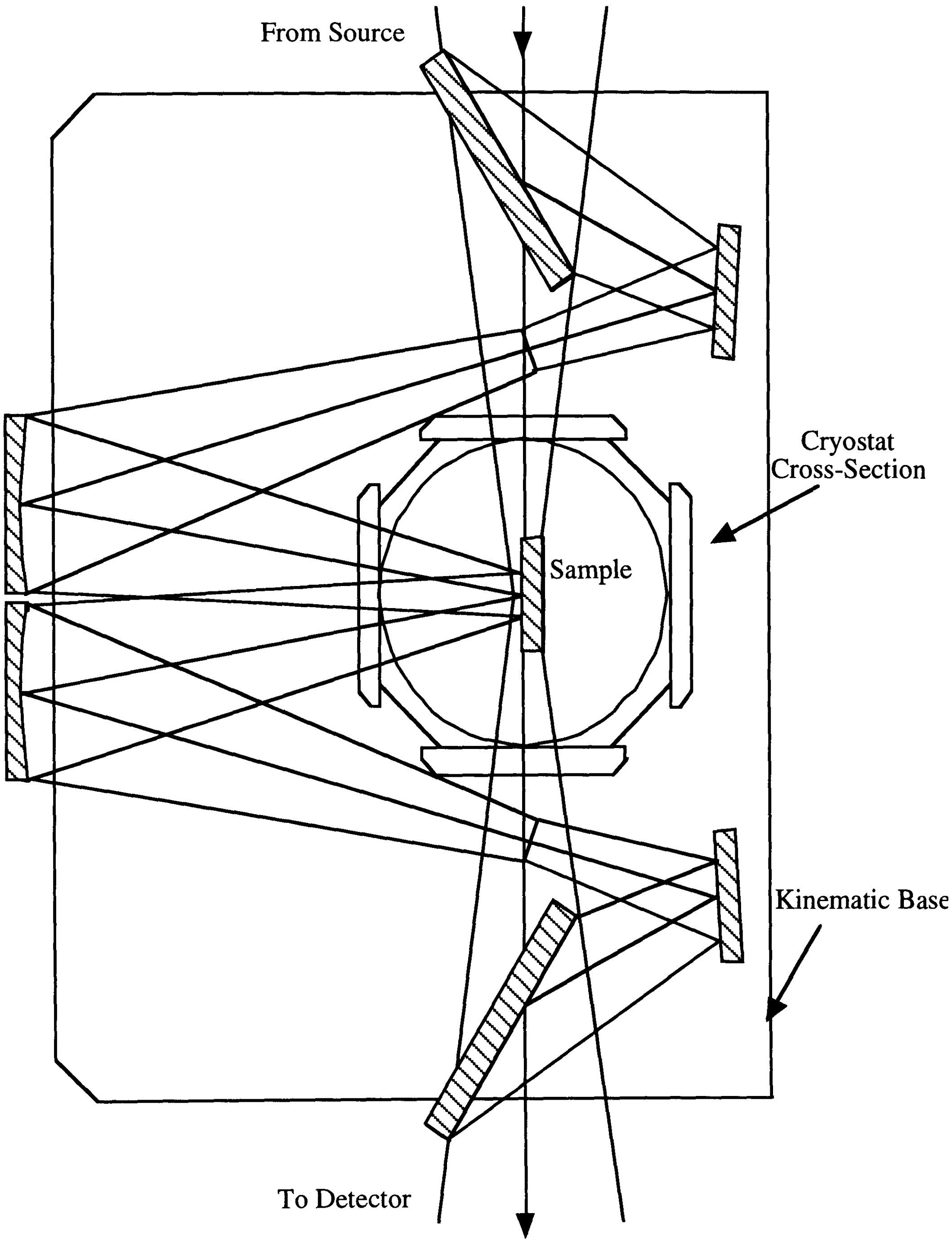

Figure 3.3 Reflectance accessory with ray trace.

kinematic base. The figure shows the cryostat at the focal point. To perform room-temperature measurements, the sample is positioned at the focal point by a special holder. For room-temperature measurements, an external He-Ne laser is used to accurately interchange the sample and reference.

Figures 3.4 and 3.5 show a top and side view of the transmission measurement accessory, respectively. The infrared beam passes straight through the samples chamber. A sample holder positions the sample at the focal point in the center of the sample chamber.

3.4 Cryostat System

Figure 3.6 shows a cross-section of the Oxford Instruments continuous flow cryostat used in the low-temperature measurements presented here. To cool the sample, liquid helium is transferred to the cryostat at a precisely controller flow rate. The sample temperature can be controlled by adjusting this flow rate and/or by the use of resistance heaters mounted near the sample. A picture of the complete low-temperature arrangement is presented in Fig. 3.7. The sample temperature is monitored using a rhodium-iron sensor mounted in a copper block near the sample. At low temperatures, thermal contact resistance can cause a significant temperature difference between the sample and the sensor. To evaluate this temperature difference, an experiment was conducted where a silicon diode was installed and held in place on the surface of a sample. The cryostat was cooled to the lowest possible temperature. At thermal equilibrium, the silicon sensor reading was ~2 K higher than the rhodium-iron sensor. Thus, for the low-temperature experiments presented here, the sample temperature is estimated to be ~6 K.

A wedged polyethylene window is used for the far-infrared measurements. The cryostat is evacuated using a liquid-nitrogen cold trap and an 80 l/s turbomolecular pump. The system is evacuated for approximately 12 hrs., reaching a pressure of approximately 10^{-5} torr.

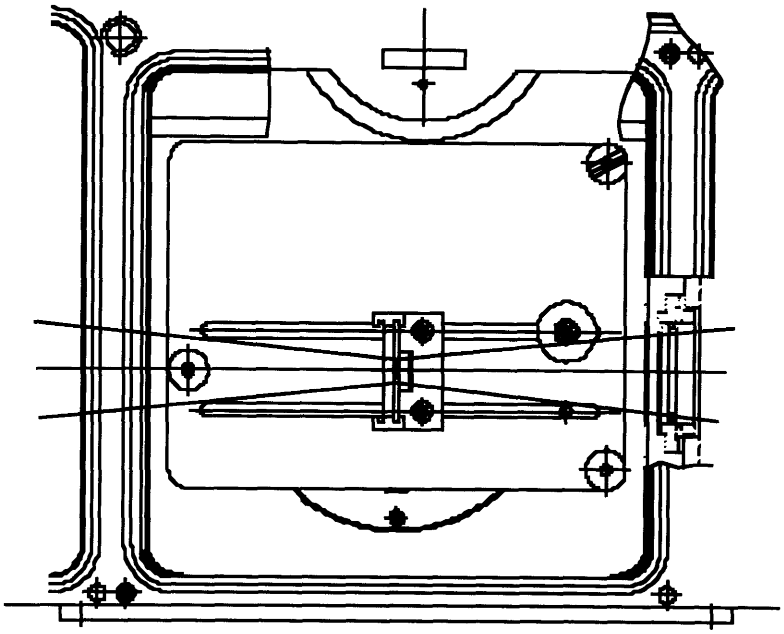

Figure 3.4 Top view of transmittance measurement accessory. Reprinted with permission from Bruker Instruments.

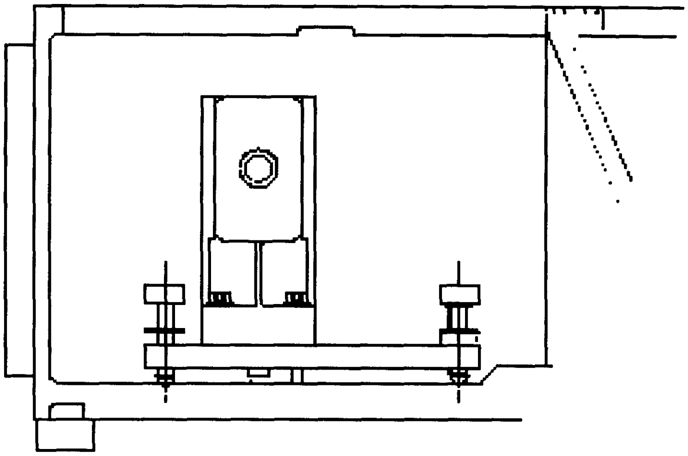

Figure 3.5 Side view of transmittance measurement accessory. Reprinted with permission from Bruker Instruments.

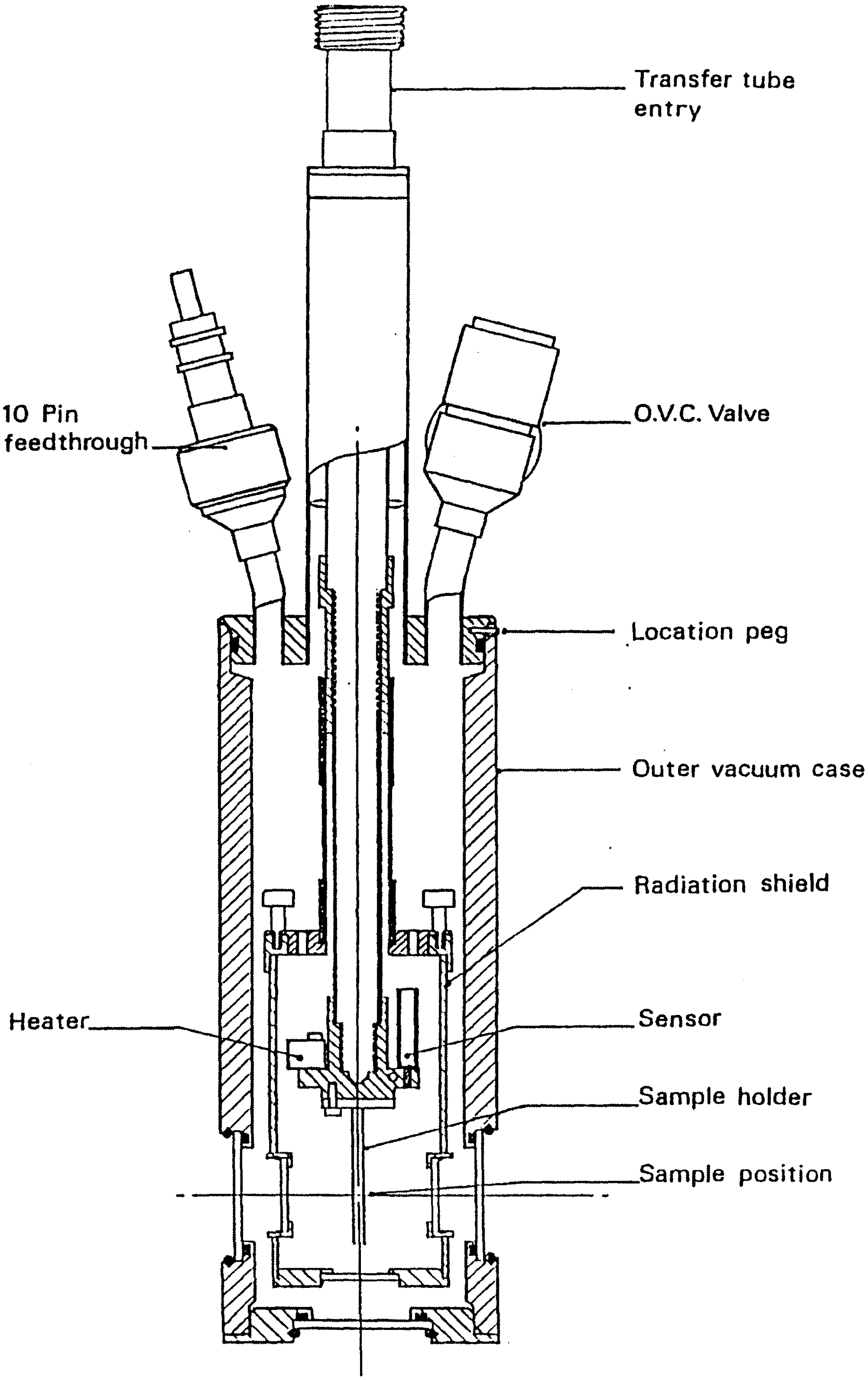

Figure 3.6 Cryostat cross-section. Reprinted with permission from Oxford Instruments.

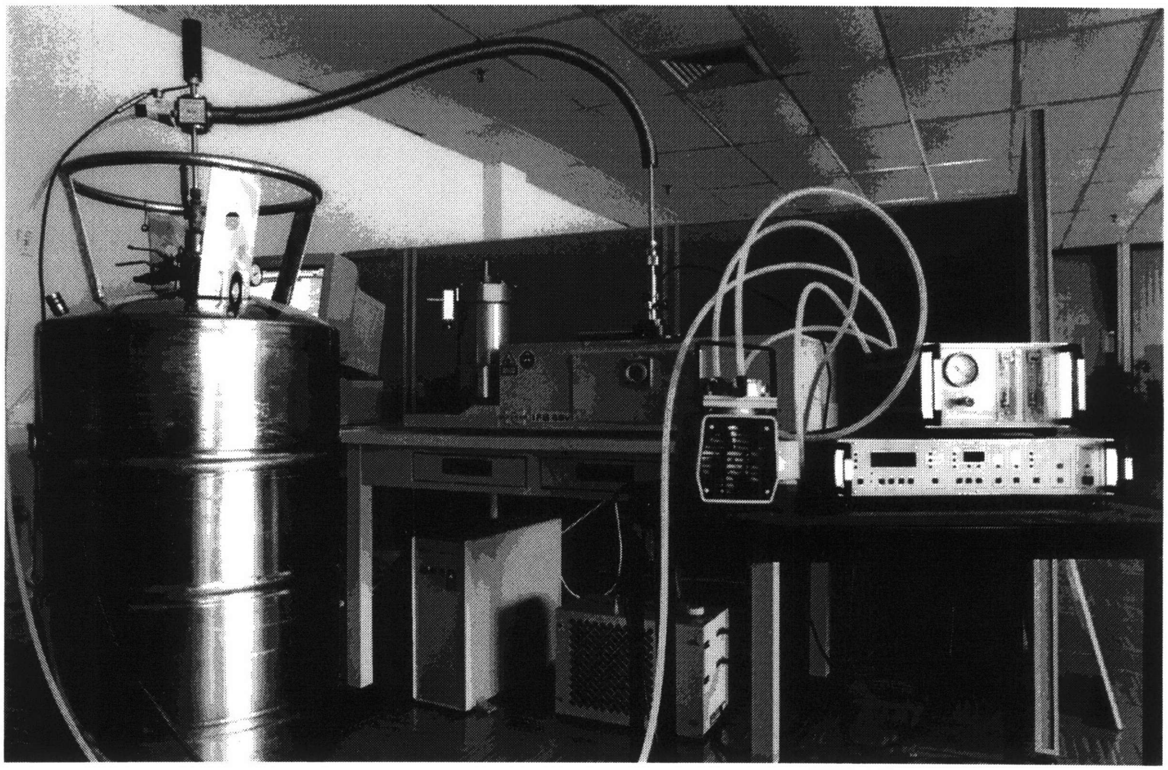

Figure 3.7 Low-temperature experimental arrangement.

Figure 3.8 shows the mechanism for mounting the silicon reflection Fabry-Pérot etalon sample to the cold finger of the cryostat. The etalon stack is held between two OFHC copper plates as described above. A copper plate with a 5-mm center hole is placed on top of the assembly. This plate is painted with low-emissivity flat black paint to minimize the effects of scattered radiation on the measured signal. The copper plates and etalon stack are then mounted onto the cold finger with spring-loaded screws. The thermal contact resistance between the sample and the cold finger is reduced by placing a thin layer of Apiezon N grease on the cold finger.

Figure 3.8 Radiation shield and cryostat with reflection Fabry-Pérot etalon sample in position.

CHAPTER 4

INFRARED RADIATIVE PROPERTIES OF SILICON

4.1 Introduction

To extract the radiative properties of the sample from the reflectance spectra of the reflection-Fabry-Pérot etalon requires knowledge of the optical properties of the silicon film used in the etalon sandwich. High-resistivity silicon is employed for this technique because of its very low loss and dispersion in the far-infrared which results in little distortion of the reflectance fringes. Additionally, the experimental technique demands a flatness and parallelism better than 1 μm for the etalon. These specifications are achievable with silicon using standard chemo-mechanical polishing (CMP) techniques. Type IIA diamond exhibits very low losses and is the only material that is transparent across the entire infrared spectral range from 7 μm to 1000 μm (Kimmitt, 1970). However, diamond remains prohibitively expensive and the material is currently not available commercially with sufficient flatness and plane-parallelism.

The silicon films used in this work were prepared by Topsil Semiconductor Materials A/S, Denmark. They were cut from 2" diameter wafers of double-side polished (111) *n*-type silicon, 127 ± 0.05 μm in thickness with a resistivity of 33.5 ± 3.3 Ω-cm. A CMP technique employing a colloidal suspension of flat silica particles was used to polish the silicon.

Silicon has a strong multi-phonon band centered at ~600 cm^{-1}, but the effect of the band on the optical properties is negligible for wavenumbers less than ~400 cm^{-1} (Johnson, 1959). Free-carrier absorption is essentially the only loss mechanism for silicon in this spectral range. Thus, it is desirable to employ high-resistivity silicon to minimize these losses.

The reflection-Fabry-Pérot etalon experiments presented in this work cover the spectral range from 400 to 100 cm^{-1}. The silicon used here is characterized at room temperature by reflection and transmittance measurements for this spectral range using an FT-IR spectrometer. A description of the experimental procedure is presented in Chapter 3.

Following a discussion of the existing experimental data for silicon, the results of these measurements are presented and silicon optical constants appropriate for the analysis of the reflection-Fabry-Pérot etalon data are recommended. The room-temperature properties of silicon are used even for the analysis of low-temperature experimental results. It was observed experimentally by examining the change in the frequencies of the reflection-Fabry-Pérot etalon resonances that the silicon refractive index changed only slightly upon cooling. Loewenstein et al. (1973) determined that the refractive index of silicon changed only slightly when cooled from room temperature to 1.5 K. Thus, ignoring the temperature effects on the refractive index is a negligible source of error. If the extinction coefficient of silicon is sufficiently small, it may be ignored in the analysis of the reflection-Fabry-Pérot etalon data. The extinction coefficient of silicon decreases upon cooling (Genzel et al., 1993). Thus, if this quantity may be ignored at room temperature, it is also negligible at low temperatures.

Despite a large effort to characterize the optical properties of silicon, there exists only one publication of experimental data that covers the spectral range from 400 to 100 cm^{-1}. These data disagree significantly with extrapolations from other experimental efforts. The data presented here resolves this disagreement.

4.2 Previous Experimental Investigations

The optical properties of silicon have been well characterized for a wide range of dopant concentrations and temperatures (Timans, 1996). The review by Edwards (1985) provides the complex refractive indices of silicon from 16130 to 30 cm^{-1}.

This work is focused on the far-infrared optical properties of high-resistivity silicon, i.e., resistivities >1 Ω-cm. Most of the far-infrared high-resistivity silicon data available in the literature is included here. There are discrepancies among the existing data in the spectral range from 400 to ~100 cm^{-1} that this work aims to clarify.

Randall and Rawcliffe (1967) measured the complex refractive index of 10 Ω-cm Si from 150 to 20 cm^{-1} using a lamellar grating interferometer. They reported a nearly frequency-independent absorption coefficient, $\alpha = 4\pi\kappa\nu$, of ~0.5 cm^{-1}, with an accuracy of ±5% and a refractive index of ~3.418, which also exhibited a negligible frequency dependence.

Loewenstein et al. (1973) measured the transmittance of 100 Ω-cm Si at room temperature and 1.5 K between 350 and 30 cm^{-1} using an FT-IR equipped with a carbon bolometer designed to permit samples to be mounted inside the detector dewar, in close proximity to the detector element. They reported a 300 K absorption coefficient α which increases almost linearly from a minimum value of 0.4 cm^{-1} at 30 cm^{-1} to 3.4 cm^{-1} at 350 cm^{-1}, with an uncertainty of ±0.2 cm^{-1}. At 100 cm^{-1}, $\alpha = 0.9$ cm^{-1}. The 300 K index of refraction varies slightly from 3.4155 at 30 cm^{-1} to 3.4200 at 350 cm^{-1}, with an uncertainty of ±0.002. At 1.5 K, both quantities are reduced slightly, due to the reduction of the 600 cm^{-1} phonon wing contribution. The absorption coefficient increases linearly with increasing frequency: $\alpha(\nu = 30\text{ cm}^{-1}) = 0.1\text{ cm}^{-1}$ and $\alpha(\nu = 350\text{ cm}^{-1}) = 2.1\text{ cm}^{-1}$. The refractive index is approximately constant: $n(\nu = 30\text{ cm}^{-1}) = 3.3818$ and $n(\nu = 350\text{ cm}^{-1}) = 3.3878$.

Afsar and Hasted (1978) used a Martin-Puplett type polarization interferometer to measure the optical constants of 1 kΩ-cm silicon between 220 and 5 cm^{-1} at 4 °C, 30 °C and 57 °C. They determined a refractive index that is approximately constant at 3.42 from 220 to 50 cm^{-1} and an absorption coefficient which increases slowly with decreasing frequency. At 100 cm^{-1}, $\alpha = 0.36\ \text{cm}^{-1}$.

Birch (1978) determined the absolute complex refractive index for 1 kΩ-cm Si between 120 and 5 cm^{-1} using a transmission dispersive Fourier transform experiment. He found a refractive index $n = 3.4125 \pm 0.0002$, averaged across the investigated spectral range, and an absorption coefficient which increased strongly for wavenumbers less than 50 cm^{-1}, due to impurity-induced free-carrier absorption . At $\nu = 100\ \text{cm}^{-1}$, $\alpha = 0.40\ \text{cm}^{-1} \pm 0.05\ \text{cm}^{-1}$ and $\alpha(\nu = 10\ \text{cm}^{-1}) = 1.40\ \text{cm}^{-1} \pm 0.05\ \text{cm}^{-1}$.

Ohba and Ikawa (1988) measured the transmittance of 9.4 Ω-cm silicon crystals grown by the Czochralski (CZ) method and 10 kΩ-cm grown by the floating-zone (FZ) method for the spectral range from 200 to 20 cm^{-1} using synchrotron radiation as a far-infrared source and a Martin-Puplett interferometer. They observed a strong decrease in the transmittance of the CZ crystal with decreasing frequency, which was attributed to impurity-induced free-carrier absorption. The transmittance of the FZ crystal increased slightly with decreasing frequency, as the wing of the 600 cm^{-1} phonon band decreased in strength. An analysis of this data indicated that the refractive index is approximately constant for both samples, $n \approx 3.42$. At the high-frequency limit of the experiment, the absorption coefficient for both samples is approximately equal, $\alpha(\nu = 200\ \text{cm}^{-1}) \approx 0.33\ \text{cm}^{-1}$. At 100 cm^{-1}, the CZ crystal absorption coefficient increased to 0.5 cm^{-1}, while the FZ crystal absorption coefficient decreased to 0.1 cm^{-1}. The FZ crystal absorptance coefficient decreases further with decreasing frequency while the CZ crystal absorption coefficient increases strongly to $\alpha(\nu = 20\ \text{cm}^{-1}) \approx 6\ \text{cm}^{-1}$.

Grischkowsky et al. (1990) investigated the absorption and dispersion of 10 kΩ-cm silicon from 66 to 6.6 cm^{-1} using time-domain spectroscopy. The authors note the lack of agreement in the measured absorptivity data for wavenumbers less than 66 cm^{-1}, with variations of as much as 5 times among existing data. For relatively low doping levels with resistivities greater than 1 Ω-cm, the absorption for wavenumbers less than 66 cm^{-1} is proportional to carrier density and thereby inversely proportional to resistivity. The data presented by Grischkowsky et al (1990) agrees qualitatively with the results of Ohba and Ikawa (1988) for their 10 kΩ-cm FZ crystal. The absorption coefficient decreases moderately with decreasing frequency. The absorption coefficient measured by these two groups is significantly less than that measured by the groups mentioned previously, which they attribute to the significantly higher resistivity of the samples investigated.

The identical experimental arrangement was used by these authors to investigate *n*- and *p*-type Si, with resistivities of 0.1, 1, and 10 Ω-cm from 66 to 3.3 cm^{-1} (Van Exter and Grischkowsky, 1990). The absorption coefficient data presented by Van Exter and Grischkowsky (1990) for moderately doped Si agree qualitatively with the CZ crystal data of Ohba and Ikawa (1988). The absorption coefficient increased dramatically with decreasing frequency. They determined a maximum absorption coefficient of 12 cm^{-1} near the low-frequency limit, 3.3 cm^{-1}. The absorption coefficient begins to increase for wavenumbers less than 66 cm^{-1}, due to impurity- or dopant-induced free-carrier absorption. Both groups model this behavior with a simple Drude model. Van Exter and Grischkowsky (1990) extend the model by including a frequency-dependent scattering rate to account for some low-frequency deviations between the simple Drude model and their experimental data. These models are not used in the present work as they are fitted primarily for data at lower frequencies than are investigated here.

The investigations by van Exter and Grischkowsky (1990) and Ohba and Ikawa (1988) indicate that for silicon with a resistivity of ~10 Ω-cm, the absorption coefficient is small and constant at the low-frequency limit of the spectral range investigated in this work, ~100 cm^{-1}.

Gatesman et al. (1995) measured the optical properties of 40-60 kΩ-cm Si using ellipsometry with a CO_2 optically pumped molecular gas laser at four frequencies from ~100 to

~10 cm^{-1} with an accuracy of better than ±0.1%. At 84.94 cm^{-1}, they measured α = 0.07 ± 0.1 cm^{-1}. Their data are in good agreement with the work of Ohba and Ikawa (1988) and Grischkowsky et al. (1990).

The investigations presented here indicate that silicon with resistivities as large as 1 kΩ-cm exhibits a significant increase in the absorption coefficient for wavenumbers less than 50 cm^{-1} due to dopant-induced free-carrier absorption. For resistivities 10 kΩ-cm, the absorption coefficient decreases with decreasing frequency, indicating the absence of free-carrier absorption.

4.3 Experimental Results and Discussion

Figure 4.1 shows the measured room-temperature reflectance from 400 to 50 cm^{-1} for the 127 μm Si used in the reflection-Fabry-Pérot etalon experiments. Figure 4.2 shows the corresponding transmittance measurements. The measurements are performed using a Bruker IFS 66v FT-IR. The techniques for conducting room-temperature reflectance and transmittance measurements are described in detail in Chapter 3. Briefly, for the reflectance measurement, single-beam spectra for the silicon and a gold reference are measured using the FT-IR room-temperature reflection accessory, which focuses the infrared beam onto the sample surface, collects the specularly reflected beam and refocuses it onto a detector. The incidence angle for the infrared beam is approximately 10°. The ratio of the two spectra yields the silicon reflectance. The transmittance is measured using the transmittance accessory, which enables a sample to be placed perpendicular to the path of infrared radiation at a focal point of the infrared beam. A single-beam spectra is measured with the silicon sample in the beam path and another spectra is collected without the sample in the beam path. The ratio of these quantities gives the transmittance.

The single beam spectra are measured consecutively using an aperture setting of 1 mm, a resolution of 0.25 cm^{-1}, a zero-filling factor of 4, a Glowbar ceramic source, and a 6 μm polyethylene beamsplitter. The detector is a liquid-helium cooled silicon bolometer with an NEP of ~1 x 10^{-13} $W/Hz^{1/2}$. The FT-IR optical path is evacuated to ~1 x 10^{-3} torr. The duration of each

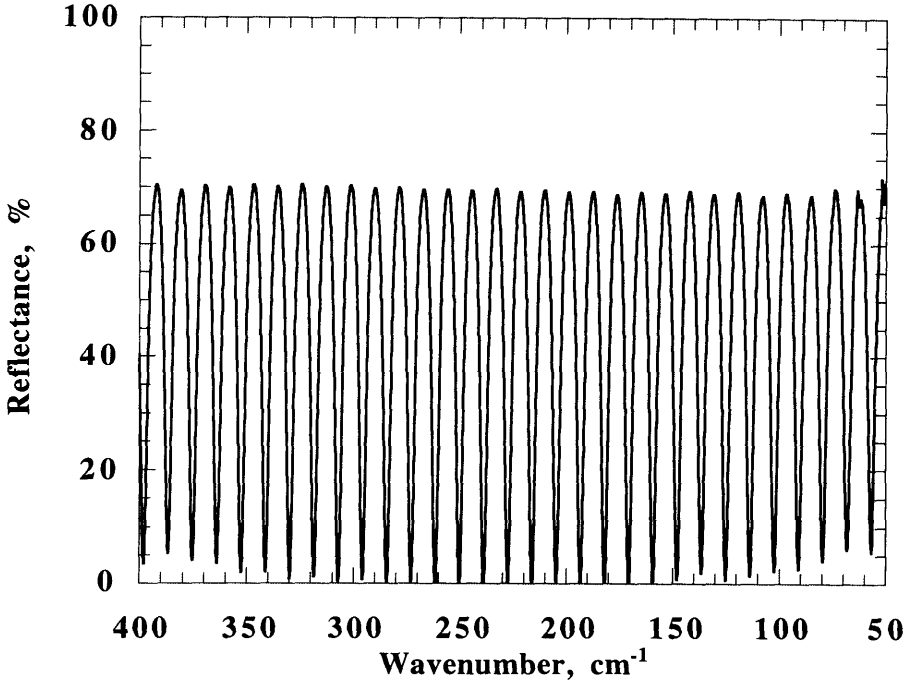

Figure 4.1 Measured reflectance of 127 μm thick silicon at 300 K.

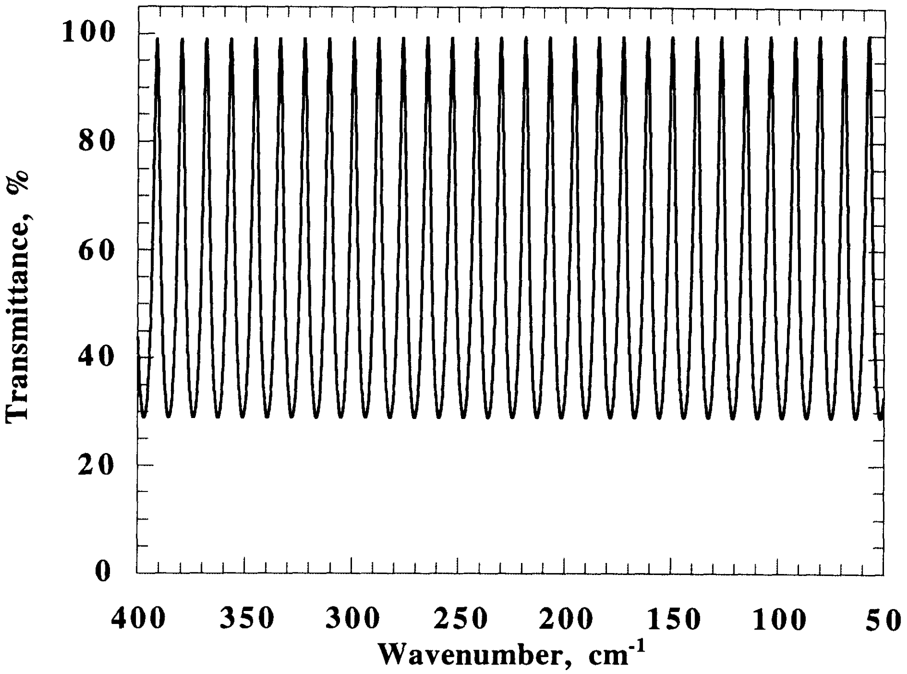

Figure 4.2 Measured transmittance of 127 μm thick silicon at 300 K.

measurement is approximately 2.6 hrs., consisting of 8000 scans at a scan speed of 100 Khz. The interferogram is multiplied by the Blackman-Harris four-term apodization function for all measurements to minimize the artificial side lobes caused by the limited resolution of the instrument. Of all the standard apodization functions used for FT-IR spectroscopy, the Blackman-Harris four-term function causes the smallest distortion in the experimental data. The drift in the bolometer signal over a 10-hour period for the evacuated FT-IR is approximately 0.2%. Errors in positioning the sample and reference in the same location in the infrared beam limit the photometric accuracy of these measurements to approximately ± 1%.

Figure 4.1 shows a near-uniform minimum and maximum reflectance across the displayed spectral range, with a maximum value of approximately 70% and a minimum value of approximately 0%. The average minimum reflectance is 1.03%, with a standard deviation of ±0.16%. For wavenumbers greater than 550 cm^{-1}, the spectrum is distorted by the 600 cm^{-1} multi-phonon band. The minimum reflectance rises slightly toward the limits of the displayed spectral range. This is due to signal-to-noise limitations caused by the beamsplitter and possibly due to the influence of the sample holder used for this measurement. Although the infrared beam was smaller than the lateral dimensions of the sample, 1 mm vs. 5 mm, it is possible that due to misalignment or beam diffraction, some of the beam interacted with the sample holder, causing a small increase in the reflectance minima.

The corresponding transmittance measurements displayed in Fig. 4.2 show a maximum transmittance in excess of 99% and ~28% minimum transmittance across the spectral range. The data exhibit little variation across the displayed spectral range. A decrease in the transmittance maxima with increasing frequency would indicate that free-carrier absorption is occurring in the film. This effect is not observed. The average maximum transmittance is 99.97%, with a standard deviation of ±0.82%. The average frequency spacing between transmittance maxima is 11.36 ±0.054 cm^{-1}. The photometric error in the experimental measurement of the transmittance is estimated to be better than ±0.5%. The transmittance data is not subject to the error in the reflectance data caused by limitations in the sample holder dimensions.

These two results confirm that the Si wafer is highly plane-parallel and that the resistivity is sufficiently large as to minimize free-carrier absorption by dopant electrons. The standard specification for eliminating the influence of geometric effects on the spectra is that the sample faces must be flat to better than $\lambda/4$ (visible) and parallel to a second of arc or better (Edwards, 1985). The samples used here exceed these specifications. If the material were less plane-parallel, the reflectance minima would have increased linearly with increasing wavenumber. The corresponding transmittance maxima would have decreased linearly. Genzel et al. (1993) found this limitation with the silicon used in their work. They derived an approximate analytical solution for correcting their data for a slight non-plane parallelism in the silicon wafer, as well as the non-vertical incidence and non-collimation of the infrared beam. The results presented in Figs. 4.1 and 4.2 indicate that these compensations are not required for experimental data measured in this work.

To compare the experimental data with a prediction based on the optical constants discussed in the previous section, a thin-film optics model is developed for the reflectance and transmittance of the silicon wafer. The silicon is modeled as a single homogeneous and isotropic absorbing layer sandwiched between two semi-infinite nonabsorbing media. Consider a monochromatic plane wave propagating in a nonabsorbing medium incident on the layer. Figure 4.3 shows the resultant multiple reflections occurring inside the idealized, optically smooth thin film with perfectly plane-parallel surfaces. This analysis is available in any optics text, e.g., Yeh (1988), and is considered in more detail in Chapter 2. Appendix A presents a matrix formulation for the radiative properties of a stack of any number of thin films.

At the first interface, the incident beam is partially reflected. The remainder is transmitted through the interface, where it is absorbed exponentially by medium 2. Some fraction of the transmitted energy reaches the second interface where part is reflected and the rest is transmitted into medium 3. The beam is subsequently reflected back and forth between the two interfaces as

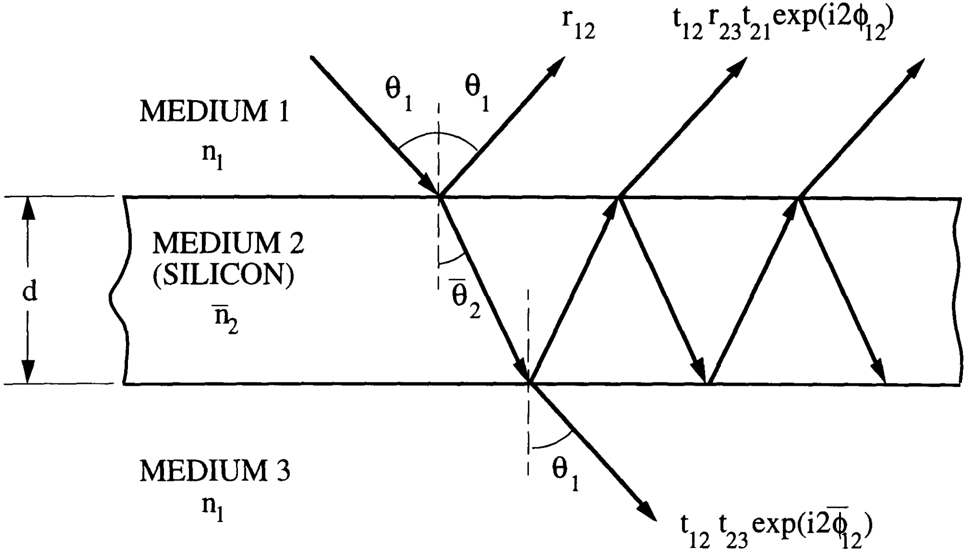

Figure 4.3 Multiple reflections occurring inside the idealized, optically smooth thin film with perfectly plane-parallel surfaces.

shown in the figure. Successive waves transmitted into medium 1 have a phase difference 2ϕ with respect to each other. Similarly, successive transmitted waves into medium 3 have a phase difference of 2ϕ. The waves interfere destructively or constructively based on the phase difference. For normal incidence, 2ϕ is:

$$2\phi = 4\pi\nu n_2 d \tag{4.1}$$

By adding the contributions from all the reflected and transmitted waves leaving the film, the amplitude of the reflected and transmitted waves for the film may be determined. The reflectance R_{film} and transmittance T_{film} of the film for normal incidence are determined by multiplying the total amplitude ratios r_{film} and t_{film} by their respective complex conjugates:

$$R_{\mathrm{film}} = \left|r_{\mathrm{film}}\right|^2 = \left|\frac{r_{12} + r_{23}\mathrm{e}^{i2\bar{\phi}}}{1 + r_{12}r_{23}\mathrm{e}^{i2\bar{\phi}}}\right|^2 \tag{4.2}$$

$$T_{\mathrm{film}} = \left|t_{\mathrm{film}}\right|^2 = \left|\frac{t_{12}t_{23}\mathrm{e}^{i\bar{\phi}}}{1 + r_{12}r_{23}\mathrm{e}^{i2\bar{\phi}}}\right|^2 \tag{4.3}$$

where r_{ij} and t_{ij} are the Fresnel coefficients for reflection and transmission, respectively, for a wave propagating in medium i toward medium j. The complex phase difference $2\bar{\phi} = 4\pi\nu\bar{n}_2 d$ includes both the phase difference between successive reflections and transmissions and the exponential attenuation of the wave as it crosses absorbing medium 2.

The reflectance and transmittance oscillate between maxima and minima as the phase difference changes by 2π. The film transmittance reaches a maximum for $2\phi = m\,2\pi$, where $m = 0,1,2,3...$ There is a corresponding reflectance minimum. The minimum reflectance and maximum transmittance are:

$$R_{\mathrm{film,min}} = \left|\frac{r_{12} - r_{23}\exp[-4\pi\nu\kappa_2 d]}{1 + r_{12}r_{23}\exp[-4\pi\nu\kappa_2 d]}\right|^2 \tag{4.4}$$

$$T_{\text{film,max}} = \left| \frac{t_{12}t_{23}\exp[-2\pi\nu\kappa_2 d]}{1 + r_{12}r_{23}\exp[-4\pi\nu\kappa_2 d]} \right|^2 \tag{4.5}$$

The frequency spacing $\Delta\nu$ between maxima is:

$$\Delta\nu = \frac{1}{2n_2 d} \tag{4.6}$$

The refractive index of the film may be determined from experimental data by measuring $\Delta\nu$. From the experimental data in Fig. 4.2, the average frequency spacing of 11.36 ± 0.05 cm^{-1} from transmittance data over-predicts the literature value of $n_2 \approx 3.42$. Given the 0.25 cm^{-1} resolution of the measurement of the measurement, n_2 is known within the range, $3.39 < n_2 < 3.54$. A spacing of 11.51 cm^{-1} predicts $n_2 = 3.42$. This spacing value is within the 0.25 cm^{-1} resolution of the measurement, so the refractive index of silicon is set at the literature value, $n_2 = 3.42$, as there is little dispute over this value in all studies.

The transmittance maxima and reflectance minima are influenced by the extinction coefficient κ_2. The transmittance maxima are much more strongly influenced by the choice of this parameter. Equation (4.5) is used to determine the approximate value for κ_2 appropriate for the silicon used in this work. Given that the experimental measurements yielded a negligible change from 100% across the spectral range, the experimental uncertainty of ±0.5% is used to determine this parameter, i.e., the maximum transmittance is set at 99.5% to determine a maximum value for κ_2.

Figure 4.4 shows the variation in the normal incidence maximum transmittance with κ_2 at ~391 cm^{-1} and ~104 cm^{-1}, the theoretical transmittance maxima at the frequency limits for the reflection-Fabry-Pérot experiment. The refractive index is set at $n_2 = 3.42$. The transmittance is lower for higher frequencies because the exponential term in Eq. (4.5) contains frequency ν. Based on the criterion of 99.5% maximum transmittance for the 391 cm^{-1} transmittance maximum, the extinction coefficient is set at $\kappa_2 = 4 \times 10^{-5}$ or $\alpha(391\ \text{cm}^{-1}) = 0.20$ cm^{-1}. As indicated in the

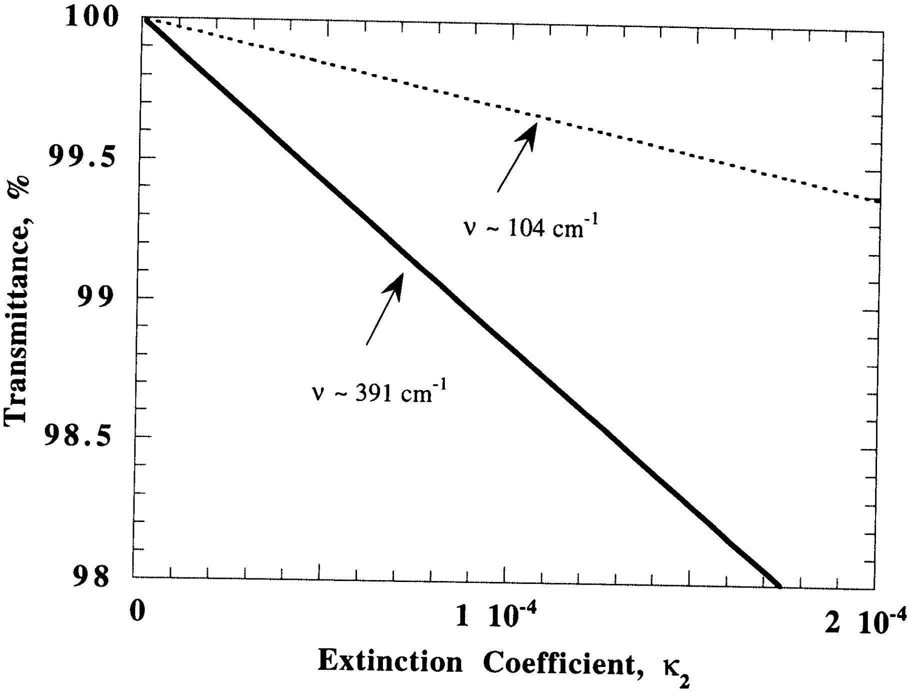

Figure 4.4 Predicted maximum normal-incidence transmittance of 127 μm thick silicon at 300 K at resonance frequencies at the experimental frequency limits versus silicon extinction coefficient for $n_{si} = 3.42$.

figure, $\kappa_2 = 1.5 \times 10^{-4}$ meets the 99.5% criterion at 104 cm^{-1} or $\alpha(103.605\ cm^{-1}) = 0.20.\ cm^{-1}$. Both of these values are in reasonable agreement with the tabulated values of $\kappa_2 = 2.9 \times 10^{-4}$ at 100 cm^{-1} and $\kappa_2 = 9.15 \times 10^{-5}$ at 400 cm^{-1} in the review by Edwards (1985), which were extrapolated the experimental findings of Johnson (1959). Johnson (1959) does not report the resistivity of his samples.

Table 4.1 presents the absorption coefficients at ~400 cm^{-1} and ~100 cm^{-1} for the present investigation and the investigations discussed in the previous section. Only Loewenstein et al. (1973) cover the entire spectral range of interest and their absorption coefficients are significantly larger than those determined here. As mentioned above, the findings presented here agree with the review of Edwards (1985) who extrapolated the experimental findings of Johnson (1959) to cover this spectral range and found significant disagreement with the data of Loewenstein et al. (1973). Loewenstein et al. (1973) suggested that there might be some surface damage to their silicon sample caused by polishing, resulting in the measurement of anomalously large absorption coefficients. Edwards (1985) omitted this work and published instead the extrapolation of Johnson's (1959) work. The experimental data presented here support Edward's work. This author could find no other published data for silicon for this spectral range that addressed this issue.

With the exception of Loewenstein et al. (1973), the absorption coefficient data at ~100 cm^{-1} vary as expected with sample resistivity. For samples with resistivities from 10 Ω-cm to 1 kΩ-cm, there is little change in the absorption coefficient, indicating that the free-carrier absorption from dopant atoms is large for this range of resistivities. Only resistivities of 10 kΩ-cm and larger exhibit insignificant free-carrier absorption at 100 cm^{-1}.

The predicted reflectance and transmittance for a 127 μm thick silicon film with $n_{Si} = 3.42$ and $\kappa_2 = 4 \times 10^{-5}$ are shown in Figs. 4.5 and 4.6. Varying κ_2 from 4×10^{-5} at 400 cm^{-1} to 1.5×10^{-4} at 100 cm^{-1} causes only a slight increase in the maximum transmittance and

Table 4.1 Summary of far-infrared silicon investigations.

Investigator	Si Resistivity	Spectral Range	Absorption Coefficient, α	
			$\nu = 400$ cm^{-1}	$\nu = 100$ cm^{-1}
Present Work	33.5 Ω-cm	400 - 100 cm^{-1}	0.20 cm^{-1}	0.20 cm^{-1}
Randall and Rawcliffe (1967)	10 Ω-cm	150 - 20 cm^{-1}	—	0.5 cm^{-1}
Loewenstein et al. (1973)	100 Ω-cm	350 - 30 cm^{-1}	3.4 cm^{-1}	0.9 cm^{-1}
Afsar and Hasted (1978)	1 kΩ-cm	220 - 5 cm^{-1}	—	0.36 cm^{-1}
Birch (1978)	1 kΩ-cm	120 - 5 cm^{-1}	—	0.40 cm^{-1}
Ohba and Ikawa (1988)	9.4 Ω-cm	200 - 20 cm^{-1}	—	0.5 cm^{-1}
	10 kΩ-cm	same	—	0.1 cm^{-1}
Grischkowsky and others (1990)	0.1, 1, and 10 Ω-cm; 10 kΩ-cm	66 - 3.3 cm^{-1}	—	0.05 cm^{-1} at 66 cm^{-1} (10 kΩ-cm)
Gatesman et al. (1995)	40-60 kΩ-cm	100 - 10 cm^{-1}	—	0.07 cm^{-1}

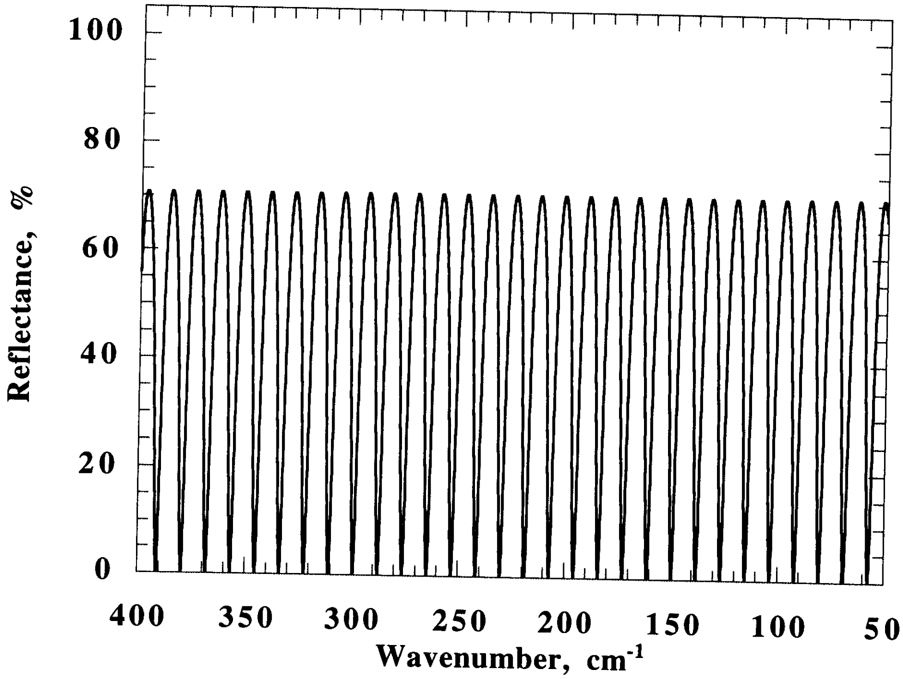

Figure 4.5 Predicted normal-incidence reflectance of 127 μm thick silicon at 300 K for $n_{\mathrm{Si}} = 3.42$ and $\kappa_{\mathrm{Si}} = 4 \times 10^{-5}$.

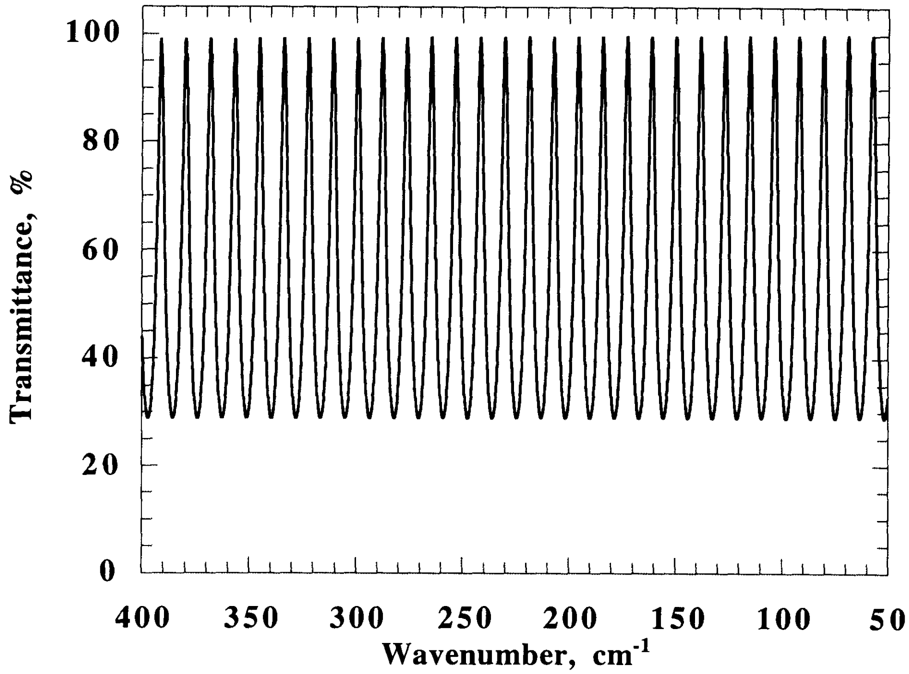

Figure 4.6 Predicted normal-incidence transmittance of 127 μm thick silicon at 300 K for n_{si} = 3.42 and κ_{Si} = 4 x 10^{-5}.

a decrease in the corresponding minimum reflectance with decreasing frequency.

4.4 Conclusions

The optical constants of the 127 μm-thick silicon used in this work are determined using reflectance and transmittance measured using an FT-IR for the spectral range from 400 to 100 cm^{-1}. For the first time, experimental data is presented which resolves a disagreement in the literature over the value of the absorption coefficient for this spectral range. The absorption coefficient is found to be 0.20 cm^{-1} for 33.5 Ω-cm silicon.

The resolution of the measurements is too large to accurately determine the refractive index, so the literature value of ~3.42 was chosen. There was little disagreement in any of the studies on this value.

CHAPTER 5

INFRARED RADIATIVE PROPERTIES OF GOLD

5.1 Introduction

Theoretical models for the temperature-dependent thermal radiative properties of gold are required for the accurate design of devices employing gold. The theoretical foundations of two models used to predict these properties are presented here: the Drude theory and the anomalous skin effect theory. These models are later applied to the experimental data collected in this work to determine their suitability for the accurate prediction of the radiative properties of gold. The limitations of these models and several more complex model are also discussed. Experimental data are presented at room temperature and liquid-helium temperature and compared to existing experimental data. Appropriate predictive models are recommended.

5.2 Skin Depth

Maxwell's equations are the starting point for analyzing the macroscopic electromagnetic field at interior points in matter. Faraday's law, Eq. (5.1), and Ampere's law, Eq. (5.2), written using the constitutive relations, i.e., Ohm's law, $\boldsymbol{J} = \sigma \boldsymbol{E}$, etc., are the most relevant expressions for this treatment:

$$\nabla \times \boldsymbol{E} = -\mu \frac{\partial \boldsymbol{H}}{\partial t} \tag{5.1}$$

$$\nabla \times \boldsymbol{H} = \sigma \boldsymbol{E} + \varepsilon \frac{\partial \boldsymbol{E}}{\partial t} \tag{5.2}$$

Applying Faraday's law and Ampere's law for the simplified case of a linearly polarized plane wave propagating through a medium along arbitrary direction z yields the following wave equation,

$$\frac{\partial^2 E_x}{\partial z^2} = \mu\varepsilon \frac{\partial^2 E_x}{\partial t^2} + \mu\sigma \frac{\partial E_x}{\partial t} \tag{5.3}$$

where E_x is the electric field polarized along the x-axis, μ is the magnetic permeability, ε is the permittivity, and σ is the electrical conductivity of the medium. The solution to Eq. (5.3) is a plane, time-harmonic wave,

$$E_x = E_{x0} e^{i(\bar{k}_z z - \omega t)} \tag{5.4}$$

where $\bar{k}_z$ is the complex wave number given by:

$$\bar{k}_z^2 = \omega^2 \mu \left(\varepsilon + i \frac{\sigma}{\omega} \right) = \omega^2 \mu \bar{\varepsilon} \tag{5.5}$$

The complex dielectric function $\bar{\varepsilon}$ defined above is related to the complex index of refraction by:

$$\bar{\varepsilon} = \varepsilon + i \frac{\sigma}{\omega} = \frac{\varepsilon_0 \mu_0}{\mu} \bar{n}^2 \tag{5.6}$$

where ε_0 and μ_0 are the electrical permittivity and magnetic permeability of free space, respectively.

The complex index of refraction $\bar{n}$ is defined as:

$$\bar{n} = n + i\kappa \tag{5.7}$$

where n is the index of refraction and κ is the extinction coefficient. From Eq. (5.6) the optical constants are related to the material properties by:

$$n=\sqrt{\frac{\mu}{2\mu_0\varepsilon_0}}\sqrt{\sqrt{\varepsilon^2+\frac{\sigma^2}{\omega^2}}+\varepsilon} \tag{5.8}$$

$$\kappa=\sqrt{\frac{\mu}{2\mu_0\varepsilon_0}}\sqrt{\sqrt{\varepsilon^2+\frac{\sigma^2}{\omega^2}}-\varepsilon} \tag{5.9}$$

Writing the expression for a plane, time-harmonic wave, Eq. (5.4) in terms of $\bar{n}$,

$$E_y=E_{y0}\mathrm{e}^{i\omega\left(\frac{n}{c_0}z-t\right)}\mathrm{e}^{-\frac{\omega\kappa}{c_0}z} \tag{5.10}$$

where c_0 is speed of light in vacuum,

$$c_0=\frac{1}{\sqrt{\varepsilon_0\mu_0}} \tag{5.11}$$

The real part of this expression,

$$E_y=E_{y0}\cos\left(\omega\left(\frac{n}{c_0}z-t\right)\right)\mathrm{e}^{-\frac{\omega\kappa}{c_0}z} \tag{5.12}$$

describes the electric field vector as a plane wave, given by the cosine term, with attenuation, given by the exponential term (Born and Wolf, 1980).

The skin depth δ is the length over which the amplitude of the electric field vector is reduced to $1/e$ of its original value. From Eq. (5.12), δ is,

$$\delta=\frac{c_0}{\omega\kappa}=\frac{\lambda_0}{2\pi\kappa} \tag{5.13}$$

Using Eq. (5.9), the skin depth may be rewritten in terms of the material properties, the permittivity and the electrical conductivity σ. At the dc limit, $\varepsilon \ll \sigma_{dc}/\omega$ and Eq. (5.14) reduces to:

$$\delta=\sqrt{\frac{2}{\mu\,\sigma_{dc}\omega}} \tag{5.14}$$

The Poynting vector S, the cross product of the electric and magnetic field vectors, is related to the energy flux of a propagating electromagnetic wave. The time-average $|S|_{\text{ave}}$ is:

$$|S|_{\text{ave}} = \frac{n}{2c_0\mu} E_{y0}^2 \exp\left(-\frac{z}{\delta_{\text{p}}}\right) \tag{5.15}$$

where δ_{p} is the penetration depth or the mean free photon pathlength (Brewster, 1992). This is the length over which the energy density decreases by $1/e$ of its original value,

$$\delta_{\text{p}} = \frac{c_0}{2\omega\kappa} = \frac{\lambda_0}{4\pi\kappa} = \sqrt{\frac{1}{\mu\,\sigma_{\text{dc}}\omega}} \tag{5.16}$$

5.3 Radiative Property Regimes

The derivation of the skin depth uses the constitutive relations, including Ohm's law, $J = \sigma(\omega)E$, which describes a local, instantaneous relationship between the electric field and the induced current. Ohm's law requires equilibrium, which is established by collisions between electrons and the lattice of the material (Wooten, 1972). Equilibrium is influenced by the scattering time, or the average time τ between collisions, and the frequency ω of the electric field acting on the electrons in the material. Four major regimes describe the interaction between electrons and photons in ω-τ space: 1) the classical skin effect; 2) the relaxation regime; 3) the anomalous skin effect; and 4) the extreme anomalous skin effect. Figure 5.1 shows the approximate boundaries between these regimes in ω-τ space and Fig. 5.2 qualitatively illustrates the interaction between the electrons and the electric field within the skin depth of a material. Figure 5.1 shows a fifth regime in which the electric field is transmitted through the material at sufficiently high frequencies. This presentation is based on the treatment by Wooten (1972).

When τ is sufficiently small such that the electrons undergo several collisions during the period of one oscillation of the electric field, i.e., $\omega\tau < 1$, the dc electrical conductivity correctly relates the induced current J to the electric field E. This situation is called the classical skin effect, and is characteristic of room-temperature metals in the very far infrared and millimeter wavelength

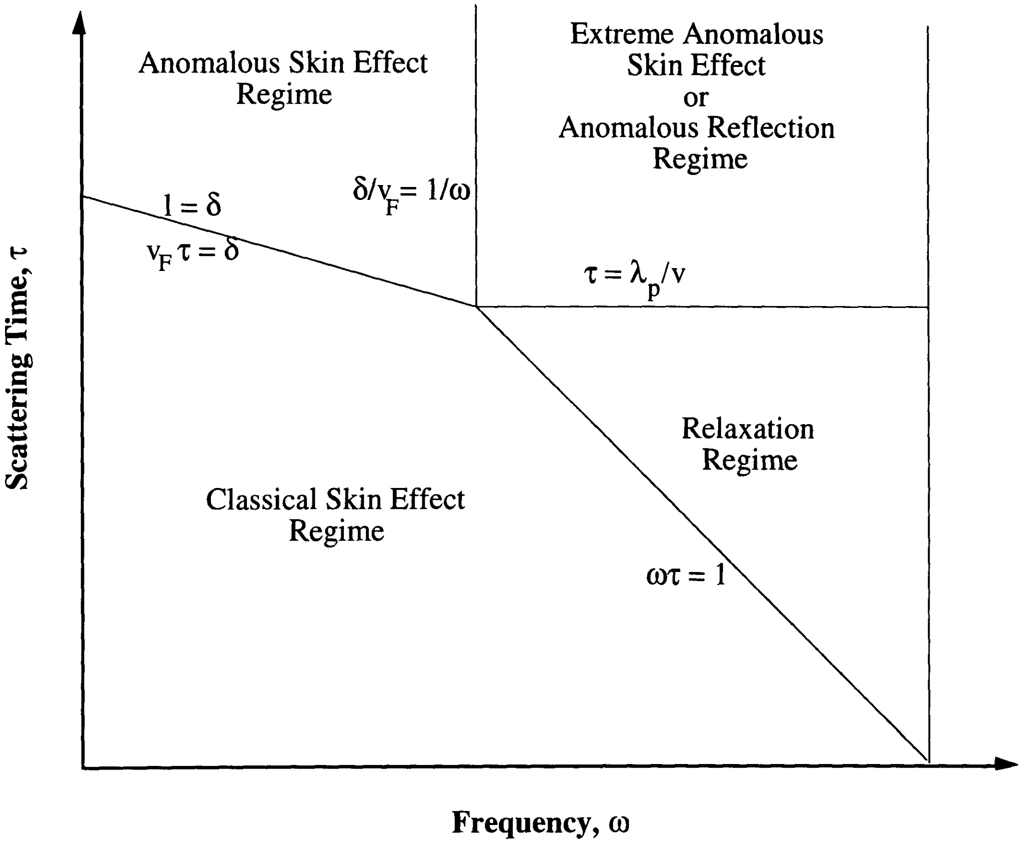

Figure 5.1 Schematic of scattering time versus frequency illustrating the four regimes of electron-photon interaction.

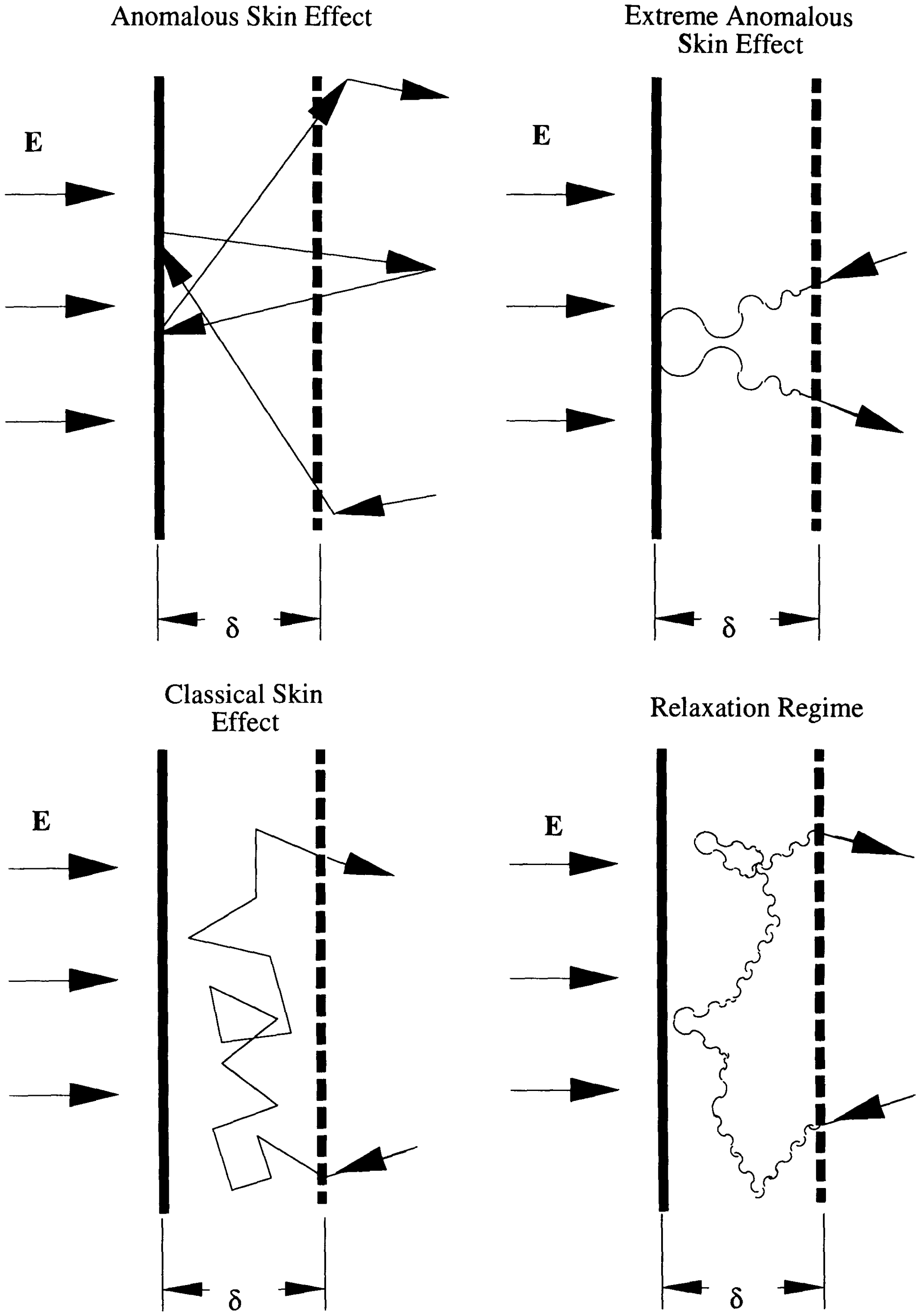

Figure 5.2 Interaction between the electric field and the material electrons for the four regimes shown in Fig. 5.1.

region. The electrons undergo many collisions during the time spent in the skin layer and during one period of the electric field, as illustrated in Fig. 5.2.

The relaxation regime occurs when τ is sufficiently small such that electrons undergo many collisions in the skin depth, but the frequency is large enough that the electric field oscillates many times between collisions, i.e., $\omega\tau > 1$. This is typical of room-temperature metals in the optical and infrared spectral ranges, below frequencies at which interband transitions become important. The dc electrical conductivity must be replaced with a frequency-dependent conductivity which accounts for the inertial effects of the electrons moving under the electric field. This behavior is modeled using the Drude free electron model described in the following section. The electrons screen the electric field resulting in a high reflectivity until the frequency is increased beyond the plasma frequency, where it becomes transparent.

If the scattering time is increased from the values which define the classical skin effect and relaxation regimes, thermal equilibrium between the electron and the lattice is not maintained, and Ohm's law is no longer valid. The electric field interacting with the electrons is not uniform in space. This situation defines the final two regimes: the anomalous skin effect regime and the extreme anomalous skin effect regime. A theory which considers the spatial non-uniformity of the electric field in the prediction of the optical properties of a metal is considered in Section 5.5.

At low frequencies, the anomalous skin effect regime can be reached from the classical skin effect regime by cooling a metal to cryogenic temperatures, which increases the scattering time. The transition from the classical skin effect regime to the anomalous skin effect regime occurs when the mean free path of the electrons l is of the same order as the skin depth δ. The mean free path is the lengthscale over which an electron travels between collisions, $l = v_F\tau$, where v_F is the Fermi velocity, the characteristic velocity of free electrons. In this regime, collisions are of little importance as the electron mean free path exceeds the skin depth, as shown in Fig. 5.2.

From the anomalous skin effect regime, increasing the electric field frequency eventually results in the electron experiencing oscillations of the electric field during the time it spends in the skin depth. The transition between the extreme anomalous skin effect, or the anomalous reflection regime, and the anomalous skin effect occurs when the ratio of the skin depth δ to the Fermi velocity v_F is approximately equal to the reciprocal of the electric field frequency, $\delta/v_F \approx 1/\omega$.

This regime is very similar to the relaxation regime, where the electrons in the skin layer respond to the electric field as essentially free electrons. However, in this regime, collisions occur much less frequently, and mostly at the interface. The boundary between this regime and the relaxation regime is defined as the equality between the mean free path and the skin depth, the condition at which lattice collisions are of equal importance with surface collisions. In this regime, the penetration depth is approximately equal to the plasma wavelength, so the boundary may be expressed as $l = \lambda_p$, or, $\tau = \lambda_p/v_F$.

5.4 Drude Free Electron Model

Free-carrier absorption is the dominant mechanism of absorption in the infrared portion of the electromagnetic spectrum for metals. The absorption processes are mainly intraband transitions, involving the excitation of an electron to another state within the same band. The Drude free electron theory models a material as an assembly of fixed, ionized metallic atoms and electrons which, due to their weak binding forces, are approximated as moving in a free manner. The theory ignores electron-electron and electron-ion electromagnetic interactions. The ion cores serve only as scattering sites.

The electrons are treated as classical charged particles under the influence of an applied electric field, with the assumption that the field does not vary in magnitude over the mean free path of the electron. Under the action of a linearly polarized incident electromagnetic field, a charged particle will experience a driving force. The magnitude of the driving force is the product of the particle charge, e, and the magnitude of the electric field vector, $\boldsymbol{E}(\boldsymbol{r},t)$ The driving force is opposed by the inertial force of the electron and a damping force. The damping force accounts for interactions between the electron and the medium. The damping force is represented by the product of the particle velocity, the electron mass m_e, and a damping term $1/\tau$, called the scattering rate.

Three assumptions are made for this model (Ashcroft and Mermin, 1976). First, the electrons travel in straight lines obeying Newton's laws between collisions. The electrons do not interact with the ion cores between collisions and electron-electron interactions are ignored. Second, the collisions are treated as instantaneous scattering events which abruptly change the velocity of the electron, i.e., the scattering event time is much shorter than any other times in the system. This is known as the relaxation time approximation where electrons emerge from a collision with no memory of its initial velocity. Electrons achieve thermal equilibrium only through collisions with ion cores and emerge from these collisions with velocities related to the temperature at the scattering location. Finally, all details of the scattering of electrons are summarized in the scattering time τ, which represents the time between collisions. Collisions occur between the electrons and ions and electrons and impurity atoms in the metal, although the actual scattering mechanism is unspecified in this theory.

The force balance on the particle is,

$$m_e \ddot{\boldsymbol{r}} + m_e\left(\frac{1}{\tau}\right)\dot{\boldsymbol{r}} = e\,\boldsymbol{E}(\boldsymbol{r},t) \tag{5.17}$$

The electric field vector is described by,

$$\boldsymbol{E}(\boldsymbol{r},t) = E_0 \mathrm{e}^{\mathrm{i}(\boldsymbol{k}\cdot\boldsymbol{r}-\omega t)} \tag{5.18}$$

Solving for $\boldsymbol{r}$(t),

$$\boldsymbol{r}(t) = \frac{-e}{m_e\left(\omega^2+\mathrm{i}\left(\frac{1}{\tau}\right)\omega\right)} E_0 \mathrm{e}^{-\mathrm{i}\omega t} \tag{5.19}$$

To relate this solution to the complex dielectric function of the material $\bar{\varepsilon}$, the electric polarization or the electric dipole moment per unit volume, $\boldsymbol{P}$, is introduced. By the constitutive relations for an isotropic medium,

$$\boldsymbol{P}(\boldsymbol{r}) = \varepsilon_0 \chi E_0\, \mathrm{e}^{-\mathrm{i}\omega t} = \varepsilon_0(\bar{\varepsilon} - 1)E_0\, \mathrm{e}^{-\mathrm{i}\omega t} \tag{5.20}$$

where $\bar{\chi}$ is the material complex electric susceptibility.

The electric polarization is related to the expression for the electron amplitude in Eq. (5.19) by:

$$\boldsymbol{P}(\boldsymbol{r}) = N_\mathrm{e} e \boldsymbol{r} \tag{5.21}$$

where N_e is the number of electrons per unit volume.

Combining Eqs. (5.19), (5.20), and (5.21), the complex dielectric function is given by:

$$(\bar{\varepsilon}\text{-}1) = -\frac{N_\mathrm{e} e^2}{\varepsilon_0 m_\mathrm{e}} \frac{1}{\omega^2 + \mathrm{i}\omega\left(\frac{1}{\tau}\right)} = -\frac{\omega_\mathrm{p}^2}{\omega^2 + \mathrm{i}\omega\left(\frac{1}{\tau}\right)} \tag{5.22}$$

where the plasma frequency ω_p is defined as:

$$\omega_\mathrm{p} = \sqrt{\frac{N_\mathrm{e} e^2}{\varepsilon_0 m}} \tag{5.23}$$

The real ε_r and imaginary ε_i components of the dielectric function are related to the refractive index n and the extinction coefficient κ as:

$$\varepsilon_\mathrm{r} = n^2 - \kappa^2 = 1 - \frac{\omega_\mathrm{p}^2}{\omega^2 + \left(\frac{1}{\tau}\right)^2} \tag{5.24}$$

$$\varepsilon_\mathrm{i} = 2n\kappa = \frac{\left(\frac{1}{\tau}\right)\omega_\mathrm{p}^2}{\omega^3 + \left(\frac{1}{\tau}\right)^2 \omega} \tag{5.25}$$

To write an expression for the complex conductivity of the medium, Ohm's law is employed,

$$\boldsymbol{J} = \sigma(\omega)\boldsymbol{E} \tag{5.26}$$

where $\sigma(\omega)$ is the frequency-dependent complex conductivity. The current density $\boldsymbol{J}$ is related to the equation of motion for the electron as:

$$\boldsymbol{J} = N_e e \frac{\mathrm{d}\boldsymbol{r}}{\mathrm{d}t} = \frac{N_e e^2}{m_e} \frac{\mathrm{i}\omega \boldsymbol{E}}{\omega^2 + \mathrm{i}\omega\left(\frac{1}{\tau}\right)} \tag{5.27}$$

Comparing Eqs. (5.26) and (5.27),

$$\sigma(\omega) = \frac{\sigma_{\mathrm{dc}}}{1 - \mathrm{i}\omega\tau} \tag{5.28}$$

where τ is the relaxation time and σ_{dc} is the dc conductivity,

$$\sigma_{\mathrm{dc}} = \frac{N_e e^2 \tau}{\mathrm{m_e}} \tag{5.29}$$

The dielectric function may be expressed in terms of the complex conductivity by comparing Eqs. (5.22) and (5.28),

$$\bar{\varepsilon} = 1 + \frac{\mathrm{i}\sigma(\omega)}{\omega\varepsilon_0} \tag{5.30}$$

5.5 Anomalous Skin Effect Theory

When the electric field varies appreciably over a distance comparable to the mean free path, thermal equilibrium between the electron and the lattice is not maintained, and Ohm's law is no longer valid. A non-local spatial relationship between the current and the electric field is described as the anomalous skin effect. The velocity of an electron depends upon the electric field at positions within the electron mean free path. The electron has a 'memory' of other fields at other positions.

This effect was first studied by Pipard (1947). He measured the surface resistance of silver, gold, and tin at low temperatures and noted a difference between these data and their corresponding bulk values. The measured surface resistance depends on the skin depth. When the skin depth is less than the mean free path, Ohm's law is not valid in the surface region where energy is absorbed.

Reuter and Sondheimer (1948) developed a method to calculate the surface impedance, $Z(\omega)$, of a semi-infinite metal based on the assumption that the free carriers move under the influence of a space- and time-dependent electric field. Their analysis does not include a photoelectric current, atomic polarization, and the displacement current, i.e., the current generated by the motion of bound charges under the action of an applied electric field. These effects are generally insignificant for metals for wavelengths greater than ~0.1 μm.

To determine the surface impedance in the anomalous skin effect regime, the frequency-dependent electric field distribution within the metal must be known. Reuter and Sondheimer (1948) solved a simplified version of the Boltzmann equation to determine the distribution function for the free electrons in the metal under the combined action of an applied electric field and electron-lattice scattering. The distribution function enables the determination of the space- and frequency-dependent current density. Substituting the current density into Maxwell's equations enables the determination of the space- and frequency-dependent electric field, in the form of an integro-differential equation. The electric field is then related to the metal surface impedance. The electromagnetic field considered is linearly polarized and propagates along a direction normal to the metal surface.

The distribution function is modeled as the linear combination of the Fermi-Dirac distribution function for free electrons in thermal equilibrium and a perturbation to the equilibrium distribution caused by the interactions experienced by the electrons. The collision term of the Boltzmann equation is simplified as the ratio of the perturbation to a scattering time τ. The collision mechanism is unspecified and it is assumed that the mechanism can always be described in terms of a free path, $l = \tau\bar{v}$, where $\bar{v}$ is the mean velocity of the electrons under consideration.

A solution for the distribution function requires a boundary condition at the metal-vacuum interface. Reuter and Sondheimer (1948) followed the phenomenological approach of Fuchs (1938). A reflection coefficient p is defined for the interaction between the electrons and the interface, which represents the fraction of electrons which are reflected specularly at the interface. When $p = 1$, all of the electrons are reflected specularly, with conservation of their momentum, whereas $p = 0$ indicates that all of the electrons are reflected diffusely, with a complete loss of their momentum.

The current density is proportional to the product of the electron density and velocity. With the expression for the distribution function, the current density may be determined. This result is used in Maxwell's equations to solve for the electric field vector, $E_x(\omega, z)$, where z is the axis, perpendicular to the metal surface, along which the electromagnetic wave propagates. The final solution for the electric field is the following integro-differential equation,

$$\frac{\mathrm{d}^2 E}{\mathrm{d} z^2} + \frac{\omega^2}{c_0^2} E = \frac{8\pi^2 i\omega e^2 m_e^2 \bar{v}^2}{c_0^2 \hbar^3} \left\{ p \int_{-\infty}^{\infty} k_a\left(\frac{z-t}{l}\right) E(t)\,\mathrm{d}t + (1-p) \int_0^{\infty} k_a\left(\frac{z-t}{l}\right) E(t)\,\mathrm{d}t \right\} \tag{5.31}$$

where $\hbar$ is Planck's constant and k_a is the integral over the polar coordinate θ^* for $a = \omega\tau$,

$$k_a(u) = \int_0^{\pi/2} \sec\theta^* \sin^3\theta^* \exp\left[-(1+ia)|u| \sec\theta^*\right] \mathrm{d}\theta^* \tag{5.32}$$

Since the wave propagation is no longer exponential, the classical concept of the complex index of refraction as derived in Section 5.2 is no longer valid. The optical properties of the metal can be expressed in terms of the complex surface impedance $Z(\omega)$. The surface impedance for normal incidence is defined as the ratio of the electric field at the metal surface to the total current density integrated over the depth into the metal,

$$Z(\omega) = R(\omega) + iX(\omega) = \frac{E_x(0)}{\int_0^\infty J(z)dz} \tag{5.33}$$

where $R(\omega)$ is the surface resistance and $X(\omega)$ is the surface reactance.

To relate the complex refractive index $\bar{n}$ to $Z(\omega)$, the displacement current term is ignored and Ampere's law, Eq. (5.2) is rewritten in terms of $\boldsymbol{J}$. The electric field is linearly polarized along the x-axis and propagates along the z-axis, perpendicular to the metal surface,

$$-\frac{\mathrm{d}H_y(z)}{\mathrm{d}z} = J(z) \tag{5.34}$$

Substituting this expression into Eq. (5.33),

$$Z(\omega) = \frac{E_x(0)}{H_y(0)} \tag{5.35}$$

Using Faraday's law, Eq. (5.1), $Z(\omega)$ is written as,

$$Z(\omega) = \frac{E_x(0)}{\left(\frac{1}{\mu i\omega}\right)\frac{\mathrm{d}E_x(0)}{\mathrm{d}z}} = \frac{\mu c_0}{\bar{n}} \tag{5.36}$$

Using the continuity of the transmitted and reflected electric field vectors at the metal surface and Kirchoff's law for the transmitted and reflected current densities, an expression for the metal directional-hemispherical spectral reflectivity at normal incidence is written as,

$$\rho'_{s,p,\omega}(\theta = 0) = \left|\frac{Z_0 - Z}{Z_0 + Z}\right|^2 \tag{5.37}$$

where θ is the angle of incidence from the surface normal and Z_0 is the impedance of free space.

Dingle (1953) provided series solutions to the integro-differential equations of Reuter and Sondheimer (1948) for the limiting cases of p, the fraction of electrons scattered specularly: $p = 0$, where all of the electrons are scattered diffusely, and $p = 1$, where all of the electrons are scattered specularly. The solution is presented in CGS units. The input parameters for the series solutions are the number density of free electrons, N_e, the effective electron mass, m_e, and dc electrical conductivity, σ_{dc}. The series solutions for the non-dimensional surface impedance $\overline{Z}_p$ are:

Specular Limit, $p = 1$:

$|\xi| \le 0.8$

$$\begin{aligned}\frac{W\overline{Z}_{p=1}}{i} \approx\ & 0.8660\,\xi^{-1/2} + 0.1155\,\xi^{1/2} - 0.1667\xi + 0.2210\,\xi^{3/2} - 0.2910\,\xi^{2} + 0.3815\,\xi^{5/2} \\ & -0.5040\,\xi^{3} + 0.6688\,\xi^{7/2} - 0.8920\,\xi^{4} + 1.1930\,\xi^{9/2} - 1.600\,\xi^{5}\ldots\end{aligned} \tag{5.38}$$

$|\xi| \ge 0.8$

$$\begin{aligned}\frac{W\overline{Z}_{p=1}}{i} \approx\ & 0.7698(\pi\xi)^{-1/3} + 0.6534(\pi\xi)^{-2/3} + (\pi\xi)^{-1} + \{0.1318\ln(\pi\xi) + 0.0852\} \\ & -0.1325(\pi\xi)^{-4/3} + 0.1983(\pi\xi)^{-5/3} + (\pi\xi)^{-2}\{0.0819\ln(\pi\xi) - 0.0788\} \\ & -0.1047(\pi\xi)^{-7/3}\ldots\end{aligned} \tag{5.39}$$

Diffuse Limit, $p = 0$:

$|\xi| \le 0.8$

$$\begin{aligned}\frac{i}{W\overline{Z}_{p=0}} \approx\ & 1.1547\,\xi^{1/2} - 0.2500\,\xi + 0.1540\,\xi^{3/2} - 0.1262\,\xi^{2} + 0.1188\,\xi^{5/2} \\ & -0.1214\,\xi^{3} + 0.1307\,\xi^{7/2} - 0.1840\,\xi^{4} + 0.1685\,\xi^{9/2}\ldots\end{aligned} \tag{5.40}$$

$|\xi| \ge 0.8$

$$\begin{aligned}\frac{i}{W\overline{Z}_{p=0}} \approx\ & 1.1547(\pi\xi)^{1/3} - \{0.1351\ln(\pi\xi) + 0.5330\} + 0.0416(\pi\xi)^{-1/3} \\ & -0.0649(\pi\xi)^{-2/3} + (\pi\xi)^{-1} - \{0.0164\ln(\pi\xi) - 0.0184\} \\ & +0.0660(\pi\xi)^{-4/3} - 0.0307(\pi\xi)^{-5/3}\ldots\end{aligned} \tag{5.41}$$

where $\bar{Z}$ is the dimensionless surface impedance, ξ is related to the electric current, $\bar{\sigma}$ is the dimensionless dc conductivity, $\bar{\nu}$ is the dimensionless frequency, and $\bar{V}$ is the dimensionless Fermi velocity:

$$\bar{Z} = \left(\frac{c_0}{4\pi\bar{\sigma}\bar{\nu}\mu\bar{V}}\right)Z \tag{5.42}$$

$$W = 1 + i\bar{\sigma}\,\bar{\nu} \tag{5.43}$$

$$\xi = \frac{\mathrm{i}\bar{\sigma}^3\bar{\nu}}{\left(1 + \mathrm{i}\bar{\sigma}\,\bar{\nu}\right)^3} \tag{5.44}$$

$$\bar{\sigma} = \sqrt{\frac{3\pi m_\mathrm{e}\mu}{N_\mathrm{e} e^2}}\,\bar{\mathrm{V}}\sigma_\mathrm{dc} \tag{5.45}$$

$$\bar{\nu} = \frac{2}{3V}\sqrt{\frac{3\pi m_\mathrm{e}}{N_\mathrm{e} e^2\mu}}\;\nu \tag{5.46}$$

$$\bar{V} = \frac{v_\mathrm{F}}{c_0} \tag{5.47}$$

$$v_\mathrm{F} = \frac{h}{m_\mathrm{e}}\left(\frac{3N_\mathrm{e}}{8\pi}\right)^{1/3} \tag{5.48}$$

The analysis of Reuter and Sondheimer and of Dingle consider the incident electric vector to be normal to the metal surface. For oblique incidence, the electric field varies in two dimensions. Thus, there is difference in the surface impedance for the p-polarized electric field compared to the s-polarized electric field, which always agrees with the analysis for a normal-incidence electric field, regardless of the incidence angle. However, Reuter and Sondheimer (1948) indicate that the difference is very small under the conditions where the displacement current may be ignored. Collins (1958) examined this simplification in detail and extended the analysis to consider the surface impedance for oblique incidence where the displacement current must be considered.

As mentioned above, the displacement current may be safely ignored in the infrared spectral range. The series solutions by Dingle presented above ignore the displacement current and so, the surface impedance values determined above may be related to the complex refractive index using Eq. (5.36). The polarization-dependent reflectivity for oblique incidence may be determined using the Fresnel reflection coefficients for an isotropic medium, which are presented in any introductory optics text. At the interface between vacuum and a non-magnetic material ($\mu = \mu_0$), the *s* and *p* wave directional-hemispherical spectral reflectivities are given by:

$$\rho'_{s,\omega}(\theta) = \left| \frac{Z\cos\theta - \sqrt{Z_0^2 - Z^2 \sin^2\theta}}{Z\cos\theta + \sqrt{Z_0^2 - Z^2 \sin^2\theta}} \right|^2 \tag{5.49}$$

$$\rho'_{p,\omega}(\theta) = \left| \frac{Z_0^2\cos\theta - Z\sqrt{Z_0^2 - Z^2 \sin^2\theta}}{Z_0^2\cos\theta + Z\sqrt{Z_0^2 - Z^2 \sin^2\theta}} \right|^2 \tag{5.50}$$

5.6 Other Theoretical Models

The anomalous skin effect is a purely classical model which does not consider the quantum mechanical interactions between electromagnetic waves and the free electrons of the metal. As with the Drude theory, the anomalous skin effect theory does not specify the electron scattering mechanism.

Holstein (1954) developed an expression for phonon-assisted absorption, called the bulk absorption, which adds another absorption mechanism to the surface collision absorption mechanism which the anomalous skin effect considers. Holstein modeled the absorption mechanism as a two-stage process consisting of the simultaneous absorption (or emission) of a photon and the emission (or absorption) of a phonon by an electron. The Debye model is used for the phonon spectrum. The analysis yields an effective scattering rate for the bulk absorption mechanism.

The result is valid in the limit $\hbar\omega >> k_B\theta >> k_BT$, where $\hbar$ is the reduced Planck's constant, ω is the frequency of the electromagnetic wave, k_B is the Boltzmann constant, θ is the Debye temperature of the metal ($\theta = 180$ K for gold), and T is the metal temperature. The energy required for the generation of a phonon is $\sim k_BT$. In the limit $k_B\theta >> k_BT$, very few phonons are generated by the thermal energy of the metal. This limit is satisfied when the metal temperature is reduced to liquid-helium temperature. In this low-temperature limit, phonons may be generated by electromagnetic radiation. When the energy of the electromagnetic wave $\hbar\omega$ exceeds the Debye energy, $k_B\theta$, i.e., $\hbar\omega >> k_B\theta$, the entire Debye phonon frequency spectrum is excited. This is the requirement for the validity of the Holstein bulk absorption model.

Writing the above limit in terms of wavelengths, we get $\lambda << \lambda_\theta << \lambda_T$. At the high-frequency limit of the liquid-helium temperature experiments performed in this work, $\lambda = 20\ \mu\text{m}$, the limit $\lambda \ll \lambda_\theta$ is not sufficiently satisfied: $(\lambda \approx 20\ \mu\text{m}) << (\lambda_\theta \approx 80\ \mu\text{m}) << (\lambda_T \approx 3400\ \mu\text{m})$. The Holstein model is valid only in the visible and near-infrared spectral range. Toscano and Cravalho (1976) report a prediction for the absorptance of gold films at 4.2 K made using the Holstein model for wavelengths less than ~15 μm. The Holstein model, with diffuse scattering at the metal surface, predicts an absorptance approximately 0.2% higher than the diffuse-scattering anomalous skin effect model. The Holstein model has some theoretical inconsistencies that are discussed by Toscano (1973). Since the model is not valid for the spectral region investigated in this work, no further discussion is presented here.

Gurzhi (1958) extended Holstein's approach by accounting for an electric field that varies with position and allowing for other types of electron interactions, e.g., electron-electron, and electron-impurity. His model, again, is only valid in the visible and near-infrared.

McKay and Rayne (1976) measured the infrared absorptivity of electropolished bulk samples of the noble metals from 1.7 μm to 3.5 μm over a temperature range from 10 K to

310 K using normal-incidence calorimetry. The Holstein model agreed well with the experimental data when the anisotropy of the electron-phonon scattering over the Fermi surface was considered.

Beach and Christy (1977) and Parkins (1978) measured the reflectance of copper, silver, and gold from 0.35 μm to ~3 μm at 77 K, 295 K, and 425 K. Parkins et al. (1981) applied the Drude model with a frequency- and temperature-dependent scattering rate to the experimental data. The scattering rate was modeled as the sum of the Holstein electron-phonon model and Gurzhi's model for electron-electron interaction.

No theoretical model was found which would account for quantum-mechanical absorption mechanisms in the spectral range investigated in this work. The low-temperature experimental absorptance data presented later in this chapter are larger than that predicted by the diffuse-scattering anomalous skin effect. This indicates that, possibly, an additional absorption mechanism must be included in a predictive model for the low-temperature absorptance of gold.

5.7 Physical Parameters for the Predictive Models

At room temperature, the electrical resistivity of most metals is predominantly due to collisions between the free electrons and the lattice phonons. As the temperature of the metal approaches absolute zero, the electrical resistivity is dominated by collisions with lattice defects and impurity atoms. Mattheissen's rule expresses the temperature-dependent net resistivity $\rho(T)$ in the presence of these two independent contributions as the sum of the individual resistivities (Kittel, 1976),

$$\rho(T) = \rho_\mathrm{l}(T) + \rho_\mathrm{i} \tag{5.51}$$

where $\rho_\mathrm{l}(T)$ is the temperature-dependent resistivity due to electron-phonon scattering, and ρ_i is the residual resistivity caused by lattice defect- and impurity atom-scattering, which has a very weak temperature dependence.

The Bloch-Grüneisen formula (Ziman, 1963; MacDonald, 1956) is used to model $\rho_\mathrm{l}(T)$,

$$\frac{\rho_\mathrm{l}(T)}{\rho_\mathrm{l}(T = 273\ \mathrm{K})} = \left(\frac{T}{273}\right)^5 \frac{J_5(\theta/T)}{J_5(\theta/273)} \tag{5.52}$$

where θ is the Debye temperature and $J_5(\theta/T)$ is a Debye integral defined below. For gold, $\theta =$ 180 K (Burns, 1990). The Debye temperature is derived by fitting experimental specific heat data, c_v, to the Debye formula,

$$c_\mathrm{v} = 9 n_\mathrm{i} k_\mathrm{B} \left(\frac{T}{\theta}\right)^3 J_4(\theta/T) \tag{5.53}$$

where n_i is the ion density, k_B is the Boltzmann constant, and $J_4(\theta/T)$ is a Debye integral defined generally as $J_\mathrm{p}(q)$,

$$J_\mathrm{p}(q) = \int_0^q \frac{(q')^\mathrm{p}\, e^{q'}}{\left(e^{q'} - 1\right)^2} \mathrm{d}q' \tag{5.54}$$

Note that ρ_l is very small for $T < \theta/10$. The residual resistivity ρ_i is equal to the extrapolated resistivity at 0 K because $\rho_\mathrm{l}(T)$ is vanishingly small at low temperatures. Thus, ρ_i is an approximation of the purity of a sample. At high temperatures, the net resistivity is dominated by $\rho_\mathrm{l}(T)$.

The Bloch-Grüneisen formula is not the most rigorous predictions for the temperature dependence of the electrical resistivity. However, the predictions are in excellent agreement with experimental results for a wide range of metals.

To estimate the temperature-dependent net resistivity $\rho(T)$ for gold requires the resistivity at 273 K, the Debye temperature $\theta = 180$ K, and the residual resistivity ρ_i. The values chosen for $\rho_\mathrm{l}(T = 273\ \mathrm{K})$ and ρ_i strongly influence the predicted values for radiative properties. To model the radiative properties of gold, literature values are chosen: $\rho_\mathrm{l}(T = 273\ \mathrm{K}) = \rho(T = 273\ \mathrm{K}) =$ $2.06 \times 10^{-8}\ \Omega$-m and $\rho_\mathrm{i} = 1.75 \times 10^{-11}\ \Omega$-m. (MacDonald, 1956). More recent measurements of the resistivity of polycrystalline samples of gold between 0.04 K and 7 K yielded results similar to the residual resistivity chosen for this work (Khoshenevisan et al., 1979).

Literature values for the electron carrier density, $n_e = 5.9 \times 10^{28}$ m^{-3} and the effective electron mass to the electron rest mass ratio, $m_e^*/m_e \approx 1$ (Burns, 1990; Ashcroft and Mermin, 1976) were chosen. Table 5.1 summarizes the physical parameters chosen for the radiative property predictive models for gold.

5.8 Gold Film Sample Preparation

Gold films are obtained from two sources, a deposition system at Lincoln Laboratory and a similar system at the Microsystems Technology Laboratory at MIT. Both films are deposited at room temperature using high-vacuum vapor deposition systems. The gold vapor is generated using an electron beam. The adherence of gold to most substrates is poor, so for continuous films, a buffer layer is required. The gold films are much thicker than the skin depth of the incident infrared electric field, so the buffer layer does not influence the measured radiative properties.

The Lincoln Laboratory film is approximately 3000 Å thick. It is deposited over a 100 Å Ti buffer layer on an atomically smooth 2" silicon wafer, 127 μm thick, polished on both sides. The gold billet used in the deposition has a purity of 99.999+%. The background pressure of the deposition system is ~2 x 10^{-7} torr. The deposition rate is optimized to minimize surface roughness. Based on results obtained for similar films fabricated using this system, the film roughness is approximately 200 Å.

The MIT film is 5770 Å thick, deposited over a 100 Å Cr buffer layer on an atomically smooth 4" silicon wafer, 500 μm thick, polished on both sides. The gold billet purity is 99.999%. The background pressure of the deposition system was approximately 10^{-7} torr. Again, the deposition rate is optimized to minimize surface roughness. The film is specular, so the surface roughness is much less than 0.4 μm.

The influence of deposition conditions on the radiative properties of metallic films has been thoroughly investigated. Bennett and Bennett (1967) discuss the effect of substrate preparation,

Table 5.1 Physical parameters for gold for the Drude and anomalous skin effect theories.

$\rho(273\ \mathrm{K})$	ρ_i	θ	n_e	m_e^*/m_e
$2.06 \times 10^{-8}\ \Omega\ \mathrm{m}$	$1.75 \times 10^{-11}\ \Omega\ \mathrm{m}$	180 K	$5.9 \times 10^{28}\ \mathrm{m}^{-3}$	1

deposition technique, deposition rate, etc. on the radiative properties of the resultant metal film. Of all common methods for producing metal films, vapor deposition was found to produce the best results, with physical properties similar to single crystal samples. Billet purities of 99.999% were found to yield films with reproducible radiative properties.

The deposition background pressure was identified as the one of the most sensitive parameters for controlling the radiative properties of metal films. Bennett and Bennett (1967) compared the near- and mid-infrared spectral emittance measurements of Hass and Hadley (1963) for gold films deposited under high vacuum, i.e., 10^{-5} torr, to measurements for their own films (Bennett and Ashley, 1965) deposited under an ultrahigh vacuum of 10^{-9} torr. The emittance of the films deposited in ultrahigh vacuum was found to be more than twice as small as the high-vacuum films in the mid-infrared. The films examined in this work were prepared at an intermediate deposition pressure.

The data of Bennett and Ashley (1965) and Hass and Hadley (1963) are compared with the experimental data from the present investigation in Section 5.9. It is evident from the discussion in Bennett and Bennett (1967) that the films examined in this work are of the highest quality.

5.9 Room-Temperature Experimental Results

5.9.1 Experimental Data

The room-temperature reflectance of two silicon-on-gold reflection Fabry-Pérot etalon samples are presented here. One gold sample, labeled MIT#1, was cut from the wafer prepared at MIT and the other sample, BI#9, was cut from the wafer prepared at Lincoln Laboratory. The reflectance of sample MIT#1 was measured using the room-temperature reflectance accessory described in Chapter 3 and the reflectance for sample BI#9 was measured using the low-temperature reflectance accessory, which is also described in Chapter 3. Data measured at 6 K for sample BI#9 are presented in Section 5.10.

Figure 5.3 shows the single-beam spectra for the etalon stack containing sample MIT#1 and the gold reference for the spectral range from 400 to 100 cm^{-1}. The data are gathered using the standard far-infrared FT-IR arrangement described in detail Chapter 3. The collection time for both spectra is approximately 2.6 hrs., consisting of 8000 scans measured using a liquid-helium cooled bolometer at a scan rate of 100 kHz. The sample and reference are positioned in approximately the same location in the infrared beam, so the single beam spectra overlap at the etalon sample resonance maxima. As discussed in Chapter 2, the reflectance of the etalon sample at the resonance maxima equals the reflectance of the sample. So, at the resonance maxima, the reflectance should equal approximately 100%. This is evident in Fig. 5.4, which shows the reflectance of this structure.

Figure 5.5 shows the reflectance spectra for the etalon stack containing sample BI#9. The sample and reference are measured using the same parameters as above. Note that the data exhibits more noise than Fig. 5.4. This is because the sample is mounted inside the cryostat. For this arrangement, the infrared beam passes twice through a wedged polyethylene window as it travels to the detector. This decreases the signal-to-noise of the measurement relative to the previous set of data.

Figure 5.6 shows the absorptance for samples BI#9 and MIT#1 extracted from reflectance spectra in Figs. 5.4 and 5.5. The absorptance is determined using the methods described in Chapter 2. The error bars for the data are determined to be approximately ±20%. The figure also shows an absorptance prediction made using the diffuse reflection anomalous skin effect theory, which provides the best agreement with the data.

The absorptance data for the two sample agree very well over investigated spectral range. The two high-quality gold samples prepared with different deposition systems yield very similar absorptance data. This agreement provides confidence in the reliability of the experimental technique.

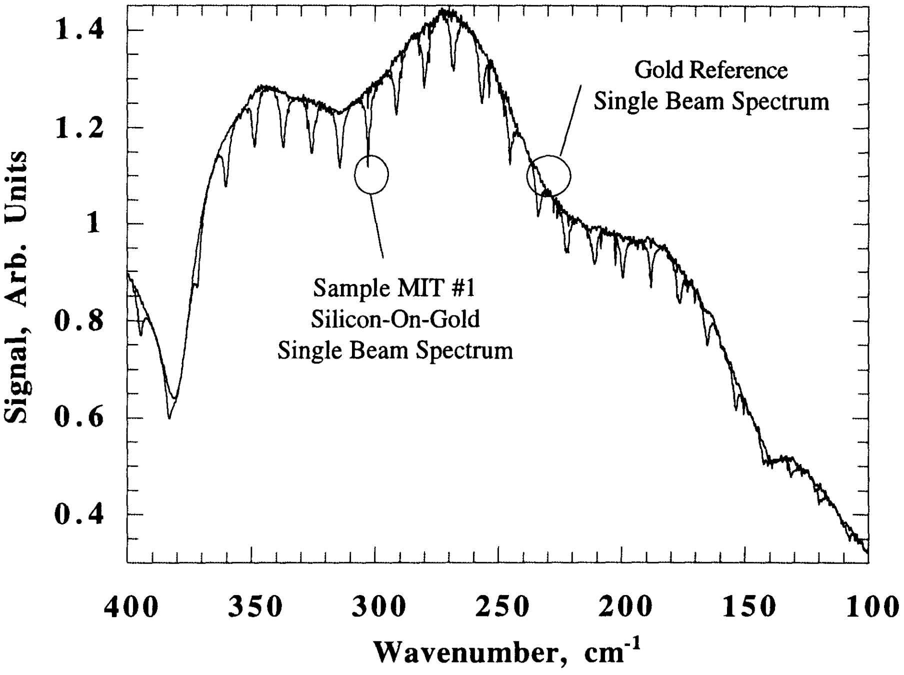

Figure 5.3 Single-beam spectra for silicon-on-gold reflection Fabry-Pérot etalon (sample MIT#1) and gold reference at 300 K.

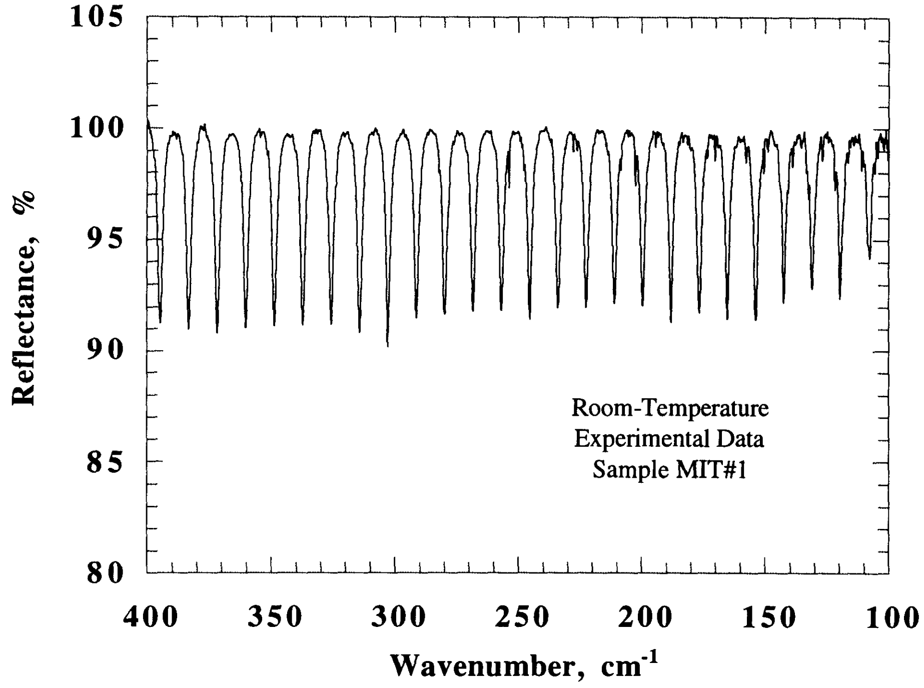

Figure 5.4 Reflectance of a silicon-on-gold reflection Fabry-Pérot etalon (sample MIT#1) at 300 K.

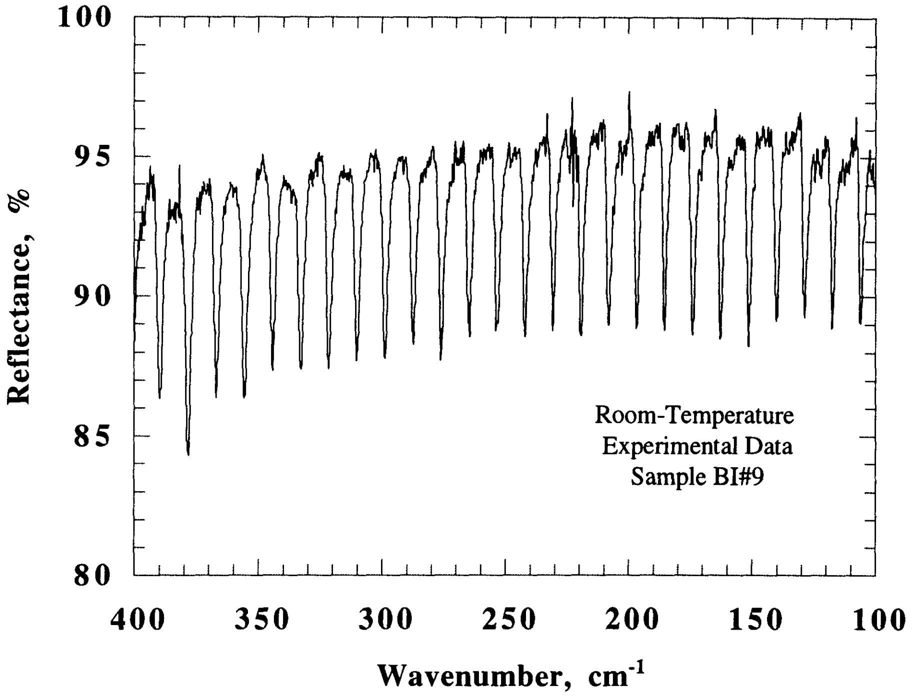

Figure 5.5 Room-temperature reflectance of silicon-on-gold reflection Fabry-Pérot etalon for sample BI#9.

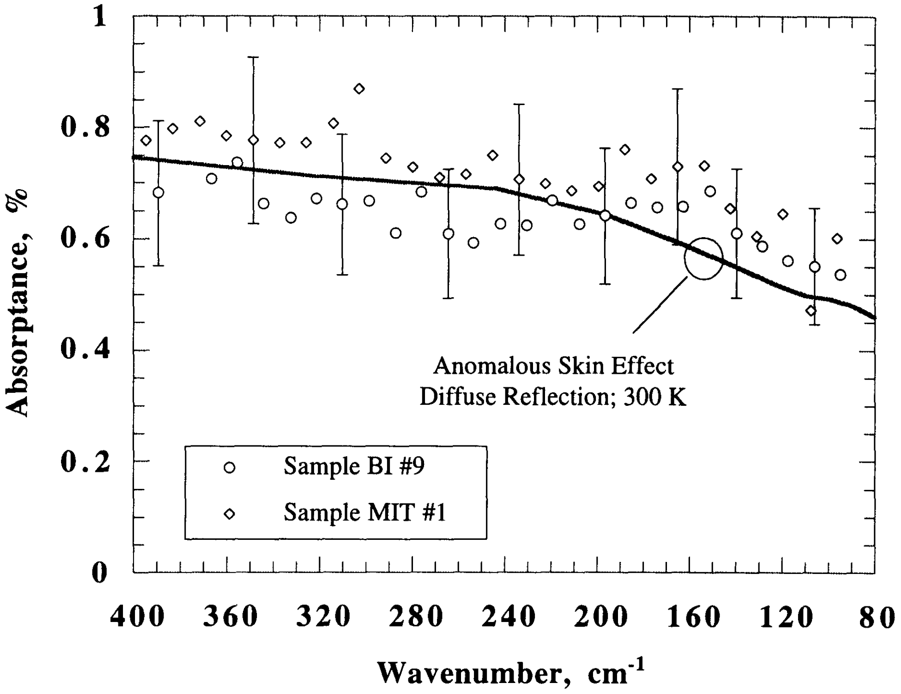

Figure 5.6 Absorptance of gold at 300 K for samples BI#9 and MIT#1 with the ASE model diffuse reflection prediction.

Figure 5.7 shows the absorptance of sample BI#9 with the three predictive models considered in this work: the Drude model, and the anomalous skin effect theory for diffuse reflection (p=0) and specular reflection (p=1). Model parameters are taken from Table 5.1. Note that at room temperature, the specular reflection prediction yields the same value as the Drude model. The diffuse reflection anomalous skin effect model seems to better represent the data. However, given its computational simplicity and impressive agreement with the data, the Drude model is recommended as the predictive model for engineering applications at room temperature.

5.9.2 Comparison with Previous Room-Temperature Experimental Investigations

Figure 5.8 compares the room-temperature absorptance data for sample BI#9 with eight previous experimental investigations. Four of the previous experimental investigations overlap with part of the spectral range of this investigation: Gatesman et al. (1993); Toscano and Cravalho (1976); Brandli and Sievers (1971); and Bennett and Ashley (1965). These experiments are shown in Fig. 5.9 and are considered here in detail. The remainder of the experiments are mentioned briefly as they relate to the influence of deposition conditions on the resultant film radiative properties.

Gatesman et al. (1993) measured the reflectance of a gold film at 117.7 μm and 513.0 μm with a reported accuracy of ±0.1% using a high precision reflectometer and a CO_2 optically-pumped SM laser. The high accuracy was achieved by using a precision sample holder, which allowed for the precise interchange of sample and reference, and characterizing the optical properties of the silicon reference to better than ±0.03%. Their result at 117.7 μm lies slightly above the data measured here. They report the same absorptance value at 513.0 μm, which disagrees markedly with the trend of the data for sample BI#9. Their sample came from a commercial source, which might account for the increased absorptance.

Toscano and Cravalho (1976) used a multiple reflection technique to measure the absolute reflectance of gold films at 6 K, 77 K, and 300 K for the spectral range from 4 μm to 30 μm.

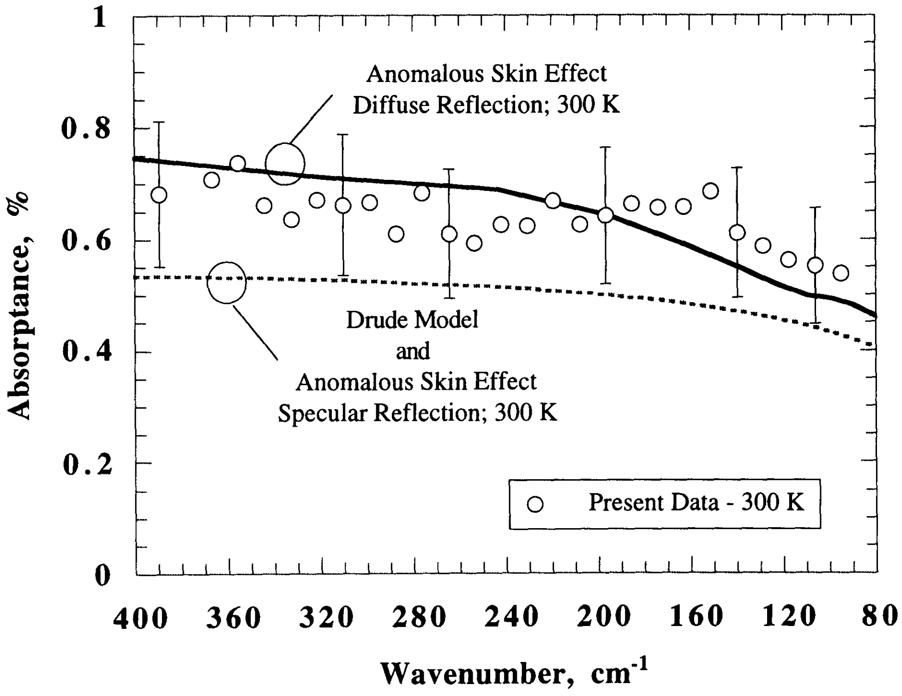

Figure 5.7 Absorptance of gold at 300 K for sample BI#9 with the Drude model and ASE model specular and diffuse reflection predictions.

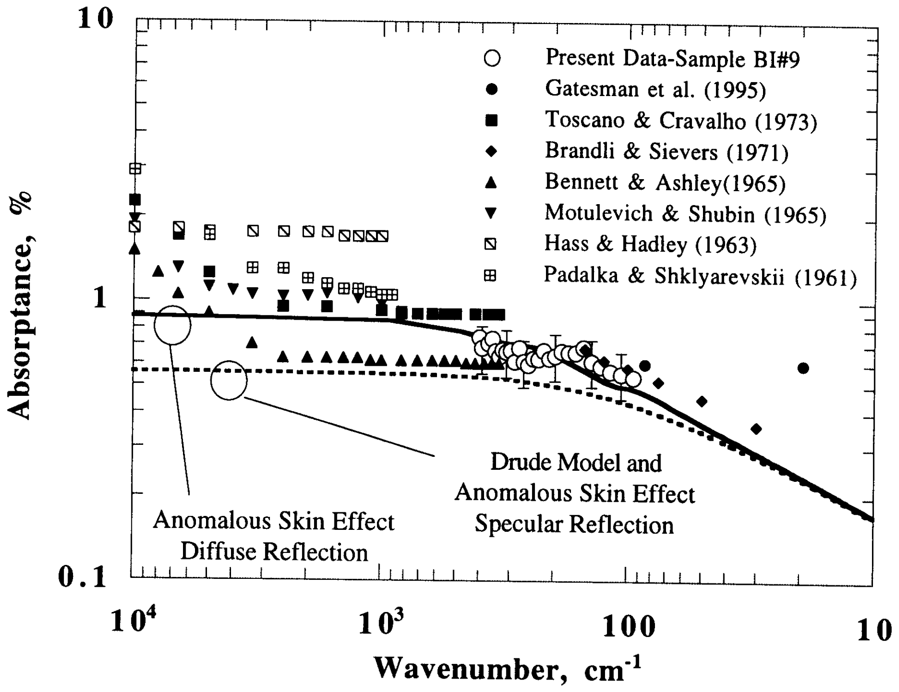

Figure 5.8 Comparison of the absorptance of gold at 300 K for sample BI#9 and previous experimental investigations.

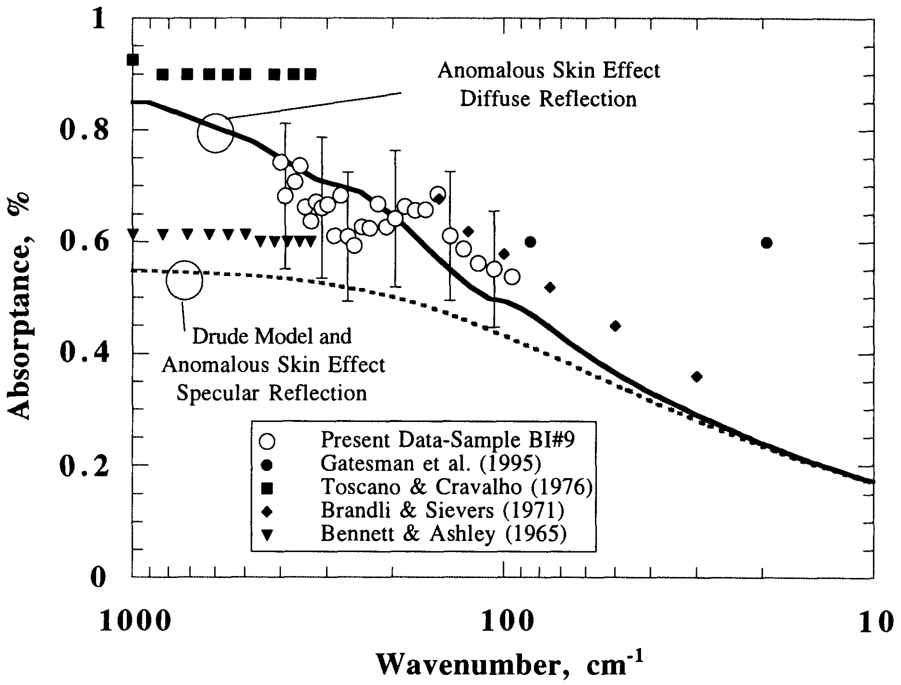

Figure 5.9 Comparison of the absorptance of gold at 300 K for sample BI#9 and previous experimental investigations (1000-10 cm^{-1}).

The films were prepared using a high-vacuum vapor deposition system, with a background pressure of 10^{-6} torr. This technique measures a reference signal by removing the sample holder from the beam path. The sample and reference signal pathlengths are different, which might cause an error in the measurement. Their data lie above the error bars for the BI#9 data. This discrepancy might be due to the pathlength difference or the higher deposition background pressure.

Brandli and Sievers (1971) measured the absolute surface resistance of 8 μm thick gold foil using a parallel-plate waveguide technique from 150 cm^{-1} to 30 cm^{-1}. Absorptance data calculated using their surface resistance data agree well with the present experiment and follow the anomalous skin effect prediction with decreasing frequency.

Bennett and Ashley (1965) measured the near-normal reflectance of a gold film with an accuracy of ±0.1% using an absolute reflection technique developed by Bennett and Koehler (1960). The film was prepared in an ultrahigh vacuum of 10^{-9} torr on a substrate with an rms roughness of 3-7 Å. The gold film had a similar rms roughness. The data agree well with the anomalous skin effect with specular reflection at the metal surface, which gives the same result as the Drude model at room temperature. Bergman (1970) prepared gold films under similar ultrahigh vacuum conditions with varying film surface roughness. He observed a decrease in absorptance at 4 μm for decreasing rms roughness.

The deposition background pressure can account for the minor differences observed in the data presented in Figs. 5.8 and 5.9. The data of Bennett and Ashley (1965), measured for films deposited with a background pressure of 10^{-9} torr yielded the lowest absorptance. The film labeled BI#9 from the present work was deposited with a background pressure of 10^{-7} torr and has a slightly larger absorptance. The films of Toscano and Cravalho (1976) and Motulevich and Shubin (1965) were deposited at 10^{-6} torr and yielded similar absorptance values, which are slightly higher than the data presented here. The films of Hass and Hadley (1963) and Padalka and

Shklyarevskii (1961) were deposited at approximately 10^{-5} torr and yielded the highest absorptance values.

5.10 Liquid-Helium Temperature Experimental Results

5.10.1 Experimental Data

The 6 K reflectance of the silicon-on-gold reflection Fabry-Pérot etalon stack containing sample BI#9 is presented in Fig. 5.10 for the spectral range from 400 cm^{-1} to 100 cm^{-1}. The sample and reference signals are collected for approximately 1.3 hrs., for 4000 scans at a scan rate of 100 kHz. The low-temperature reflectance is compared with the room-temperature reflectance for this sample in Fig. 5.11. The ratio of the reflectance minima to maxima decreases with decreasing temperature, indicting that the absorptance of the film is decreasing.

Figure 5.10 clearly shows a very large absorption band at ~315 cm^{-1}. This is unexpected as the absorption of a metal film is expected to decrease smoothly with decreasing frequency. This feature is a result of the experimental arrangement used in this measurement. For low-temperature experiments, the cryostat is typically evacuated for approximately 24 hrs. using a pumping system consisting of a liquid-nitrogen cold trap, an 80 l/sec turbomolecular pump, and a roughing pump. More details are provided in Chapter 3. The liquid nitrogen cold trap is placed between the cryostat and the turbomolecular pump. When a pressure of approximately 10^{-5} torr is reached, the cryostat valve is closed and the vacuum system is removed before beginning the low-temperature experiment. The cryostat vacuum level by itself was insufficient to collect a result at temperatures above ~40 K. In the investigation presented here, the pumping system operated during the low-temperature experiment in an unsuccessful attempt to collect a result at 100 K by continuously pumping on the system. At liquid-helium temperatures, over the 1.3 hr. experiment, a substance, possibly O_2 (Van Atta, 1965), diffused through the open pumping system onto the 6 K sample. This obscures the measurement at the 315 cm^{-1} resonance and the resonances on either side of this

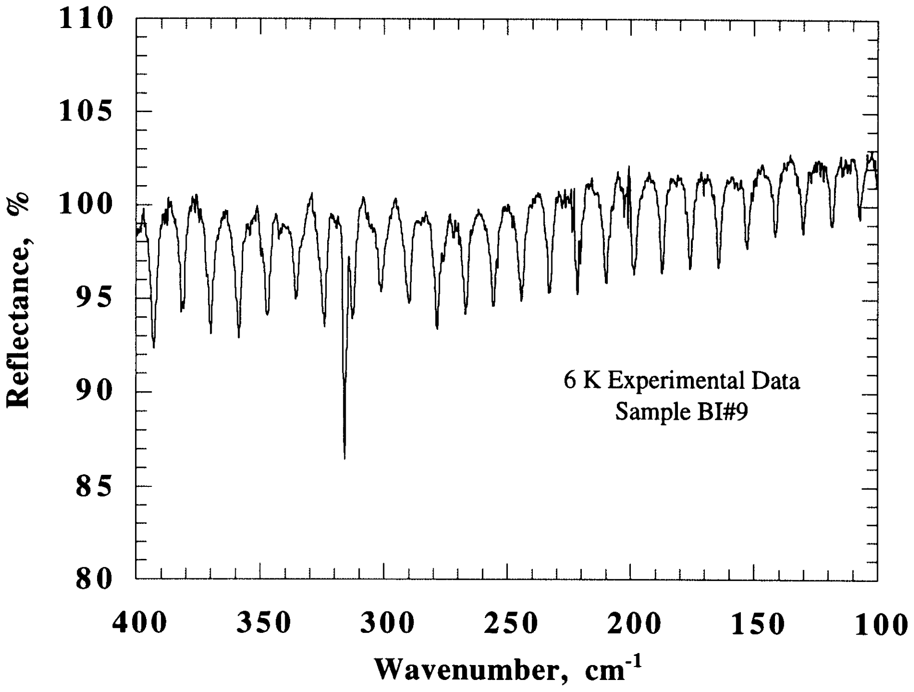

Figure 5.10 Reflectance of silicon-on-gold reflection Fabry-Pérot etalon at 6 K for sample BI#9.

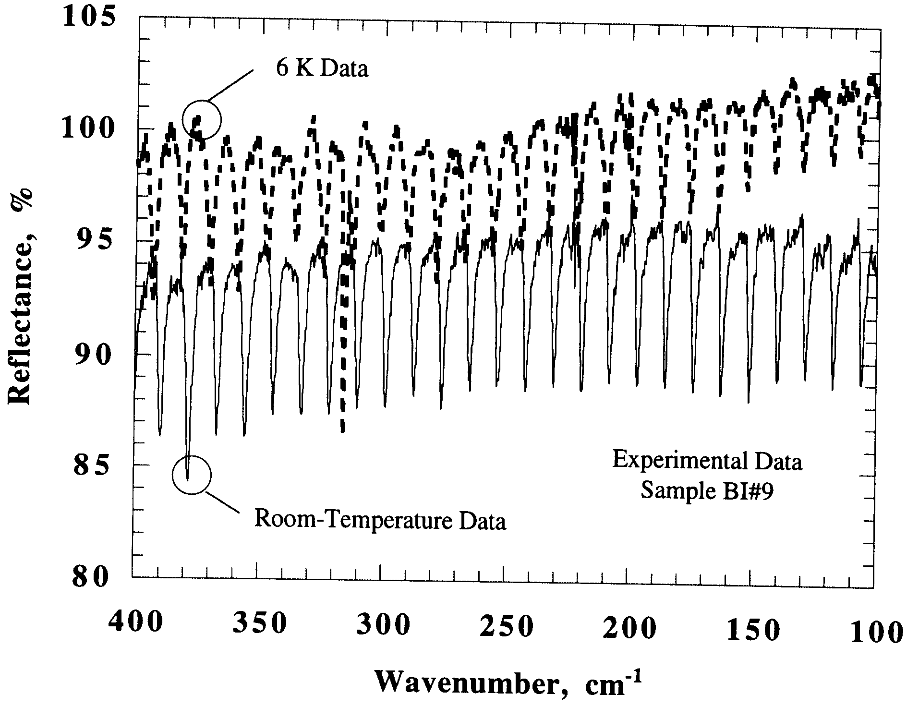

Figure 5.11 Reflectance of silicon-on-gold reflection Fabry-Pérot etalon at room-temperature and 6 K for sample BI#9.

frequency. These resonances were not considered in the analysis of the film absorptance. Resonance data outside this range are unaffected.

Figure 5.12 shows the 6 K- and room-temperature absorptance of the film with a prediction made using the anomalous skin effect with diffuse electron reflections, which provides the best agreement with the data. The data converge at the high-frequency limit of the experiment. The results differ increasingly with decreasing frequency as the mean free path of the low-temperature electrons increases with respect to the skin depth.

5.10.2 Comparison with Previous Liquid-Helium Temperature Experimental Investigations

Figure 5.13 shows all of the existing liquid-helium temperature experimental absorptance data for gold with predictions made using the Drude and the anomalous skin effect models with diffuse and specular electron scattering. The technique of Toscano and Cravalho (1976) is described in the previous section. Weaver (1981) employed a calorimetric technique to measure the near-normal absorptance of gold films. For the first time, experimental data is available for the far-infrared in the spectral range where the absorptance predicted by the anomalous skin effect begins to decrease.

From Fig. 5.13, it is clear that the Drude model and the anomalous skin effect with specular electron reflections do not describe the experimental data. Weaver's data and the data for sample BI#9 lie above the anomalous skin effect with diffuse electron reflections. This is expected as the anomalous skin effect prediction does not account for electron-phonon bulk absorption processes. A theoretical model is required which accounts for these process in the far-infrared spectral range. Toscano and Cravalho's (1976) results lie below the prediction. The discrepancy is not understood, but the difference might be within the error limits of the measurement technique, which were not reported.

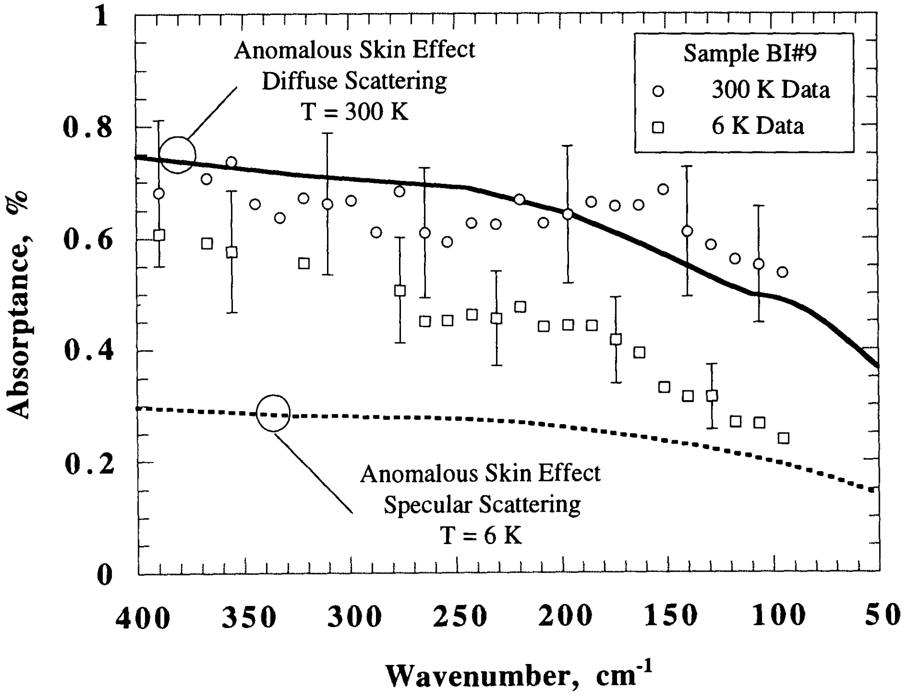

Figure 5.12 Absorptance of gold at 300 K and 6 K for sample BI#9 with ASE model diffuse reflection prediction.

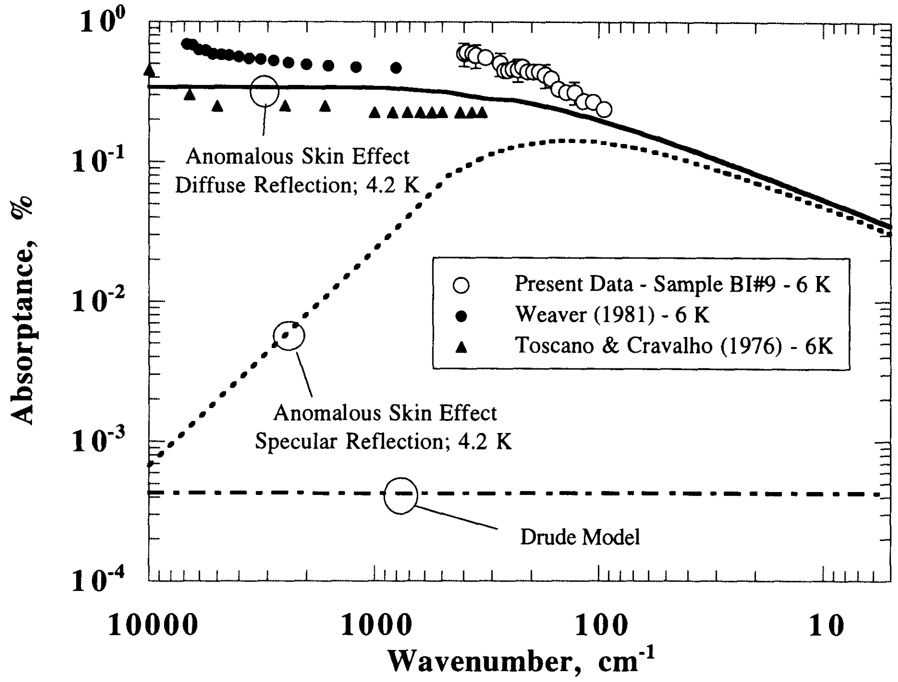

Figure 5.13 Comparison between the absorptance of gold at 4.2 K for sample BI#9 and the existing experimental data with the ASE and Drude model predictions.

5.11 Conclusions

The anomalous skin effect with diffuse electron scattering provides the most accurate prediction of the radiative properties of gold at room temperature and liquid-helium temperature. At room temperature, the discrepancy between the experimental data and the Drude model prediction is small. Given the relative simplicity of this model, it is recommended for room-temperature predictions. The Drude model is not appropriate for predicting liquid-helium temperature radiative properties. The diffuse reflection anomalous skin effect prediction agrees closely with the radiative property measurements across infrared spectral range.

CHAPTER 6

INFRARED RADIATIVE PROPERTIES OF $YBa_2Cu_3O_7$

6.1 Introduction

Since the discovery of copper oxide superconductors by Bednortz and Müller (1986), there have been an enormous number of experimental investigations applying infrared spectroscopy to study this new class of materials. Infrared spectroscopy was used successfully with low-temperature superconductors such as lead and tin to identify the superconducting energy gap predicted by the BCS theory (Tinkham, 1970). Conclusive evidence regarding the existence of an energy gap or gaps has been elusive for high-temperature superconductors. It has been suggested that the strong mid-infrared band for clean high-temperature superconductors like $YBa_2Cu_3O_7$ shields any gap from identification by infrared spectroscopy (Kamaras, 1990). At this point, there is little consensus on the correct theory for describing the phenomenon of superconductivity in copper oxide superconductors (Norman, 1993).

Many other experimental methods have applied to these materials in an effort to describe the nature of the superconductivity and to identify an energy gap. Flux quantization provided proof soon after their discovery that Cooper pairs were formed in the superconducting state (Gough et al., 1987; Gammel et al., 1987). Photoemission spectroscopy has been used to unambiguously identify an energy gap for $Bi_2Sr_2CaCu_2O_8$ (Imer et al., 1989).

Recently, angle-resolved photoemission spectroscopy techniques have been developed to the extent where experiments have explored the nature of the pairing state in ***k***-space. There is growing evidence, based on experiments using this technique, that the high-T_c superconductors have a d-wave, or anisotropic s-wave gap symmetry (Shen et al., 1995), which is not explainable with the standard BCS isotropic s-wave model of superconductivity. Some magnetic penetration depth studies for $YBa_2Cu_3O_7$ show results consistent with non-s-wave superconductivity (Hardy et al., 1993). Flux quantization measurements made with 'tricrystal' Josephson junctions support d-wave symmetry as a viable explanation, but do not rule out s-wave symmetry (Kirtley and Tsuei, 1996).

The evidence for d-wave symmetry is not conclusive and some experimental results have been inconsistent with d-wave pairing (Sun et al., 1994). Additionally, exotic pairing mechanisms (Scalapino, 1995; Cox and Maple, 1995) are required to support this approach. A theory for the infrared conductivity of d-wave superconductors has been developed only recently (Quinlan et al. 1996). Agreement with experimental data is good but no better than those achieved with BCS-theory-based phonon-mediated infrared conductivity models (Genzel et al., 1993; Zhang et al., 1994). The d-wave-based theory of Quinlan et al. (1996) is computationally intensive, whereas the BCS models require only desktop computers. In light of the present controversy regarding the gap symmetry and the computational difficulties of present d-wave models, this work develops a BCS-theory-based model for the radiative properties of $YBa_2Cu_3O_7$ by comparing the model prediction to the experimental data presented here.

The infrared optical constants of $YBa_2Cu_3O_7$ are the most heavily investigated of all the high-T_c materials. Extensive reviews of the work performed on predicting and measuring the infrared optical properties of high-T_c materials, including $YBa_2Cu_3O_7$, are given by Timusk and Tanner (1989), Tanner and Timusk (1992), Renk (1992), Thomas (1991), and many others.

Experimental data are presented here for the 6 K absorptance of two $YBa_2Cu_3O_7$ samples and one result at room temperature, along with resistivity data for similar films. The resistivity data are used to provide the material dc conductivity. Predictive models are applied to the data enabling the determination of the electron number density, the superconducting energy gap frequencies, and the scattering rate.

6.2 Normal State Radiative Property Models

The interpretation of the infrared spectra of the high-temperature superconductors is controversial, even in the normal state (Tanner and Timusk, 1992). The conventional Drude dielectric function model, consisting of a linear superposition of a high-frequency dielectric constant, ε_∞, and the Drude contribution, is unable to fit the spectra.

$$\bar{\varepsilon}(\omega) = (n + \mathrm{i}\kappa)^2 = \varepsilon_\infty + \frac{\mathrm{i}\sigma(\omega)}{\omega\varepsilon_0} \tag{6.1}$$

The Drude conductivity $\sigma(\omega)$ is:

$$\sigma(\omega) = \frac{\sigma_{\mathrm{dc}}}{1 - i\omega\tau} \tag{6.2}$$

where $1/\tau$ is the electron scattering rate. The dc conductivity σ_{dc} is related to the plasma frequency and the electron number density n_{e} as,

$$\sigma_{\mathrm{dc}} = \varepsilon_0\omega_{\mathrm{p}}^2\tau = \frac{n_{\mathrm{e}}e^2\tau}{m_{\mathrm{e}}} \tag{6.3}$$

where e is the electron charge and m_{e} is the electron effective mass.

To improve upon the conventional Drude model, several models have been proposed. The most common models are the one-component picture, which is an extension of the Drude model where the effective mass and scattering rate are frequency-dependent (Schlesinger et al., 1990), and the two-component picture, where a phenomenological mid-infrared band is added to the Drude term (Tanner et al., 1992). The mid-infrared band models a set of bound carriers, independent of the free carriers. Other models include polarons (large, small, or mixed), bipolarons, transitions involving localized states, and strong correlation models, such as the t-J model (Ruvalds, 1996). Recently, Lobo et al. (1995) proposed an extension of the Drude model which allows for different scattering rates for the longitudinal optical (LO) and transverse optical TO scattering rate. This model is especially appealing because it has been applied successfully to many superconducting and non-superconducting oxides. However, it requires as many adjustable parameters as older models, so its benefits are still unclear at present.

6.2.1 General Two-Component Dielectric Function Model

In this work, the two-component model is employed for the normal and superconducting states. A general expression for the dielectric function model, which is used here to describe both the normal and superconducting states, has the form of a linear superposition of terms (Timusk and Tanner, 1989),

$$\bar{\varepsilon}(\omega) = (\mathrm{n} + \mathrm{i}\kappa)^2 = \varepsilon_\infty + \sum_{\text{phonons}} \frac{\mathrm{S_j}\omega_\mathrm{j}^2}{\omega_\mathrm{j}^2 - \omega^2 - \mathrm{i}\omega\gamma_\mathrm{j}} + \frac{\mathrm{S_e}\omega_\mathrm{e}^2}{\omega_\mathrm{e}^2 - \omega^2 - \mathrm{i}\omega\gamma_\mathrm{e}} + \frac{\mathrm{i}\sigma(\omega)}{\omega\varepsilon_0} \tag{6.4}$$

where ε is the high-frequency dielectric constant. The second term is the infrared-active phonon contribution, which is described by the Lorentz damped oscillator model (Brewster, 1992). The model parameters are the strength S_j, the center frequency ω_j, and the damping coefficient γ_j for each phonon *j* present in the frequency range considered by the dielectric function model. The third term is a midinfrared absorption band term, considered using the Lorentz model, which accounts for interband electronic transitions (Timusk and Tanner, 1989). It has a strength S_e, a center frequency ω_e, a plasma frequency ω_{pe},= $S_e\omega_e^2$ and a damping coefficient γ_e. The midinfrared absorption band plasma frequency, ω_{pe}, corresponds to the Lorentz strength term, which depends upon the transition probability and the electron number density. The free-carrier contribution to the dielectric function is represented in the final term, where ε_0 is the electrical permittivity of free space and $\sigma(\omega)$ is the free-carrier conductivity.

This chapter presents experimental data for the *ab*-plane of fully oxygenated $YBa_2Cu_3O_7$. The *ab*-plane infrared-active phonons are effectively screened by the free-carrier contribution (Renk, 1992) in this material. Thus, the second term in Eq. (6.4) is negligible and not included in this analysis. Along the *c*-axis, the free carrier number density is much lower and infrared phonons are clearly present in experimental radiative property data. Chapter 7 presents a model for the *c*-axis dielectric function which includes five strong infrared phonon contributions.

The origin of the midinfrared absorption band in $YBa_2Cu_3O_7$ is controversial (Tanner and Timusk, 1992). The features of the band are not clearly seen in fully oxygenated $YBa_2Cu_3O_7$. However, for oxygen-reduced samples, where free-carrier screening is reduced, the mid-infrared band is clearly present in reflectance measurements (Bauer, 1990). Proponents of the one-component model for the infrared conductivity argue that the whole infrared spectral range may be represented without the mid-infrared band using a frequency-dependent scattering rate and effective electron mass (Quinlan et al., 1996; Lobo et al., 1996). Bozovic (1990) contends that the mid-infrared band is not an intrinsic material property, but is caused by structural or compositional disorder.

The parameters of the mid-infrared band used by most authors (Zhang et al., 1994; Bauer, 1990) are in reasonable agreement with experimental data for the mid-infrared plasma frequency. The plasma frequency may be evaluated using the sum rule for the optical conductivity (Bozovic et al., 1992). The screened plasma frequency determined from the data of Bozovic (1990) is in good agreement with the value of Zhang et al. (1994). The plasma frequency obtained from electron-energy-loss spectroscopy (EELS) studies (Tarrio and Schnatterly, 1988) agrees well with these values. This agreement further strengthens the appropriateness of the two-component model used here.

6.2.2 Room-Temperature Dielectric Function Model Parameters

For the room-temperature data presented here, the free-carrier contribution to the dielectric function, the final term in Eq. (6.4), is represented with the Drude model, Eq. (6.2). The model requires values for the high-frequency dielectric constant, ε, the mid-infrared band Lorentz parameters, S_e, ω_e, γ_e, the free-carrier dc conductivity σ_{dc}, and the scattering rate, $1/\tau$.

6.3 Superconducting State Dielectric Function Models

6.3.1 Model Basics

In the superconducting state, the dielectric function model has the same form as in the normal state, i.e., Eq. (6.4). Only the free-carrier conductivity contribution to the dielectric function model changes. The mid-infrared band is only weakly affected by the onset of superconductivity (Tanner et al., 1992).

Zhang et al. (1994) proposed the free-carrier conductivity model used in this work. It consists of two components: a BCS free-electron conductivity σ_{ss} for electrons whose behavior is described by the BCS microscopic theory of superconductivity (Bardeen et al., 1957) and a residual normal-state free-electron conductivity σ_{nr} for electrons which remain in the normal state below T_c. The contribution of each component to the conductivity is given by a weighted sum

$$\sigma(\omega,T) = (1 - \mathrm{f}_{\mathrm{nr}})\sigma_{\mathrm{ss}}(\omega,T) + \mathrm{f}_{\mathrm{nr}}\sigma_{\mathrm{nr}}(\omega) \tag{6.5}$$

where f_{nr} is the temperature-independent fraction of residual normal-state electrons. The Drude model is used to account for the normal-state free-electron conductivity σ_{nr}.

Kobayashi and Imai (1991) first suggested the use of a temperature-independent fraction of normal-state electrons, modeled using the Drude theory to account for the anomalously large absorption observed in the far-infrared for $YBa_2Cu_3O_7$, even at temperatures approaching 0 K (Renk et al., 1991; Genzel et al., 1993; Miller et al, 1993). The BCS theory predicts that at low temperatures, for frequencies smaller than the gap frequency, there are no absorption mechanisms and so electromagnetic radiation should not be absorbed (Mattis and Bareen, 1958). In $YBa_2Cu_3O_7$, it appears that a fraction of the free electrons do not condense into Cooper pairs, regardless of the temperature. It is not known if this non-condensing fraction is an intrinsic property of the material. Renk et al. (1991) suggested the cause is intergrain or impurity-induced absorption in defect regions of the material. Zhang et al. (1994) and Pham et al. (1990) suggest the absorption was caused by oxygen deficiency within a thin layer on the material surface. This is supported by experimental observations by Genzel et al. (1993), who observed an increase in the infrared absorptance of films only a few days old. The absorptance is easily reduced by heating up the films in an oxygen environment, suggesting that oxygen is lost from the Cu-O chains through staggering faults on their film surfaces. If the absorption is non-intrinsic and can be reduced by processing improvement, significant improvements in the performance of $YBa_2Cu_3O_7$-based radiation shielding and Fabry-Pérot resonators can be achieved, as described in Chapters 7 and 8.

6.3.2 BCS-Electron Conductivity

The BCS free-electron conductivity for $YBa_2Cu_3O_7$ is predicted from expressions given by Zimmermann et al. (1991), which were derived within the framework of the BCS superconductivity theory (Bardeen et al., 1957). By modeling the response of electrons to a space- and time-dependent electric field, Zimmermann et al. (1991) obtained the free carrier motion for a weakly coupled superconductor with arbitrary purity, i.e., a solution which is valid for any value of the electron mean free path.

Following the approach taken by Genzel et al. (1993), the BCS free-electron conductivity is modeled as the summation of a number of discrete, weighted energy gaps,

$$\sigma_{ss}(\omega,T)=\sum_{k} f_{gk}\sigma_{ss,k}(\omega,T) \tag{6.6}$$

$$\sum_{k} f_{gk}=1 \tag{6.7}$$

Zimmermann et al. (1991) gives the functional dependence of the complex conductivity for each energy gap as:

$$\sigma_{\mathrm{ss,k}}(\omega,T)=\sigma_{\mathrm{dc}}\,\mathrm{F}\left(\mathrm{x}=\omega\mathrm{h}/4\pi\Delta_{\mathrm{k}},\mathrm{Y}=\mathrm{h}/4\pi\tau\Delta_{\mathrm{k}},T/T_{\mathrm{c}}\right) \tag{6.8}$$

where σ_{dc} is the dc electrical conductivity, and F is a function of the normalized frequency, x, the ratio of sample to transition temperature, T/T_{c}, and the normalized electron scattering rate, $Y = h/(4\pi\tau\Delta_{\mathrm{k}})$, where h is Planck's constant, $1/\tau$ is the electron scattering rate, and Δ_{k} is the k^{th} superconducting energy gap.

The purity of a superconductor is measured by the ratio of the superconductor coherence length, ξ, the lengthscale over which electrons are correlated in the superconducting state, to the mean free path of the electrons (Orlando and Delin, 1991). The normalized scattering rate, Y, is proportional to the purity. For $Y >> 1$, the superconductor is in the impure limit and the theory of Zimmermann et al. (1991) gives the same results as the theory of Mattis and Bardeen (1958), which is valid for impure isotropic superconductors. For a pure superconductor such as $YBa_2Cu_3O_7$ for which $Y < 1$, the Mattis-Bardeen theory yields a large error (Flik et al., 1992).

It should be noted that while the Zimmermann theory accounts for arbitrary purity, its validity is strictly limited to weakly coupled (BCS) superconductors. The coupling strength between electrons and phonons in a superconductor is defined in terms of the energy gap parameter, $A = 2\Delta_0/k_{\mathrm{B}}T_{\mathrm{c}}$ (Burns, 1990) where k_{B} is the Boltzmann constant and Δ_0 is the superconductor energy gap at 0 K. For a BCS weakly coupled superconductor, A is approximately 3.53. Values of A in excess of 3.53 are indicative of strong electron-phonon coupling. Another requirement for the applicability of the Zimmermann model is that the superconducting coherence length, ξ, must be smaller than both the wavelength of incident radiation, λ, and the magnetic penetration depth. Zhang et al. (1992) showed that these conditions are satisfied for the *ab*-plane of $YBa_2Cu_3O_7$ for $\lambda > 1$ μm and temperatures not too close to T_{c}.

6.3.3 Superconducting State Dielectric Function Model Parameters

For the 6 K data absorptance presented here, the dielectric function model, Eq. (6.4), requires values for the high-frequency dielectric constant, ε and the mid-infrared band Lorentz parameters, S_e, ω_e, γ_e,. In addition, to model the free-carrier conductivity component requires the residual normal-state electron fraction f_{nr}; the dc conductivity σ_{dc}; the scattering rate, $1/\tau$; the energy gap distribution ν_{gk} and relative weights f_{gk}.

6.4 Previous High-Accuracy Radiative Property Investigations

Many investigations of the infrared radiative properties of $YBa_2Cu_3O_7$ have been performed. The majority employed standard FT-IR reflectance measurement techniques, with experimental accuracies of ~±1%. The reflectance of $YBa_2Cu_3O_7$ for wavelengths longer than ~25 μm exceeds 99%, so information regarding the existence of a far-infrared energy gap or the actual absorptance for this spectral range is unavailable from these experiments.

Several experimental efforts have been made to characterize the radiative properties of $YBa_2Cu_3O_7$ with high accuracy. Several groups have measured the transmittance of thin films (de Vaulchier et al., 1995; Hadni et al., 1995; Cunsolo et al. 1993). These results are not presented here because a direct comparison with the present data is not possible. Transmittance measurements must account for the radiative properties of the substrates, which can interfere with the interpretation of the film radiative properties. Additionally, Zhang et al. (1992) showed a considerable size effect on the radiative properties of $YBa_2Cu_3O_7$ thin films. The radiative properties of very thin $YBa_2Cu_3O_7$ films may disagree significantly with single-crystal samples or thicker films.

Given the difficulties with transmittance measurements, only results involving absorptance and reflectance measurements will be presented here. Three groups have presented high-accuracy absorptance data for $YBa_2Cu_3O_7$: 1) Pham et al. (1990; 1991); 2) Miller et al. (1993); and 3) Genzel et al. (1993). The results of these efforts are shown in Fig. 6.1. Note that there is no rapid

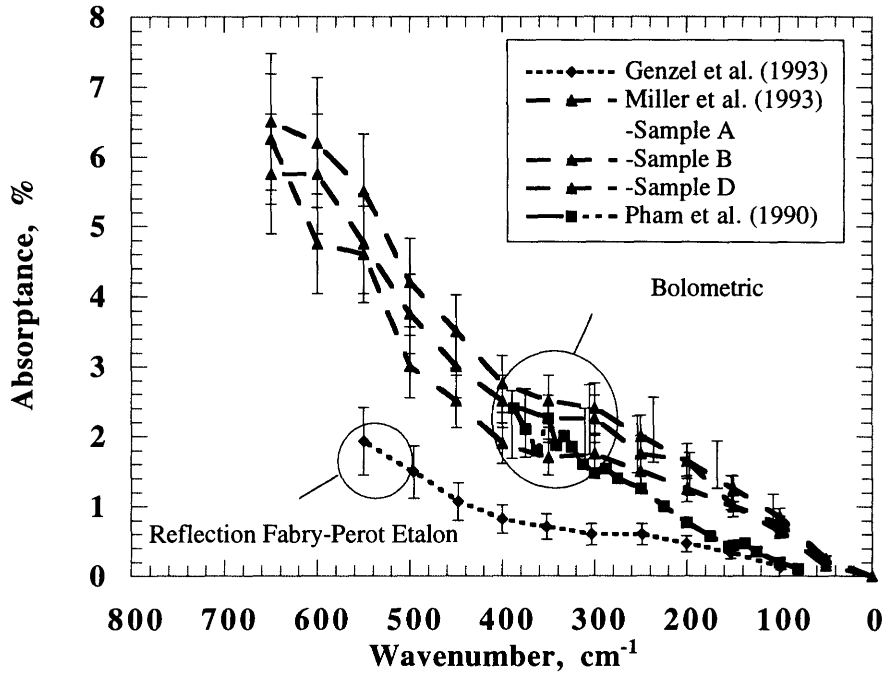

Figure 6.1 Previous high-accuracy absorptance measurements for $YBa_2Cu_3O_7$.

decrease in the absorptance for any of the data across the spectral range, indicating that there are no large single energy gaps for these materials.

Pham et al. (1990; 1991) used a bolometric technique to measure the absorptance at 2 K of twinned (1990) and detwinned (1991) $YBa_2Cu_3O_7$ single crystals from 400 to 80 cm^{-1}. Both samples had a T_c of 93 K. Figure 6.1 displays the results for the twinned sample, since the films investigated here are also twinned. The data was measured by directing far-infrared radiation from a step-scan FT-IR into a specially designed bolometer, where two elements received an equal amount of radiation. One element was fabricated from $YBa_2Cu_3O_7$, the other was a silicon reference detector. The relative absorptance was obtained by taking the ratio of the signal from both elements. By calibrating both detectors, the absolute absorptance was obtained. Pham et al. (1990) reported an error of ~±40% at the high-frequency limit and ~±100% at the low-frequency limit. They report possible evidence of a gap at ~230 cm^{-1}.

Miller et al. (1993) used the same technique as Pham et al. (1993) to measure the absorptance of several $YBa_2Cu_3O_7$ films on substrates of $SrTiO_3$, $LaAlO_3$, and MgO with critical temperatures between 85 K and 92 K. The measurement temperature was 4 K and the spectral range was 700 to 25 cm^{-1}. The reported accuracy was ±15%. The absorptance of all films were qualitatively similar, increasing smoothly with frequency. The sample with the highest T_c exhibited a slightly lower absorptance. They could not identify a gap feature in the data.

Genzel et al. (1993) used the reflection Fabry-Pérot etalon technique described in this work to measure the absorptance of a $YBa_2Cu_3O_7$ film at 10 K and 100 K from 650 to 50 cm^{-1}. The film was prepared by laser ablation and had a T_c of 90 K. The absorptance is notably smaller than the other experiments and rises much more slowly with increasing frequency. The lower absorptance was possibly due to a much higher quality sample, or to careful oxygen regeneration of the film as described above. They contend that these data could be explained only with a predictive model which uses a nearly continuous gap distribution from 215 to 70 cm^{-1} and an isolated gap at 330 cm^{-1}.

6.5 $YBa_2Cu_3O_7$ Sample Preparation

Experimental data from two sets of $YBa_2Cu_3O_7$ samples are presented here. All of the samples were prepared at the Max-Planck-Institut für Festkörperforschung in Stuttgart, Germany. The substrate were $SrTiO_3$, 10 x 10 mm, prepared with a flatness deviation of approximately ±0.2 μm. Before deposition, the flatness of the substrate was measured using a non-contact laser interferometric technique to ensure the flatness specification was met.

The films were deposited using an off-axis magnetron sputtering system described in detail by Wagner and Habermeier (1994). The system makes use of an adaptively calibrated pyrometer to maintain a constant deposition temperature during film growth. A constant deposition temperature is critical for the fabrication of high-quality films. The adaptively calibrated pyrometer was first applied to high-T_c film growth by Flik et al. (1992).

One set of films, labeled OA7#1 and OA7#2, are used for the low temperature reflection Fabry-Pérot etalon measurements. These two films were prepared in the same deposition run and had a film thickness was ~3000 Å. The surface roughness of a similar film was measured using a profilometer. The rms roughness was determined to be 319 Å ±25 Å. A test film fabricated in the same run was determined to have a T_c of 86 K.

Another film, labeled OA#6, is used for a single-reflection room-temperature reflectance measurement. The film thickness was 5800 Å. The surface roughness is unknown, but the film is specular and the roughness is not critical for this measurement.

6.6 Hypothetical dc Electrical Resistivity

The dc electrical resistivity of two sample similar to samples OA7#1 and OA7#2 were measured at the Max-Planck-Institut für Festkörperforschung using the standard four-lead van der Pauw method. Measurements were made at 273 K and 100 K. The accuracy of the measurement technique is ±10%. The data lie with the ±10% error bound.

The data for both samples is shown in Fig. 6.2 along with a theoretical prediction for a hypothetical dc electrical resistivity for temperature less than T_c = 86 K. The technique for determining a hypothetical dc electrical resistivity for $YBa_2Cu_3O_7$ films was developed by Goodson and Flik (1993). It was used by Zhang et al. (1992) as part of the development of a dielectric function model for comparison with experimental reflectance measurements.

The technique is summarized here. Matthiessen's rule (Ziman, 1963) is used to extrapolate the normal-state dc resistivity to temperatures below T_c. Two scattering mechanisms are considered: defect scattering, which is temperature independent, and electron-phonon scattering, which is modeled using the Bloch theory (Ziman, 1963). The Bloch theory is a relatively simple theory which does not account for scattering mechanisms such as electron-electron scattering, etc. However, it agrees well with experimental results for metals and provides the same trend as more complex theories. Additionally, for the low-temperature data presented here, the electron-phonon contribution is negligible.

Matthiessen's rule is written as,

$$\rho(T) = \rho_s(T) + \rho_d \tag{6.9}$$

where ρ_d is the electrical resistivity due defect scattering and $\rho_s(T)$ is the electrical resistivity due to scattering on phonons. The Bloch theory gives the following expression for $\rho_s(T)$,

$$\rho_s(T) = 4\rho_\theta \left(\frac{T}{\theta}\right)^5 \int_0^{\frac{\theta}{T}} \frac{x^5 e^x}{\left(e^x - 1\right)^2} dx \tag{6.10}$$

where ρ_θ is a constant and θ is the Debye temperature. Goodson and Flik (1993) determined that θ = 470 K for $YBa_2Cu_3O_7$. As is evident from Fig. 6.2, $\rho_s(T)$, is very small for $T/\theta < 0.1$. For the low-temperature experiments presented here, $\rho(6\ K) = \rho_d$.

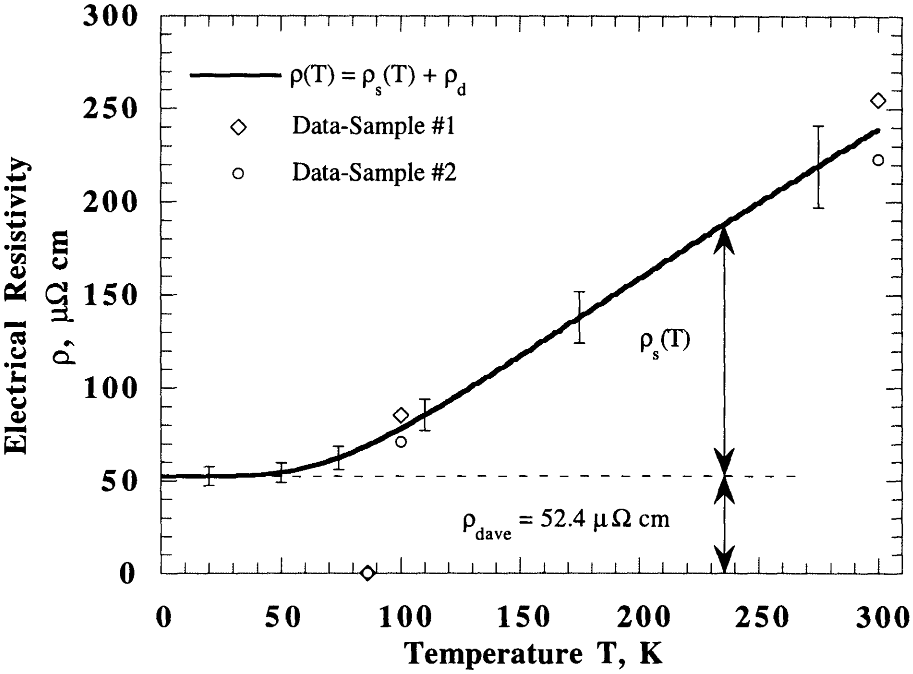

Figure 6.2 Comparison of the predicted electrical resistivity with experimental data for two $YBa_2Cu_3O_7$ samples.

The method of Goodson and Flik (1993) determines the hypothetical dc electrical resistivity by fitting Eq (6.9) to the measured resistivity data, using ρ_d and ρ_θ as adjustable parameters. The fit to the average measured resistivity data is shown in Fig. 6.2.

6.7 Room-Temperature Experimental Results

6.7.1 Experimental Data

The mid- and far-infrared reflectance of sample OA#6 are measured using the room-temperature reflectance accessory from ~1000 to 80 cm^{-1}. Results of these measurements are shown in Fig. 6.3, along with a predictive model fit, which is described in the following section.

The mid-infrared single beam data for the sample and gold reference are measured from 1000 to 400 cm^{-1} using a Glowbar source, a KBr beamsplitter, and a DTGS pyroelectric detector with a KRS-5 window. The FT-IR is evacuated and the aperture is set at 1 mm. Approximately 500 scan are collected for both measurements at a scan speed of 10 kHz and a resolution of 2 cm^{-1}.

The far-infrared single beam data are measured using a Glowbar source, a 6 μm Mylar beamsplitter, and a liquid-helium cooled bolometer from 600 to 80 cm^{-1}. Again, the FT-IR is evacuated, and the aperture is set at 1mm. Approximately 1000 scans are collected at 100 kHz, with a resolution of 1 cm^{-1}.

The mid- and far-infrared reflectance spectra overlap between 600 and 400 cm^{-1}. The data agree to better than 0.5% in this range. The overall error for these measurements is approximately ±1%, as indicated in Fig. 6.3. These data agree well with previous room-temperature reflectance measurements (Watanabe et al., 1989; Renk et al., 1989).

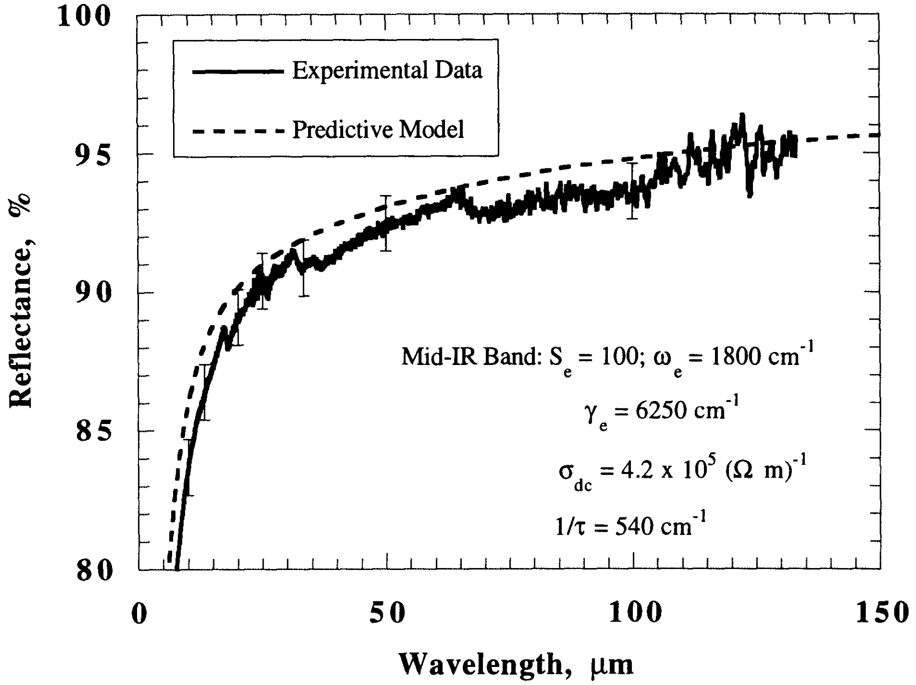

Figure 6.3 Comparison of the predictive model to the experimental data for the room-temperature infrared reflectance data for $YBa_2Cu_3O_7$.

6.7.2 Analysis of Room-Temperature Experimental Data

Equation (6.4) is used to develop a predictive model for these data. The model requires the following data: the high-frequency dielectric constant, ε; the mid-infrared band Lorentz parameters, S_e, ω_e, γ_e; the free-carrier dc conductivity σ_{dc}; and the scattering rate, $1/\tau$.

The high-frequency dielectric constant, $\varepsilon = 4$, is well-known and does not influence the far-infrared reflectance strongly (Tanner and Timusk, 1992). Following the approach of Zhang et al. (1994), the mid-infrared band center frequency is set at $\omega_e = 1800$ cm^{-1}, based on the work of Bauer (1990), and S_e and γ_e are used as adjustable parameters. These parameters have only a weak influence on the radiative properties for $\nu < 400$ cm^{-1}. The dc conductivity is taken from the arithmetic average of the experimentally measured dc electrical resistivity at 273 K: $\rho_{dc} = 239 \times 10^{-8}\ \Omega$ m, $\sigma_{dc} = 4.2 \times 10^5\ (\Omega\ \text{m})^{-1}$. Finally, the scattering rate $1/\tau$, which strongly influences the radiative properties for $\nu < 400$ cm^{-1}, is used as an adjustable parameter.

The best fit to the experimental data is given in Fig. 6.3. The mid-infrared band parameters, $S_e = 100$ and $\gamma_e = 6250$ cm^{-1} are similar to those determined by many investigators (Zhang et al., 1994; Bauer, 1990). The scattering rate determined from the fit is $1/\tau = 540$ cm^{-1}. The scattering rate is higher than that observed in very high-quality film, e.g., $1/\tau \approx 400$ cm^{-1}, but is similar to results for good films, such as the work of Zhang et al. (1992).

The electron number density may be determined using σ_{dc} and $1/\tau$ from the above model and Eq. (6.3). Rewriting Eq. (6.3) in terms of the electron number density,

$$n_e = \frac{\sigma_{dc} m_e}{e^2}\left(\frac{1}{\tau}\right) \tag{6.3}$$

The electron effective mass is set at $m_e = 4.3 \times 10^{-30}$ kg, based on the work of Fiory et al. (1990). They determined m_e and the electron number density n_e for the *ab*-plane of $YBa_2Cu_3O_7$ thin films by measuring the influence of charge density modulation on the sheet inductance and sheet resistance of the films. The sample with the lowest normal-state electrical resistivity yielded a value of $m_e = 4.3 \times 10^{-30}$ kg. They determined that the electron number density was independent of temperature, but varied between samples.

With these data, the electron number density n_e for film OA#6 is found to be $n_e = 7.1 \times 10^{27}$ m^{-3}. Given the similar deposition conditions, the same number density is applied to the films used in the low-temperature experiments, OA7#1 and OA7#2. This value is similar, but slightly lower than estimates for the highest quality films (Genzel et al., 1993). The data determined from this analysis are summarized in Table 6.1.

6.8 Low-Temperature Experimental Results

6.8.1 Experimental Data

The 6 K reflectance of the silicon-on-$YBa_2Cu_3O_7$ reflection Fabry-Pérot etalons containing samples OA7#1 and OA7#2 are shown in Figs. 6.4 and 6.5, respectively, for the spectral range from ~420 to ~80 cm^{-1}. The single beam spectra for both samples are collected for approximately 1.3 hrs., for a total of ~4000 scans collected at a scan rate of 100 kHz at a resolution of 0.25 cm^{-1}. Separate background spectra are collected for both samples.

Note that due to the difficulties in maintaining the sample and reference in the same position throughout the low-temperature experiments causes the reflectance spectra in Figs. 6.4 and 6.5 to be severely distorted. Using the method described in Chapter 2, however, meaningful absorption data are extracted from these spectra. Figure 6.6 shows the absorptance of both films at 6 K, exhibiting very good agreement across the entire spectral range. The error bars shows in Fig. 6.6 equal approximately ±20%.

Table 6.1 Parameters for room-temperature dielectric function model.

ε	ω_e (cm^{-1})	S_e	γ_e (cm^{-1})	σ_{dc} (Ω^{-1} m^{-1})	$1/\tau$ (cm^{-1})	n_e (m^{-3})
4	1800	100	6250	4.2×10^5	540	7.1×10^{27}

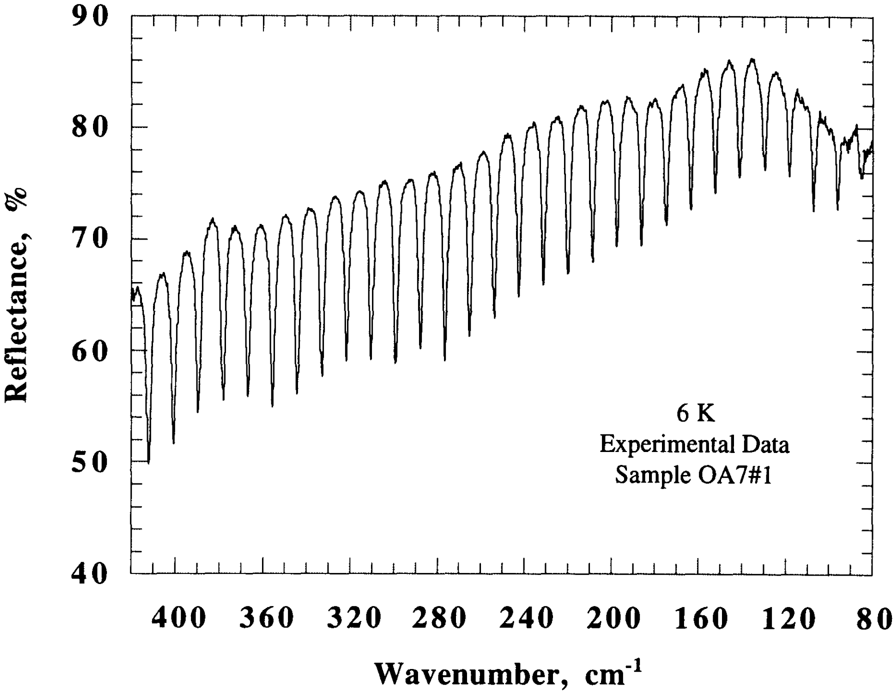

Figure 6.4 Reflectance of a $YBa_2Cu_3O_7$-on-gold reflection Fabry-Pérot etalon (sample OA7#1).

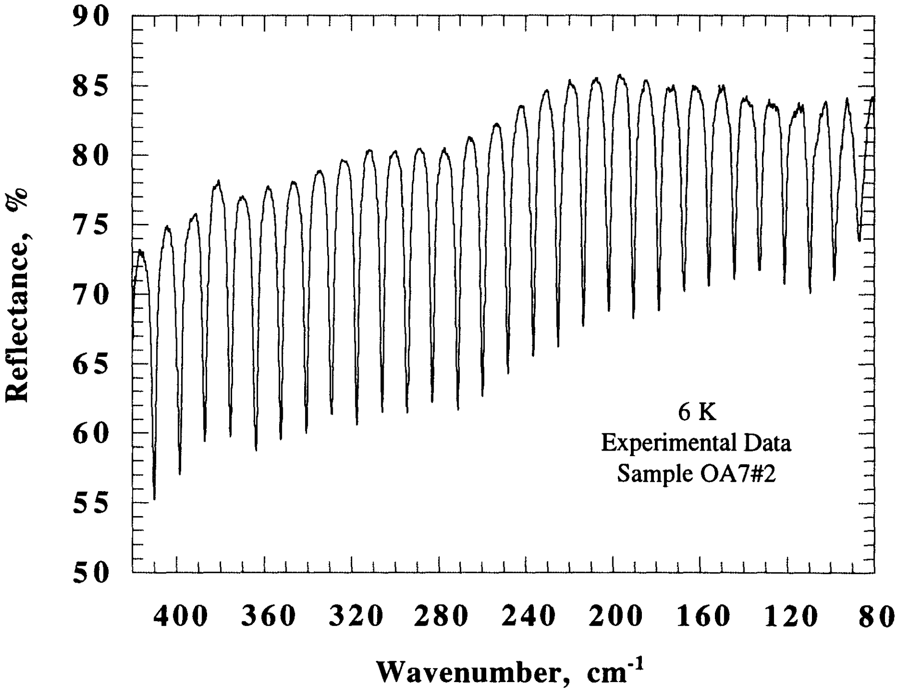

Figure 6.5 Reflectance of a $YBa_2Cu_3O_7$-on-gold reflection Fabry-Pérot etalon (sample OA7#2).

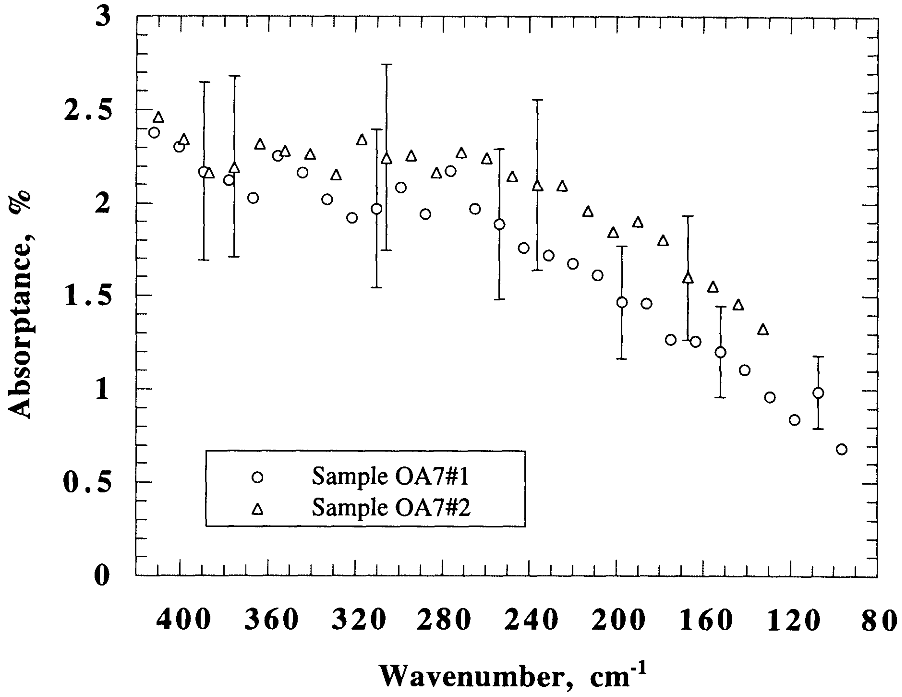

Figure 6.6 Absorptance of $YBa_2Cu_3O_7$ samples OA7#1 and OA#2 at 6 K.

6.8.2 Analysis of Liquid-Helium Temperature Experimental Data

Figure 6.7 shows the absorptance data for samples OA7#1 and OA7#2 in comparison with the existing high-accuracy absorptance data. For clarity, the data are presented again in Fig. 6.8 for a smaller spectral range and with only one of Miller et al.'s (1993) results.

The present data closely matches the data of Miller et al. (1993) for frequencies less than 250 cm^{-1}. The similarity between the present data and Miller et al. (1993) is expected, as the samples used in these experiments were of a lower quality than those investigated by Genzel et al. (1993) and Pham et al. (1990). For example, samples OA7#1 and OA7#2 have a T_c = 86 K, similar to the T_c for Miller et al.'s (1993) samples. The sample of Genzel et al. (1993) had a T_c = 90 K and Pham's single crystal samples had a T_c = 93 K.

For frequencies higher than 250 cm^{-1}, the present data exhibits a plateau consistent with the data of Genzel et al. (1993). The increased absorptance may be due to a loss of oxygen from the film surface layer, as was observed by Genzel et al. (1993). The resistivity data presented in Fig. 6.2 for films similar to the ones investigated here have an average room-temperature resistivity of $239 \times 10^{-8}\ \Omega$ m, which is higher than that observed for the best films. This suggests that the films investigated here have a larger number of defects than the best films, which may account for the larger absorptance.

6.8.3 Predictive Model for the Liquid-Helium Temperature Experimental Data

Figure 6.9 shows a predictive model for the present data developed using the general dielectric function model given by Eq. (6.4). The free-carrier conductivity is modeled using Eq. (6.5). The multiple gap model proposed by Genzel et al. (1993) for the BCS free-electron conductivity, Eqs. (6.6) and (6.7), is employed. The parameters for the model are given in Tables 6.2 and 6.3.

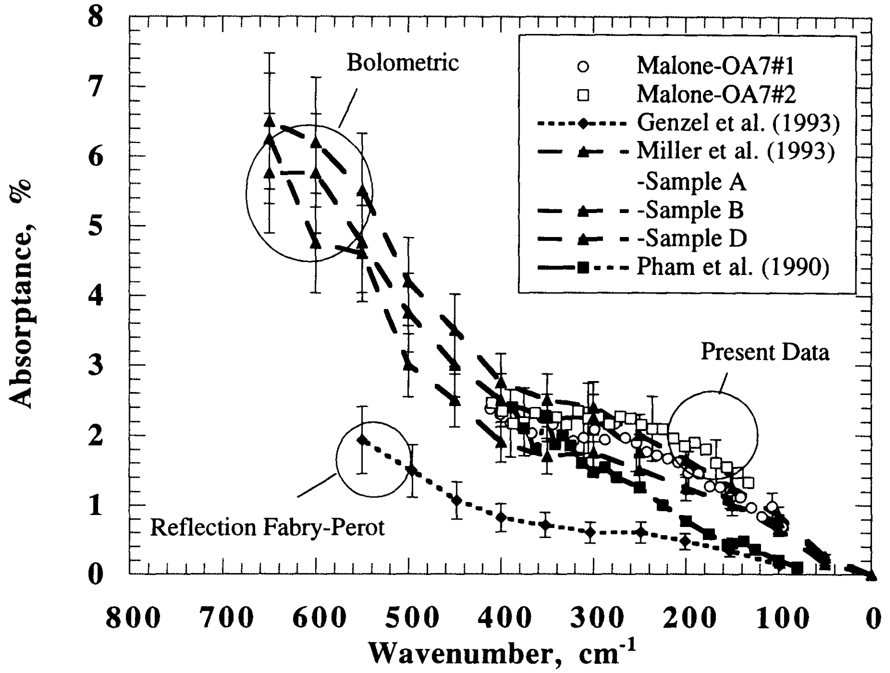

Figure 6.7 Comparison between previous results and the absorptance of $YBa_2Cu_3O_7$ samples OA7#1 and OA#2 at 6 K.

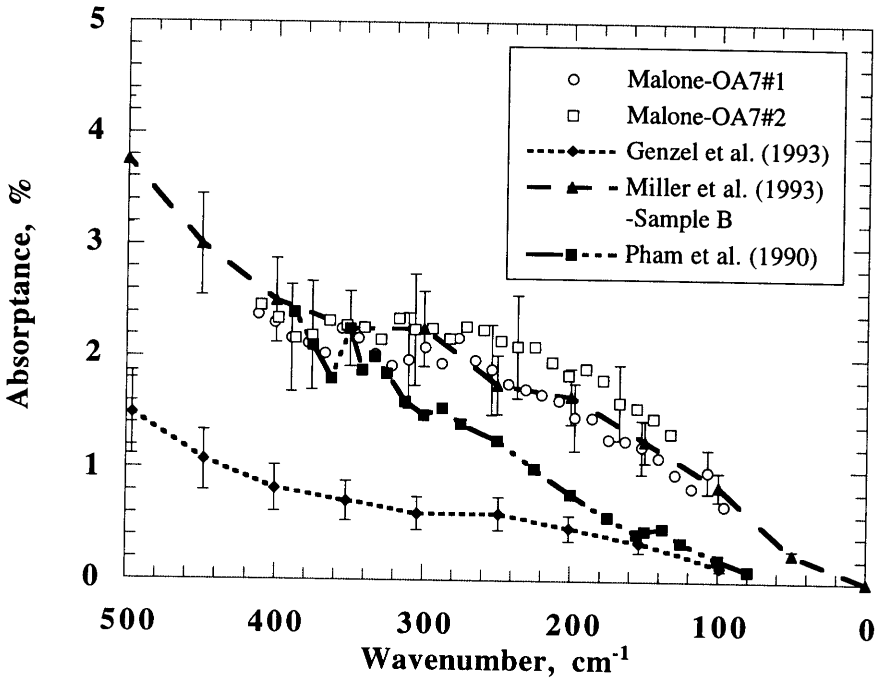

Figure 6.8 Comparison between previous results and the absorptance of $YBa_2Cu_3O_7$ samples OA7#1 and OA#2 at 6 K (reduced spectral range).

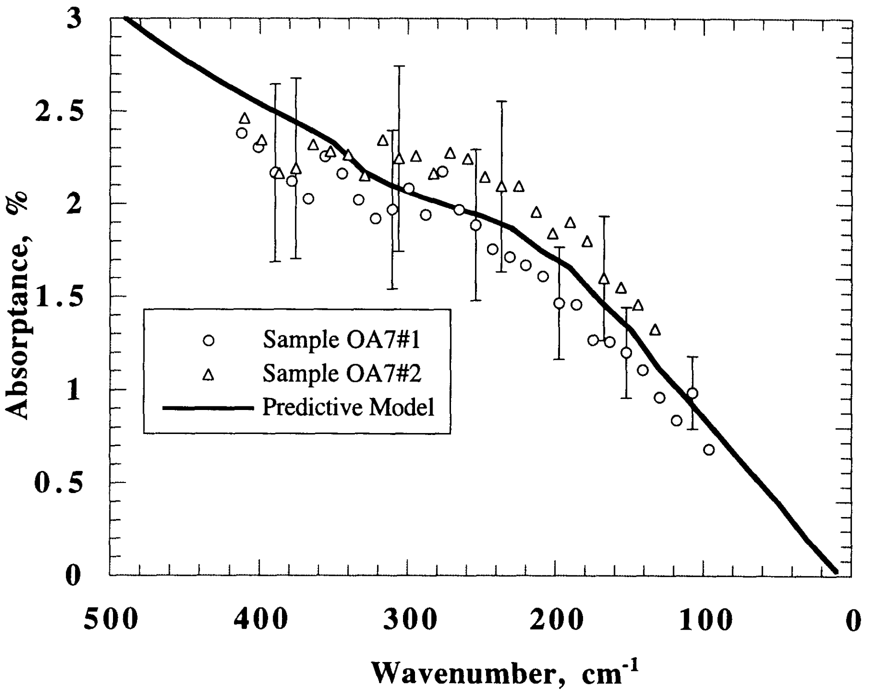

Figure 6.9 Absorptance of $YBa_2Cu_3O_7$ samples OA7#1 and OA7#2 with prediction.

Table 6.2 Parameters for dielectric function model at 6 K.

ε	ω_e (cm^{-1})	S_e	γ_e (cm^{-1})	σ_{dc} (Ω^{-1} m^{-1})	$1/\tau$ (cm^{-1})	A and Y	f_{nr} (%)
4	1800	100	6250	2.25×10^6	100	Table 6.3	40

Table 6.3 Energy gap distribution and associated non-dimensional scattering rate.

Gap #	f_{gk} (%)	v_{gk} (cm^{-1})	A_k	Y_k
1	5.6	71.9	1.20	1.39
2	5.2	82	1.37	1.22
3	4.9	91	1.52	1.10
4	5.8	100	1.67	1.00
5	6.6	112.6	1.88	0.89
6	12.4	132.2	2.21	0.76
7	12.6	143.7	2.40	0.70
8	9.8	173.2	2.90	0.58
9	9.6	176.8	2.96	0.57
10	7.5	212	3.55	0.47
11	5.4	216.4	3.62	0.46
12	14.6	331.7	5.55	0.30

The twelve energy gap frequencies and weightings used in the model are given in Table 6.3. They are taken without modification from the results of Genzel et al. (1993). The mid-infrared absorption band parameters determined for the room-temperature data are used in this model. The residual normal-state electron fraction, f_{nr}, influences the absorptivity below ~125 cm^{-1}. The best fit to the data yield f_{nr} = 40%.

The hypothetical dc conductivity at 6 K, predicted using the method of Goodson and Flik (1993), is σ_{dc} = 1.9 x 10^6 Ω m. The scattering rate determined using Eq. (6.3) with this conductivity and the electron number density of n_e = 7.1 x 10^{27} m^{-3} is $1/\tau$ = 125 cm^{-1}. With these values, the dielectric function model predicts the absorptance within the measurement error, except at the high-frequency limit, where the prediction falls slightly above the error bars. The dc conductivity σ_{dc} and the scattering rate $1/\tau$ are adjusted within the uncertainty of the hypothetical dc conductivity predictions to fit the experimental data as shown in Fig. 6.9.

The present data could not be predicted with a single gap model for any reasonable range of σ_{dc} and $1/\tau$. Zhang et al. (1994) recommended a predictive model for $YBa_2Cu_3O_7$ based on the Zimmermann theory with a single gap with a frequency of ~450 cm^{-1}. Figure 6.10 shows a prediction made using this gap frequency, along with a 12-gap model prediction for the data presented here and for the data of Genzel et al. (1993). It is evident that a nearly continuous gap distribution is required to predict these high-accuracy data.

6.9 Conclusions

Absorptance data measured at 6 K are presented for two $YBa_2Cu_3O_7$ samples for the spectral range from 420 to ~80 cm^{-1}. These data compare well with the limited set of high-accuracy absorptance data available for this material. A predictive model based on the Zimmermann theory for the BCS free-electron conductivity is developed. The experimental data cannot be predicted without employing multiple energy gaps within the model.

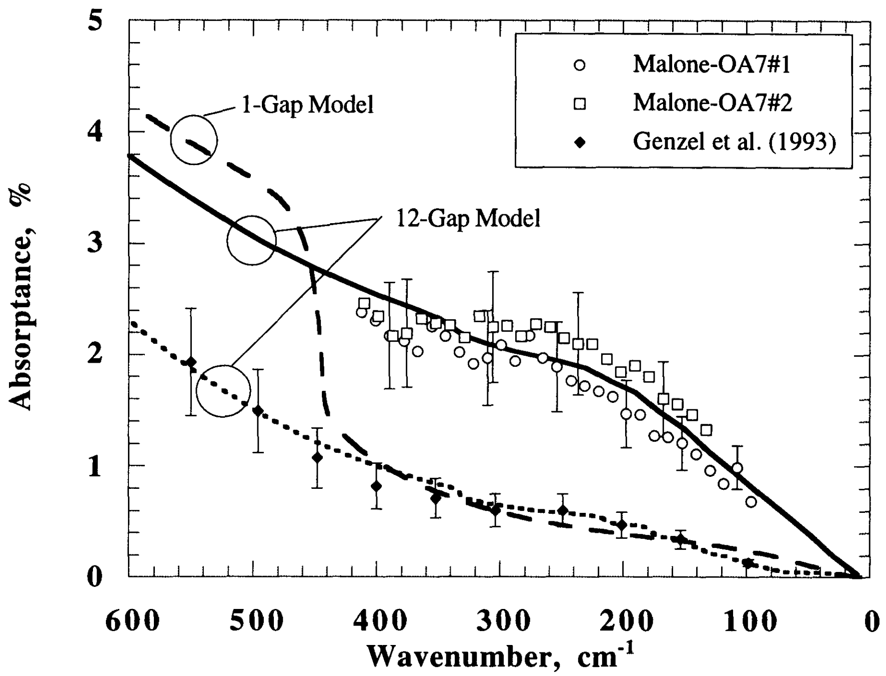

Figure 6.10 Predictive models for present data and Genzel et al. (1993) compared with a prediction made with one energy gap.

CHAPTER 7

PERFORMANCE OF WIDELY SPACED HIGH-T_c SUPERCONDUCTOR RADIATION SHIELDS

7.1 Introduction

High-T_c superconducting films offer great promise as coatings for low-temperature radiation shields. Shields employing these materials may have radiation heat leaks considerably smaller than those employing gold films, which are at present the best films for high-performance radiation shielding. According to the BCS theory of superconductivity, a superconductor absorbs only photons possessing an energy greater than the energy gap between the normal and superconducting energy bands (Tinkham, 1980). The improvement achieved with cryogenic thermal radiation shields fabricated from high-T_c superconductors arises from the fact that the energy-gap wavelength of these materials is short compared to the wavelength of maximum emissive power at temperatures below 30 K. For incident radiation with wavelengths longer than the energy-gap wavelength, the reflectance of a superconductor is close to unity. The high-T_c superconductor is able to reflect a large portion of the low-temperature radiative energy, providing highly effective radiation shielding.

Leung et al. (1979) suggested the use of superconductors as radiation shields, but concluded that the then-known superconductors were of limited value as reflectors of infrared radiation due to their low superconducting transition temperature, T_c. Zeller (1990) made a preliminary prediction of the performance of radiation shields of high-T_c superconductors by estimating the heat flux between two parallel plates with emissivities independent of direction and wavelength and assuming that all radiation at wavelengths greater than the energy-gap wavelength is not absorbed. Zhang et al. (1994) improved this assessment of shield performance with a heat flux prediction employing normal-direction spectral emissivities for the plate materials.

This work assesses the performance of the high-T_c superconductor $YBa_2Cu_3O_7$ as a low temperature radiation shield by predicting the radiative heat flux between two widely spaced parallel surfaces, separated by a vacuum gap. The low-temperature surface is coated with an opaque film of $YBa_2Cu_3O_7$ with a (001)-orientation and the high-temperature surface is coated with an opaque film of either (001)-orientation $YBa_2Cu_3O_7$ or gold. For the (001)-orientation, the crystallographic *c*-axis is perpendicular to the film surface. In contrast to previous work (Zhang et al.,1994), this prediction accounts for the angular dependence of the surface emissivities. $YBa_2Cu_3O_7$ is optically anisotropic, i.e., the optical constants of the crystallographic *ab*-plane are different from the *c*-axis properties. The influence of the anisotropy of the $YBa_2Cu_3O_7$ optical constants on the radiative heat flux is assessed for the first time. The benefit of employing $YBa_2Cu_3O_7$ on both the low- and high-temperature surfaces is established.

A prediction of the angle-dependent emissivities requires the material optical constants. The low-temperature optical constants of gold are obtained using the anomalous skin effect theory (Reuter and Sondheimer, 1948). The dielectric function of Zhang et al. (1994) is used for the $YBa_2Cu_3O_7$ *ab*-plane optical constants. A dielectric function for the *c*-axis optical constants is proposed in this work using the Zimmermann theory (Zimmermann et al., 1991) for the superconducting free-carrier conductivity and the Lorentz damped harmonic oscillator model to account for bound charges. Optimal model parameters are determined by fitting the predicted reflectance to single-crystal measurements performed by Koch et al. (1990).

7.2 Radiative Heat Flux Prediction

The performance of radiation shields is assessed by considering the idealized system in Fig. 7.1, which consists of two optically smooth semi-infinite materials separated by a vacuum gap. The shields are maintained at uniform temperatures, T_H and T_L, and a net radiative heat flux exists between the plates due to this temperature difference. The magnitude of the radiative heat flux depends on the radiative properties of the materials, the temperature of each surface, and the size of the spacing between them. In this analysis, the surfaces are assumed to be widely spaced, so that the effects of radiation tunneling and wave interference can be neglected. There is some disagreement in the literature regarding the criteria which must be met for the spacing to influence the net radiative heat flux. Hargreaves (1973) conducted radiative heat transfer measurements for two chromium surfaces separated by a vacuum gap. An increase of 10 percent over the widely spaced measurement was observed when the product of the spacing and the average surface temperature was approximately 0.78 mm K, which agrees well with the theoretical prediction of Polder and Van Hove (1971). Caren (1974) predicted that the net radiative heat flux between two metallic surfaces differed from the widely spaced prediction when the product of spacing and temperature is less than 10 mm K. For a temperature of 5 K, the influence of spacing on the radiative heat flux must be considered for a spacing of less than 0.16 mm using the Hargreaves result or less than 2 mm using the result of Caren.

The present analysis assumes that the emission of radiation from each surface corresponds to the equilibrium intensity of thermal radiation, that is, the resulting emission from a surface at temperature, T, if both surfaces were at the same temperature. Under this equilibrium condition, the intensity of radiation in the vacuum space is the product of the directional spectral emissivity of the surface and the Planck distribution function for unpolarized blackbody radiation

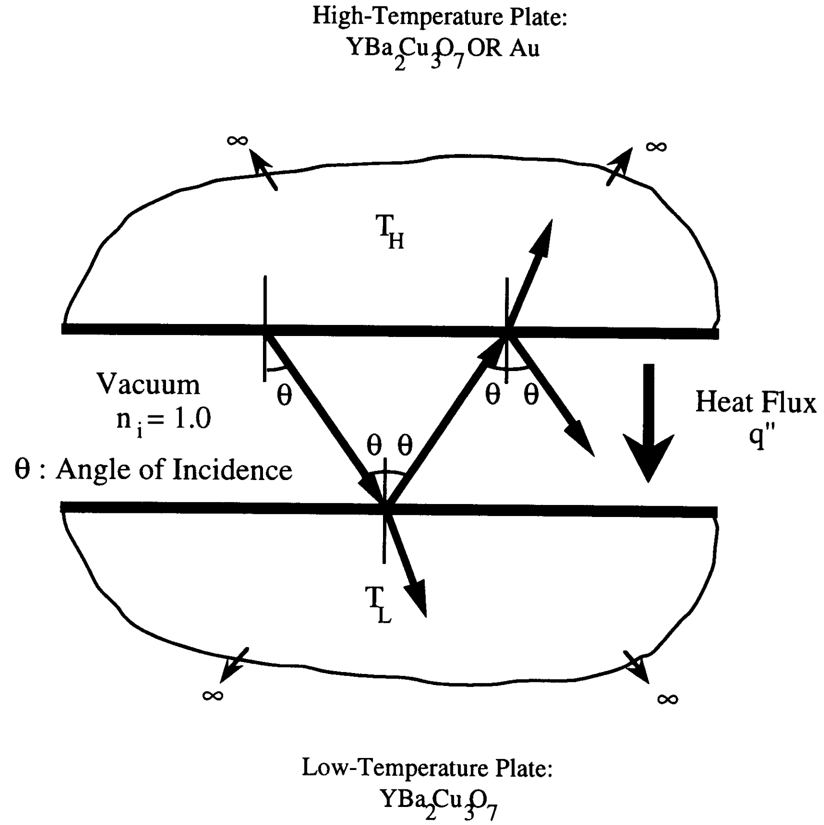

Figure 7.1 Configuration of radiation shield system.

$$I_\lambda(\theta,\varphi,\lambda,T) = \varepsilon'_\lambda(\theta,\varphi,\lambda) I_{b\lambda}(\lambda,T) = \varepsilon'_\lambda(\theta,\varphi,\lambda) \frac{hc_0^2}{\pi\lambda^5\left[\exp\left(hc_0/(k_B\lambda T)\right)-1\right]} \tag{7.1}$$

By considering the multiple reflections suffered by the radiation within the vacuum cavity, Domoto and Tien (1970) determined the portion of the net radiative heat flux corresponding to either transverse electric field, TE, or transverse magnetic field, TM, polarization. Rewriting their expression in terms of directional spectral emissivities yields

$$q''_{\mathrm{net}}(T_L,T_H)_{\mathrm{TE,TM}} = \int_0^\infty \int_0^{2\pi} \int_0^{\pi/2} \frac{I_{b\lambda}(\lambda,T_H) - I_{b\lambda}(\lambda,\mathrm{T_L})}{1/\varepsilon'_{\lambda,\mathrm{H}}(\theta,\varphi,\lambda) + 1/\varepsilon'_{\lambda,\mathrm{L}}(\theta,\varphi,\lambda) - 1} \cos\theta \sin\theta \, d\theta \, d\varphi \, d\lambda \tag{7.2}$$

To account for the difference in emissivities for the two polarizations, Domoto and Tien (1970) considered the net radiative heat flux to be the arithmetic average of the TE and TM contributions

$$q''_{\mathrm{net}} = \frac{(q''_{\mathrm{net}})_{\mathrm{TE}} + (q''_{\mathrm{net}})_{\mathrm{TM}}}{2} \tag{7.3}$$

Equation (7.3), with Eq. (7.2), provides the prediction for the net radiative flux between parallel widely spaced surfaces.

The TE and TM directional spectral emissivities are obtained from the directional spectral absorptivities by applying Kirchhoff's law, which equates the directional spectral emissivity and absorptivity for a given state of polarization (Siegel and Howell, 1992). Kirchhoff's law is valid independent of the radiation field surrounding the body provided that the distribution of the material states of the body is the equilibrium distribution (Baltes, 1976). The TE and TM directional spectral absorptivities are obtained by applying an energy balance for each polarization at the interface of the nontransmitting semi-infinite plate material. The TE and TM directional-hemispherical spectral reflectivities are calculated from the Fresnel reflection coefficients. The directional-hemispherical spectral reflectivities for a uniaxial material with a (001)-orientation were given by Malone et al. (1993), as a function of the angle of incidence, θ

$$1-\varepsilon'_{\lambda,\mathrm{TE}}=\rho'_{\lambda,\mathrm{TE}}=\left|r_{\mathrm{TE}}\right|^2=\left|\frac{n_{\mathrm{i}}\cos\theta-\sqrt{\bar{n}_{\mathrm{o}}^2-n_{\mathrm{i}}^2\sin^2\theta}}{n_{\mathrm{i}}\cos\theta+\sqrt{\bar{n}_{\mathrm{o}}^2-n_{\mathrm{i}}^2\sin^2\theta}}\right|^2 \tag{7.4}$$

$$1-\varepsilon'_{\lambda,\mathrm{TM}}=\rho'_{\lambda,\mathrm{TM}}=\left|r_{\mathrm{TM}}\right|^2=\left|\frac{\bar{n}_{\mathrm{o}}\bar{n}_{\mathrm{e}}\cos\theta-n_{\mathrm{i}}\sqrt{\bar{n}_{\mathrm{e}}^2-n_{\mathrm{i}}^2\sin^2\theta}}{\bar{n}_{\mathrm{o}}\bar{n}_{\mathrm{e}}\cos\theta+n_{\mathrm{i}}\sqrt{\bar{n}_{\mathrm{e}}^2-n_{\mathrm{i}}^2\sin^2\theta}}\right|^2 \tag{7.5}$$

Equations (7.4) and (7.5) are used to calculate the directional spectral emissivity of the anisotropic superconductor $YBa_2Cu_3O_7$ with a (001)-orientation. The ordinary complex refractive index $\bar{n}_{\mathrm{o}}$ refers to the $YBa_2Cu_3O_7$ *ab*-plane complex refractive index and the extraordinary complex refractive index $\bar{n}_{\mathrm{e}}$ refers to the $YBa_2Cu_3O_7$ *c*-axis complex refractive index. Substituting $\bar{n}_{\mathrm{o}}=\bar{n}_{\mathrm{e}}=\bar{n}$ into Eq. (7.4) and Eq. (7.5) yields the emissivity for gold.

7.3 Dielectric Function Tensor Model for Superconducting $YBa_2Cu_3O_7$

7.3.1 Model Basics

A prediction of the radiative heat flux for shielding employing $YBa_2Cu_3O_7$ requires the frequency-dependent complex dielectric function $\bar{\varepsilon}=\bar{n}^2=(n+\mathrm{i}\kappa)^2$ of the surface materials. The complex dielectric function for $YBa_2Cu_3O_7$ is a tensor with different values for each axis of the principal dielectric axis system. For (001)-orientation $YBa_2Cu_3O_7$ films, twinning occurs in the *ab*-plane whereby the *a* and *b* axes alternate in orientation (Zhu et al., 1990). To describe the reflectance of light incident along the *c*-axis, an average dielectric function is required: the *ab*-plane dielectric function. The dielectric functions for the *ab*-plane and *c*-axis are obtained by fitting a dielectric function model to *ab*-plane and *c*-axis reflectance measurements.

The frequency-dependent dielectric function model for the *ab*-plane and the *c*-axis of $YBa_2Cu_3O_7$ for temperatures not too close to T_c has the general form of a linear superposition of terms (Timusk and Tanner, 1989)

$$\bar{\varepsilon}(\omega)=(n+\mathrm{i}\kappa)^2=\varepsilon_\infty+\sum_{\text{phonons}}\frac{S_{\mathrm{j}}\omega_{\mathrm{j}}^2}{\omega_{\mathrm{j}}^2-\omega^2-\mathrm{i}\omega\gamma_{\mathrm{j}}}+\frac{S_{\mathrm{e}}\omega_{\mathrm{e}}^2}{\omega_{\mathrm{e}}^2-\omega^2-\mathrm{i}\omega\gamma_{\mathrm{e}}}+\frac{\mathrm{i}\sigma(\omega)}{\omega\varepsilon_0} \tag{7.6}$$

where ε_∞ is the high-frequency dielectric constant. The second term is the infrared-active phonon contribution to the dielectric function, due to the vibrations of lattice ions, which is described by the Lorentz damped oscillator model (Brewster, 1992). The model parameters are the strength S_j, the center frequency ω_j, and the damping coefficient γ_j for each phonon j present in the frequency range considered by the dielectric function model. The third term is a midinfrared absorption band term, considered using the Lorentz model, which accounts for interband electronic transitions (Timusk and Tanner, 1989). It has a strength S_e, a center frequency ω_e, a plasma frequency ω_{pe}, and a damping coefficient γ_e. The free-carrier contribution to the dielectric function is represented in the final term, where ε_0 is the electrical permittivity of free space and $\sigma(\omega)$ is the free-carrier conductivity.

Zhang et al. (1994) proposed the free-carrier conductivity model used in this work. It consists of two components: a BCS free-electron conductivity σ_{ss} for electrons whose behavior is described by the BCS microscopic theory of superconductivity (Bardeen et al., 1957) and a residual normal-state free-electron conductivity σ_{nr} for electrons which remain in the normal state below T_c. The contribution of each component to the conductivity is given by a weighted sum

$$\sigma(\omega) = (1 - f_{nr})\sigma_{SS}(\omega) + f_{nr}\sigma_{nr}(\omega) \tag{7.7}$$

where f_{nr} is the temperature-independent fraction of residual normal-state electrons. The Drude model is used to account for the normal-state free-electron conductivity σ_{nr}.

7.3.2 BCS-Electron Conductivity

The BCS free-electron conductivity for $YBa_2Cu_3O_7$ is predicted from expressions given by Zimmermann et al. (1991), which were derived within the framework of the BCS superconductivity theory (Bardeen et al., 1957). By modeling the response of electrons to a space- and time- dependent electric field, Zimmermann et al. (1991) obtained the free carrier motion for a weakly coupled superconductor with arbitrary purity, i.e., valid for any value of the electron mean free path.

Zimmermann et al. (1991) gives the functional dependence of the complex conductivity as:

$$\sigma_{ss}(\omega,T)=\sigma_{dc}\ \mathrm{F}\left(x={}^{\omega h}\!/_{4\pi\Delta},Y={}^{h}\!/_{4\pi\tau\Delta},{}^{T}\!/_{T_c}\right) \tag{7.8}$$

where σ_{dc} is the dc electrical conductivity, and F is a function of the normalized frequency, x, the ratio of sample to transition temperature, T/T_c, and the normalized electron scattering rate, $Y = h/(4\pi\tau\Delta)$, where h is Planck's constant, $1/\tau$ is the electron scattering rate, and Δ is the superconductor energy gap.

The purity of a superconductor is measured by the ratio of the superconductor coherence length, ξ, the lengthscale over which electrons are correlated in the superconducting state, to the mean free path of the electrons (Orlando and Delin, 1991). The normalized scattering rate, Y, is proportional to the purity. For $Y >> 1$, the superconductor is in the impure limit and the theory of Zimmermann et al. (1991) gives the same results as the theory of Mattis and Bardeen (1958), which is valid for impure isotropic superconductors. For a pure superconductor such as $YBa_2Cu_3O_7$ for which $Y < 1$ (Flik et al., 1992), the Mattis-Bardeen theory yields a large error.

It should be noted that while the Zimmermann theory accounts for arbitrary purity, its validity is strictly limited to weakly coupled (BCS) superconductors. The coupling strength between electrons and phonons in a superconductor is defined in terms of the energy gap parameter, $A = 2\Delta_0/k_B T_c$ (Burns, 1990) where k_B is the Boltzmann constant and Δ_0 is the superconductor energy gap at 0 K. For a BCS weakly coupled superconductor, A is approximately 3.53. Values of A in excess of 3.53 are indicative of strong electron-phonon coupling. Another requirement for the applicability of the Zimmermann model is that the superconducting coherence length, ξ, must be smaller than both the wavelength of incident radiation, λ, and the magnetic penetration depth. Zhang et al. (1992) showed that these conditions are satisfied for the *ab*-plane of $YBa_2Cu_3O_7$ for $\lambda > 1$ μm and temperatures not too close to T_c. The *c*-axis coherence length is much shorter than the *ab* plane coherence length: $\xi_c =$ 0.2-0.4 nm and $\xi_{ab} =$ 12-25 nm (Annett et al., 1990). The magnetic penetration depth for $\lambda > 1$ μm is close to the dc value, which is the London penetration depth. The *c*-axis London penetration depth for $YBa_2Cu_3O_7$ at 0 K is greater than 700 nm (Harshmann et al., 1989). Hence, the conditions for the applicability of the Zimmermann theory are satisfied for the *c*-axis of $YBa_2Cu_3O_7$.

7.4 *ab*-Plane Dielectric Function Model

This work employs the *ab*-plane dielectric function model proposed by Zhang et al. (1994). Zhang et al. (1994) used f_{nr}, A, and Y as adjustable parameters to obtain the best agreement between the reflectivity predicted by the dielectric function model and five sets of reflectivity measurements for the spectral region from 5 to 200 μm. They recommend using values of $f_{nr} = 20$ percent, $Y = 0.22$ and $A = 7$. The recommended value of $A = 7$ indicates strong electron-phonon coupling in the *ab*-plane of $YBa_2Cu_3O_7$, which violates the weak-coupling requirement of the theory of Zimmermann et al. (1991), thereby raising some question as to the suitability of this approach. The conductivity expression may be modified to allow for an arbitrary electron-phonon coupling strength by employing the approach of Lee et al. (1989).

7.5 *c*-axis Dielectric Function Model

A dielectric function model for the *c*-axis is developed by fitting Eq. (7.6) with adjustable parameters to the *c*-axis reflectivity of Koch et al. (1990), measured at 10 K for the wavelength region between 15 and 200 μm. The high-frequency dielectric constant is set at $\varepsilon_\infty = 4.8$, as used by Bauer (1990). Koch et al. (1990) observed eight oscillators in the measured data and reported the center frequencies, but did not develop a dielectric function model for the data. Of the eight oscillators, the five strongest are included in the dielectric function model presented in this work. The center frequencies are fixed at the values reported by Koch et al. (1990). These frequencies closely match those chosen for Lorentz oscillator fits by Bauer (1990) for a single crystal sample and Ose (1990) for a polycrystalline sample, and those calculated from lattice dynamics studies (Genzel, 1989; Liu et al., 1988). Bauer (1990) included a weak phonon at 610 cm^{-1}, which is not included in the present work. These works are reviewed by Renk (1992). The superconducting energy gap parameter A was fixed at 1.4, indicative of very weak coupling, as reported by Koch et al. (1990). This corresponds to an energy gap wavelength of 114 μm. Koch et al. (1990) commented on evidence of a mid-infrared absorption band at approximately 480 cm^{-1}, but it is not included in this dielectric function model as an improved fit is obtained by excluding this term. The fraction of residual normal-state electrons f_{nr} is set at 0 percent. For the *ab*-plane, Zhang et al. (1994) suggested an f_{nr} = 20 percent. They suggest that the free-carriers in the CuO chains are the source of the residual normal-state electrons. It is proposed that since the CuO chain bonds are not activated for radiation polarized along the *c*-axis, there should be no residual normal-state electrons. Microwave absorptivity data are required to confirm this assumption.

The oscillator strengths S_1-S_5 and the damping coefficients γ_1-γ_5, the dc electrical conductivity σ_{dc}, and normalized electron scattering rate, Y, are treated as adjustable parameters in Eq. (7.6). The optimal parameters are obtained by fitting the measured reflectance using the Levenberg-Marquardt method (Press et al., 1986), which is a method of minimizing the merit function χ^2. This fitting method provides estimates of the uncertainties in the optimized parameters based on the 1 percent uncertainty in the reflectance measurements reported by Koch et al. (1990). This method was employed by Hebb et al. (1993) to fit the measured absorptance of doped GaAs. Table 7.1 shows the optimal oscillator strengths and damping coefficients, and Table 7.2 shows a comparison of *ab*-plane and *c*-axis dielectric function model properties, including the optimal values for Y and σ_{dc}. The uncertainties in the parameters are given with a 95 percent confidence interval, assuming that the errors in the measured data points are independent and have a normal distribution (Press et al., 1986). The reflectivity predicted by the dielectric function model with the optimal parameters is compared to the measured data in Fig. 7.2. Figs. 7.3a and 7.3b show the

Table 7.1 $YBa_2Cu_3O_7$ *c*-axis oscillator center frequencies, strengths, and damping coefficients.

j	ω_j (cm^{-1})	S_j	γ_j (cm^{-1})
1	566	11.8 ± 1.0	504 ± 12.8
2	312	0.50 ± 0.2	0.07 ± 0.06
3	287	3.1 ± 0.6	28.6 ± 6.2
4	192	0.42 ± 0.08	5.9 ± 1.4
5	152	5.4 ± 0.2	4.2 ± 0.6

Table 7.2 Comparison of $YBa_2Cu_3O_7$ *ab*-plane and *c*-axis dielectric function model properties (*ab*-plane values from Zhang et al. (1994)).

	ε_∞	f_{nr}	$Y = \frac{h}{4\pi\tau\Delta}$	$A = \frac{2\Delta_0}{k_B T_c}$	$\sigma_{dc} = \frac{N_e e^2 \tau}{m_e}$ $(\Omega^{-1} m^{-1})$
ab-plane	4.0	20%	0.22	7	2.5×10^6
c-axis	4.8	0%	0.20 ± 0.02	1.4	5.15×10^4 $\pm 4.6 \times 10^3$

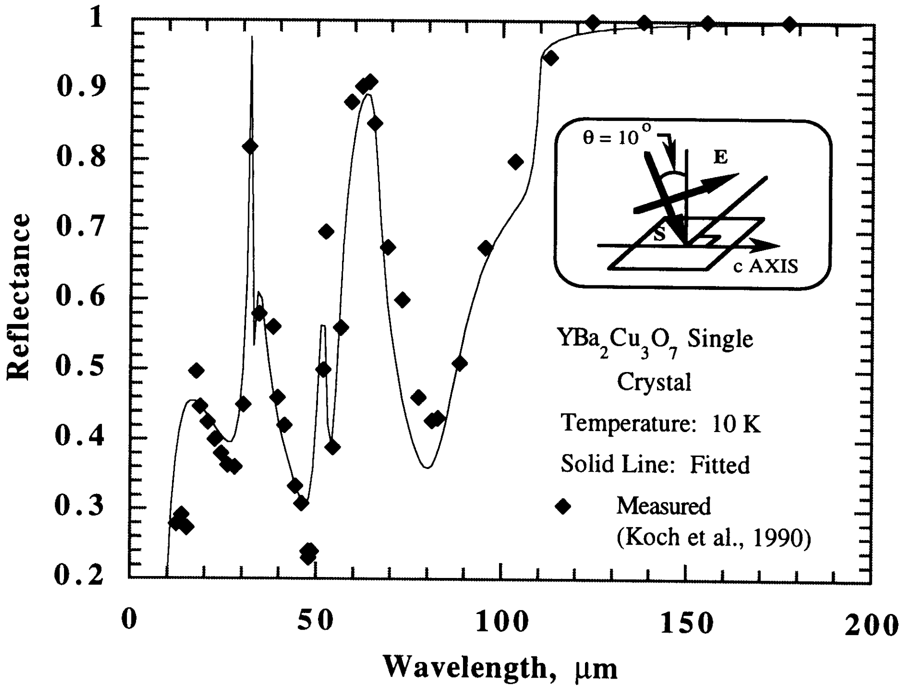

Figure 7.2 Comparison of the calculated reflectance from the fitted dielectric function model to that measured by Koch et al. (1990) for the *c*-axis of $YBa_2Cu_3O_7$

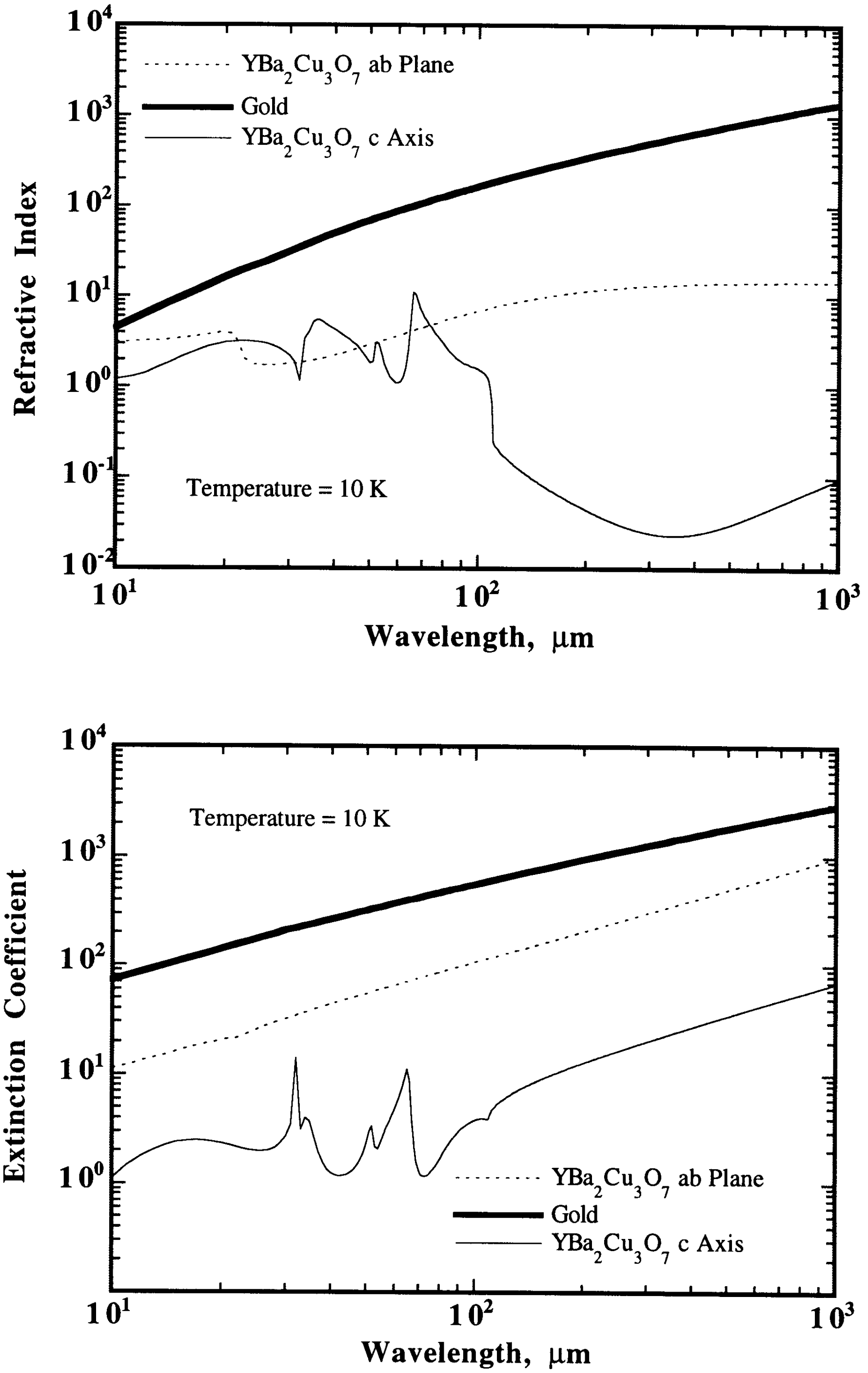

Figure 7.3 The optical constants for gold and $YBa_2Cu_3O_7$ calculated from theory at 10 K. (a) Refractive index, *n*. (b) Extinction coefficient, *κ*.

refractive indices and extinction coefficients predicted for $YBa_2Cu_3O_7$ and gold. Note the sharp change in the *ab*-plane and *c*-axis refractive indices at the gap wavelengths.

The optimal oscillator strengths and damping coefficients used in this model are similar to values determined by Bauer (1990) and Ose (1990), with the exception of the oscillator at 566 cm^{-1}, which has a much larger strength and damping coefficient. The shoulder in the reflectance spectra caused by a midinfrared absorption band in the region of the oscillator is fit to obtain the best agreement between the measured data and the predicted reflectance. This oscillator accounts for the combined effect of the midinfrared absorption band and the oscillator at 566 cm^{-1}. The uncertainty in the strength and damping coefficient of the oscillator at 312 cm^{-1} is large, indicating that it has a very small influence on the reflectance spectra. Liu et al. (1988) also showed from lattice dynamics studies that this oscillator was very weak.

The optimal *c*-axis $\sigma_{dc,c} = 5.15 \times 10^4$ is approximately 1/50 of the *ab*-plane value recommended by Zhang et al. (1994). The *ab*-plane $\sigma_{dc,ab}$ in the superconducting state is a hypothetical value extrapolated from normal-state electrical resistivity data using the method of Goodson and Flik (1992). This method is based on Matthiessen's rule by considering electron-phonon and electron-defect scattering. The temperature-dependence of the electrical resistivity due to electron-phonon scattering is determined using the Bloch formula. Electrical resistivity measurements show a ratio of approximately 30-70 between the *c*-axis and the *ab*-plane resistivities (Iye, 1992) indicating that the optimal value for $\sigma_{dc,c}$ is of the correct order-of-magnitude. The optimal normalized electron scattering rate for the *c*-axis is $Y_c = 0.20$, which indicates that the *c*-axis of $YBa_2Cu_3O_7$ is in the clean limit. The normalized electron scattering rates for the *ab*-plane and the *c*-axis are approximately equal. Due to the gap anisotropy, at 0 K, the *c*-axis electron scattering rate $1/\tau_c$ is 1/5 of the *ab*-plane value. The reduction in the electron scattering rate may be attributed to the large anisotropy in the electron effective mass where the ratio of the *c*-axis to *ab*-plane effective masses is approximately 25-50 (Iye, 1992) or to a lower electron number density.

Both of these parameters would influence the *c*-axis electron scattering rate. The cause of the reduced electron scattering rate requires further investigation.

7.6 Optical Constants of Gold

Free-carrier absorption is the dominant mechanism of absorption in the infrared portion of the electromagnetic spectrum for metals. The Drude single electron theory treats the electrons as classical particles under the influence of an applied electric field, assuming that the field does not vary in magnitude over the mean free path of the electron. At low temperatures, the penetration depth of incident radiation decreases due to increased conductivity, while the mean free path of the electrons increases. When the mean free path is comparable to the penetration depth, classical theory is no longer valid (Reuter and Sondheimer, 1948). The anomalous skin effect theory (Reuter and Sondheimer, 1948) allows for a space-dependent electric field, which accounts for the long mean free path of the electrons at cryogenic temperatures. It has been shown experimentally (Toscano and Cravalho, 1976) and theoretically (Domoto et al., 1969) that the anomalous skin effect theory is appropriate for the prediction of radiative properties of metals at cryogenic temperatures.

Reuter and Sondheimer (1948) developed a method to calculate the surface impedance, Z, of a metal based on the assumption that the free carriers move under the influence of a space- and time-dependent electric field. Reuter and Sondheimer (1948) obtained an integro-differential equation for the electric field amplitude, the solution of which can be used to determine the surface impedance.

Collins (1958) showed that for cryogenic temperatures the complex refractive index is related to surface impedance in the infrared spectral region by

$$\bar{n} = \frac{\mu c_0}{Z} \tag{7.9}$$

where c_0 is the speed of light in vacuum, and Z is the surface impedance. The optical constants obtained using the anomalous skin effect theory are substituted into Eqs. (7.4) and (7.5) to provide the emissivity of gold as required for the calculation of the net radiative heat transfer.

Dingle (1953) provided series solutions to the integro-differential equations of Reuter and Sondheimer (1948). In the present analysis, the solutions for the case of diffuse electron reflection at the metal surface are used, which is the case most strongly indicated by experimental investigation (Toscano and Cravalho, 1976). The input parameters for the series solutions are the number density of free electrons, N_e, the effective electron mass, m_e, and dc electrical conductivity, σ_{dc}. The number density of free electrons and effective electron mass for gold were obtained from Burns (1990). The temperature dependence of the dc electrical conductivity is obtained from the Bloch-Grüneisen formula (Wilson, 1953), and the electrical resistivity is calculated using Matthiessen's rule (MacDonald, 1956). The optical constants of gold obtained from the solutions given by Dingle (1953) are shown in Figs. 7.3a and 7.3b for a temperature of 10 K.

7.7 Performance of Radiation Shields

Figures 7.4a and 7.4b present the heat flux predictions for the parallel plate system for two values of T_L: 4.2K, which is the boiling point of liquid helium at atmospheric pressure and 1.8 K, the lower limit of the lambda-line in the phase diagram for helium, which may be achieved by pumping on liquid helium (Mendelssohn, 1960). These are representative of two possible radiation-shielding temperature requirements for the storage of liquid helium. A heat flux prediction for a system of two gold surfaces is shown to provide a benchmark for the comparison to the proposed systems. The new systems considered here consist of a low temperature surface of $YBa_2Cu_3O_7$ and a high temperature surface of either gold or $YBa_2Cu_3O_7$.

Zhang (1994) performed similar predictions, but did not consider the angle dependence of the emissivity nor the anisotropy in the optical constants of $YBa_2Cu_3O_7$. The present study

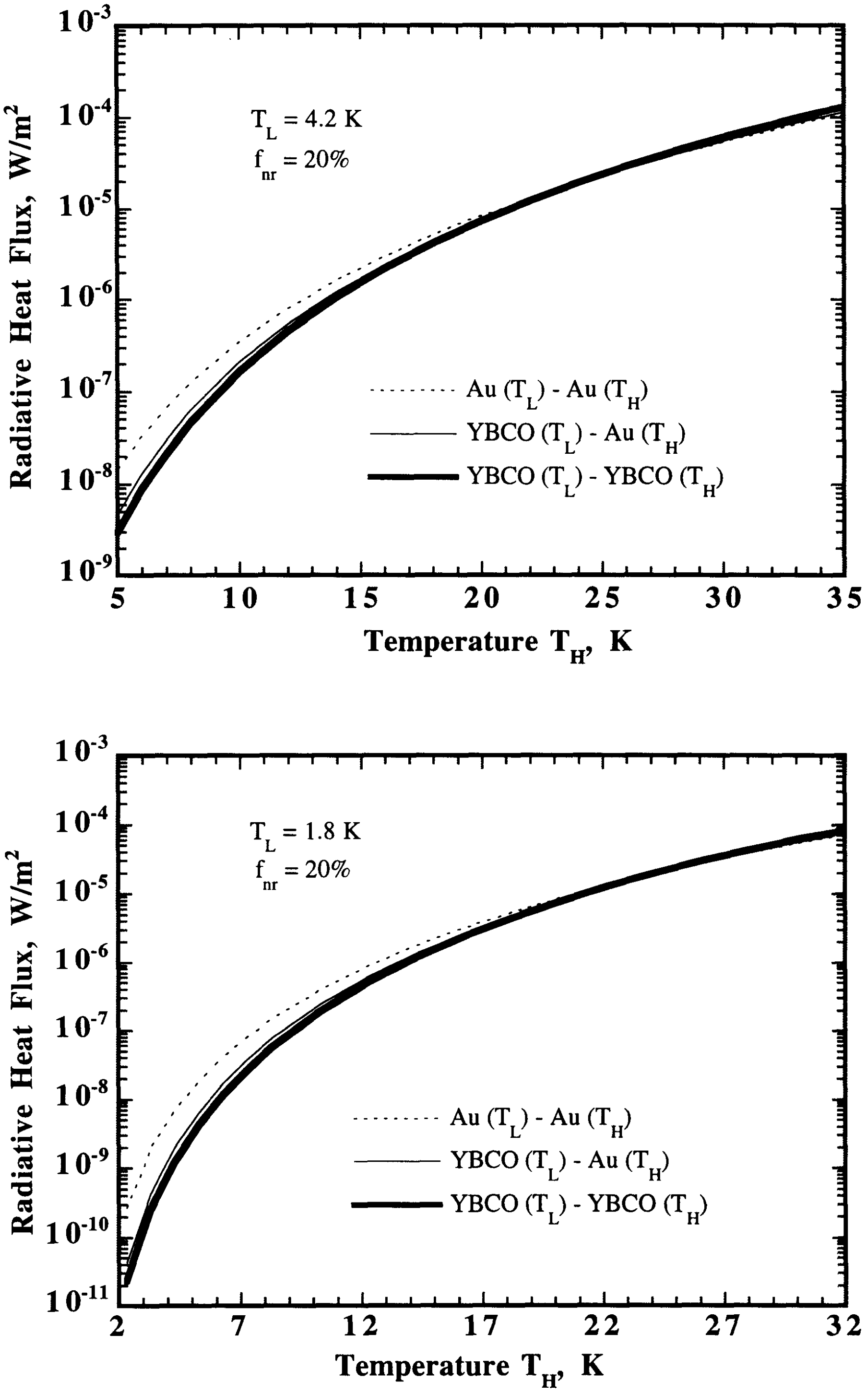

Figure 7.4 The predicted net radiative heat flux for the system shown in Fig. 7.1. (a) $T_L = 4.2$ K. (b) $T_L = 1.8$ K.

indicates that over the temperature range shown in Figs. 7.4a and 7.4b, the radiative heat flux prediction for all three systems is approximately 33 percent greater when the angle-dependent emissivity is considered than that for which the emissivity was assumed to be constant over all angles of incidence and equal to the value of the normal emissivity. The effect of including the anisotropic optical constants of $YBa_2Cu_3O_7$ on the net radiative flux is small. An increase of less than 5 percent is obtained when the anisotropic optical constants are included as compared to the heat flux predicted using the *ab*-plane optical constants for the *c*-axis. The anisotropy of the optical constants does not greatly influence the radiative heat flux because at long wavelengths, $\lambda >$ 100 μm, where the major fraction of the total emissive power is emitted at low temperatures, the reflectivity of both the *ab*-plane and the *c*-axis approaches unity. The optical anisotropy has little influence on the directional spectral emissivity.

A comparison of Figs. 7.4a and 7.4b indicates that for $T_H > 5K$ the predictions for the case of the low temperature surface at 1.8K and 4.2K agree to within 5 percent. The deviation between the two cases increases as T_H approaches T_L. This result can be explained by the fact that in both cases, T_L is so close to absolute zero that the amount of radiative heat flux emitted by the cold surface is quite small compared to that being emitted by the hot surface. For a relatively high T_H, the presence of the cold surface is unimportant, and the net radiative heat flux is the same for both $T_L = 1.8K$ and $T_L = 4.2K$. As T_H approaches T_L the temperature of the cold surface becomes significant compared to T_H, and the net radiative heat flux differs slightly.

To provide a clearer presentation of the improvement offered by employing $YBa_2Cu_3O_7$ in a radiation shield system, Figs. 7.5a and 7.5b display the relative difference between the heat flux predicted for both the $YBa_2Cu_3O_7$-$YBa_2Cu_3O_7$ system and the $YBa_2Cu_3O_7$-gold system as compared to the benchmark gold-gold system. The relative difference is defined as

$$\delta_{(\mathrm{YBCO-X})-(\mathrm{Au-Au})} = \frac{q''_{(\mathrm{YBCO-X})} - q''_{(\mathrm{Au-Au})}}{q''_{(\mathrm{Au-Au})}} \tag{7.10}$$

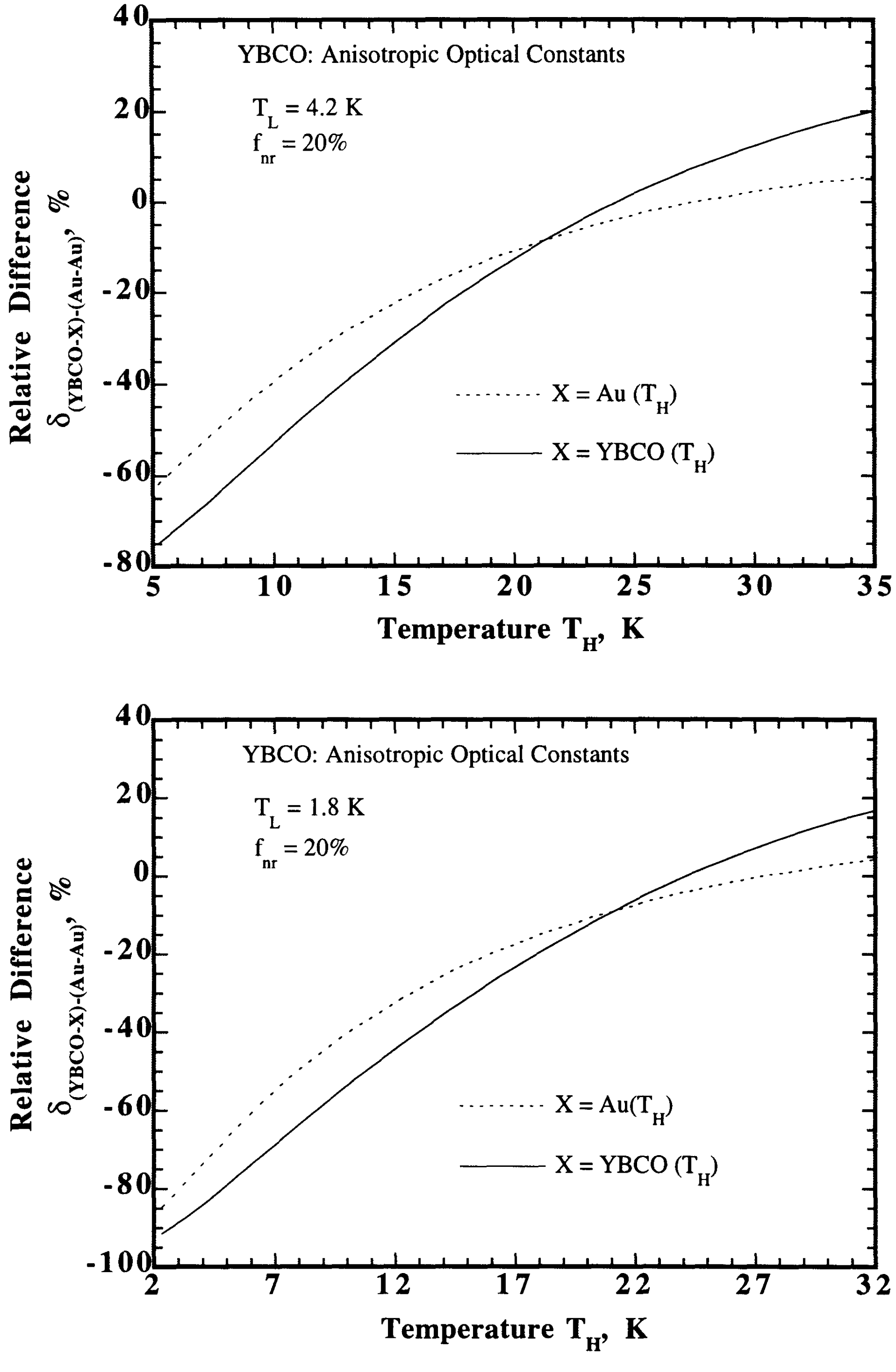

Figure 7.5 The relative difference between the net radiative heat flux predictions for systems employing $YBa_2Cu_3O_7$ and the gold-gold system. (a) T_L = 4.2 K. (b) T_L = 1.8 K.

where X represents the hot surface material, either $YBa_2Cu_3O_7$ or gold. By this definition, a negative relative difference represents an improvement, i.e., a smaller heat flux in the system employing $YBa_2Cu_3O_7$.

When the hot surface has a temperature T_H in excess of approximately 27.5 K, Figs. 7.5a and 7.5b indicates that shields employing $YBa_2Cu_3O_7$ on the cold surface offer no improvement over the gold-gold system. When $YBa_2Cu_3O_7$ is used for both the hot and cold surfaces, the shields offer no improvement for $T_H > 24.5$ K. This is due to the shift in the wavelength of maximum emissive power to shorter wavelengths with increasing temperature. The spectral emissivity of gold at 4 K is smaller than $YBa_2Cu_3O_7$ for wavelengths shorter than approximately 100 μm (Zhang et al., 1992). As the hot surface temperature increases, more energy is emitted at shorter wavelengths, reducing the shielding improvement offered by using $YBa_2Cu_3O_7$.

When T_H is less than approximately 21.5 K, a system employing $YBa_2Cu_3O_7$ on both surfaces provides the best shielding, as the energy emitted by the hot surface shifts to longer wavelengths. If $T_H = 8$ K and $T_L = 1.8$ K or 4.2 K, the $YBa_2Cu_3O_7$-$YBa_2Cu_3O_7$ system offers an improvement of approximately 65 percent over the gold-gold system and an improvement of 15 percent over the system with a low-temperature $YBa_2Cu_3O_7$ surface and a high-temperature gold surface. Figure 7.5b shows that as T_H approaches T_L, a reduction in the net heat flux of approximately 90 percent is achieved.

If the fraction of residual normal-state electrons f_{nr} in the *ab*-plane is not an intrinsic property of the material and may be decreased by improvements in processing techniques, a significant improvement in the shield performance may be achieved. If f_{nr} is reduced from 20 percent to 5 percent, a $YBa_2Cu_3O_7$ -$YBa_2Cu_3O_7$ shield with $T_L = 1.8$ K or 4.2 K and $T_H = 8$ K reduces the heat flux by 145 percent over the gold-gold system, an improvement of 80 percent over shields made from the best $YBa_2Cu_3O_7$ material available today. The nature of the normal-state residual electrons requires further investigation.

7.8 Conclusions

1. By considering the angle-dependent emissivity of the surfaces, the net radiative heat flux predictions increase by approximately 33 percent over the predictions made assuming that the emissivity is independent of angle and equal to the normal emissivity, demonstrating the importance of using the appropriate relations for the angle-dependent emissivity. By considering the anisotropy of the optical constants of $YBa_2Cu_3O_7$, the radiative heat flux prediction changes by less than 5 percent from the prediction performed using the *ab*-plane optical constants for the *c*-axis.

2. More effective radiation shielding can be obtained by utilizing $YBa_2Cu_3O_7$ for one or both of the surface coatings. The largest reduction in the radiative heat flux is achieved for shields employing $YBa_2Cu_3O_7$ on both surfaces. This analysis predicts a reduction in the net radiative flux of as much as 90 percent with such a system over gold-gold systems. An improvement over gold-gold systems is realized for hot-surface temperatures below 27.5 K using $YBa_2Cu_3O_7$ on the cold surface and gold on the hot surface. A reduction in the radiative heat flux compared to gold-gold systems is achieved for $YBa_2Cu_3O_7$-$YBa_2Cu_3O_7$ systems when the hot-surface temperature is less than 24.5 K. These temperature limitations are valid for cold-surface temperatures of either 1.8 K or 4.2 K.

3. If the fraction of residual normal state electrons in the *ab*-plane of $YBa_2Cu_3O_7$ can be reduced from 20 percent to 5 percent, a dramatic reduction in the radiative heat flux (from the gold-gold system) can be obtained. Substantially improved radiation shielding could be fabricated if this reduction is achievable.

4. The present work determines the superconducting conductivity of $YBa_2Cu_3O_7$ by applying the Zimmermann theory, which is strictly valid for weakly-coupled superconductors. Recent studies that support the existence of an energy gap indicate that the $YBa_2Cu_3O_7$ *ab*-plane coupling is strong. The Zimmermann theory, therefore, may not be appropriate for the $YBa_2Cu_3O_7$ *ab*-

plane conductivity. Further investigation is needed to provide a means with which to calculate the optical constants of $YBa_2Cu_3O_7$ which considers the strong coupling and high purity of these materials.

CHAPTER 8

OPTIMIZED DESIGN OF FAR-INFRARED FABRY-PÉROT RESONATORS FABRICATED FROM $YBa_2Cu_3O_7$

8.1 Introduction

For many years, far-infrared Fabry-Pérot resonators have been successfully fabricated using metal mesh structures (Renk and Genzel, 1962). They are used for far-infrared laser spectroscopy, astronomy, and most recently, for the precise measurement of the far-infrared reflectance of smooth metal surfaces (Genzel et al., 1990). Sakai and Genzel (1983) reviewed the design criteria and performance of various metal-mesh Fabry-Pérot resonators.

A superconductor only absorbs photons possessing an energy greater than the energy gap between the normal and superconducting electrons of the material (Tinkham, 1980). The energy-gap frequency at zero temperature $\omega_g(0)$ of $YBa_2Cu_3O_7$ is large compared to far-infrared frequencies. Thus, the reflectance of the high-T_c superconductor $YBa_2Cu_3O_7$ approaches unity for wavenumbers lower than approximately 200 cm^{-1} at temperatures well below T_c. Increasing the reflectance of the mirrors in a Fabry-Pérot resonator dramatically improves device performance.

Thus, the $YBa_2Cu_3O_7$ Fabry-Pérot resonator should offer optimal performance characteristics in the far-infrared, possibly surpassing those of the metal mesh structures.

Renk and co-workers (Renk et al., 1990; Wiese et al., 1992) investigated experimentally and analytically the performance of far-infrared Fabry-Pérot resonators fabricated from two $YBa_2Cu_3O_7$ films deposited on MgO substrates, as shown in Fig. 8.1. They successfully demonstrated the suitability of these structures for far-infrared applications. However, the maximum transmittance and finesse of their structures were inferior to those of existing metal mesh devices. This was attributed to poor film quality and nonparallelism of the reflecting surfaces. Disagreement between the predicted and measured transmittance was, in part, explained by inaccuracies in predicting the dielectric function of the $YBa_2Cu_3O_7$ films.

The present study predicts the transmittance of a Fabry-Pérot resonator consisting of two parallel plates, each consisting of a $YBa_2Cu_3O_7$ film deposited on an MgO substrate for light incident normal to the substrate surface. The superconducting films have a (001)-orientation, i.e., the metallic *ab*-plane is parallel to the mirror surface. The influence of the substrate and film thicknesses on device performance is examined. An accurate prediction of the transmittance requires accurate *ab*-plane optical constants. These are provided using the parameters recommended by Zhang et al. (1994) for the *ab*-plane dielectric function of the best $YBa_2Cu_3O_7$ films currently available. The free-carrier conductivity component of the dielectric function is determined using the Zimmermann theory (Zimmermann et al., 1991) together with the contribution of residual normal-state electrons. To investigate possible improvement in Fabry-Pérot resonator performance with improving film quality, the faction of residual normal-state electrons in the film is reduced in the predictions below the value found for the best films currently available.

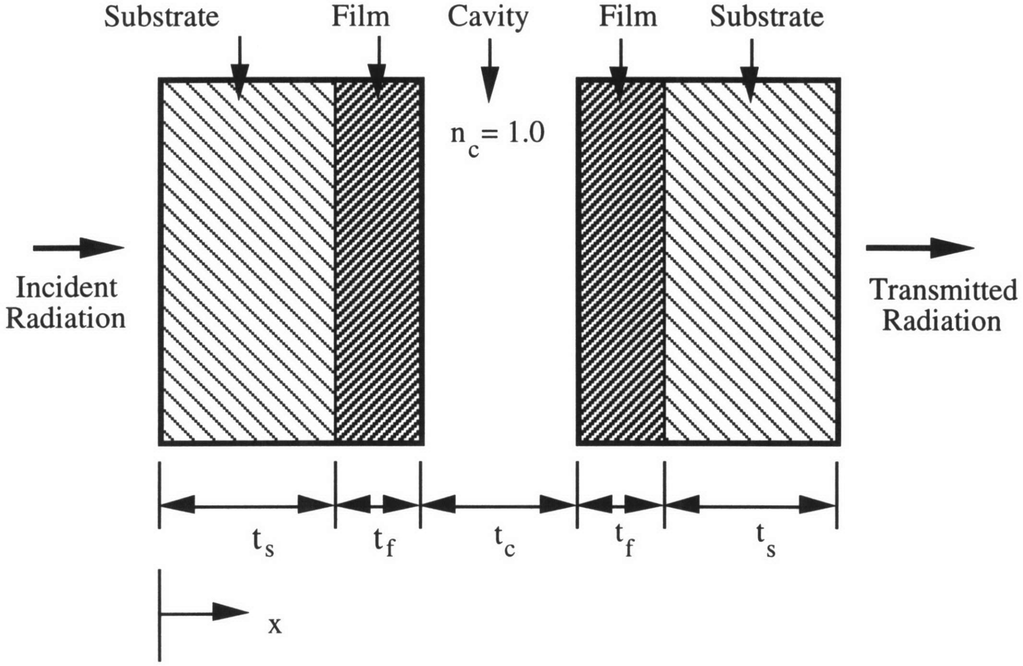

Figure 8.1 Fabry-Pérot resonator fabricated from high-T_c superconducting films.

8.2 Analysis

8.2.1 Transmittance Prediction

The transmittance of the Fabry-Pérot structure shown in Fig. 8.1 is predicted using the electromagnetic wave matrix formulation for layered media (Yeh, 1988). The surfaces are assumed to be parallel and optically smooth, i.e., the rms surface roughness is much smaller than the investigated wavelength range. The magnetic permeability of all materials is assumed to be the permeability of free space, μ_0. The method for predicting the transmittance and reflectance of the Fabry-Pérot structure is presented in Appendix A.

8.2.2 Material Optical Constants

The optical constants of MgO at 8 K are obtained from a Lorentz model dielectric function fit to reflectance measurements (Jasperse et al., 1966). Of the substrate materials presently available, this study determined MgO to be the best for this application because of its high transmittance in the far-infrared. The optical constants of $YBa_2Cu_3O_7$ at 8 K are determined using the dielectric function parameters recommended by Zhang et al. (1994). This frequency-dependent dielectric function is the sum of a high-frequency dielectric constant, a midinfrared absorption band accounting for electronic transitions, and a free-carrier contribution. The free-carrier contribution, which is a function of the free-carrier conductivity $\sigma(\omega)$ dominates the dielectric function in the infrared region. The free-carrier conductivity is modeled by two components: the BCS-theory-electron contribution $\sigma_{ss}(\omega)$, which is determined from the Zimmermann theory (Zimmermann et al., 1991) and the residual normal-state electron contribution $\sigma_{nr}(\omega)$, which is based on the Drude model. The free carrier conductivity is:

$$\sigma(\omega) = (1 - f_{nr})\sigma_{ss}(\omega) + f_{nr}\sigma_{nr}(\omega) \tag{8.1}$$

where f_{nr} is the temperature-independent fraction of residual normal-state electrons. Zhang et al. (1994) recommended $f_{nr} = 0.20$ for the best $YBa_2Cu_3O_7$ films and crystals currently available. It is assumed that there are no size effects on the optical constants of the films examined in this work.

8.2.3 Fabry-Pérot Resonator Performance Characteristics

Upon traversing the width t_c of the Fabry-Pérot cavity along the x direction, a monochromatic plane wave acquires a phase change δ given by:

$$\delta = \frac{\omega}{c_0} n_c t_c \tag{8.2}$$

where n_c is the refractive index of the cavity. For a nonabsorbing Fabry-Pérot resonator, the transmittance equals unity when $\delta = m_c \pi$, where m_c is a positive integer representing the order of the cavity resonance. When the resonator materials are absorbing, the maximum transmittance is less than unity and it occurs at a smaller frequency than that predicted by Eq. (8.2) for $\delta = m_c \pi$. However, for the $YBa_2Cu_3O_7$-on-MgO resonator, a good approximation of the maximum transmittance frequency ω_{max} is obtained by setting $\delta = m_c \pi$ (Yeh, 1988),

$$\omega_{max} \approx \frac{m_c \pi c_0}{n_c t_c} \tag{8.3}$$

For a cavity thickness $t_c = 100$ μm, Eq. (8.3) predicts a maximum transmittance at 50 cm^{-1} for the fundamental resonance. The maximum transmittance occurs at 48.6 cm^{-1} for a substrate thickness $t_s = 81.6$ μm and a film thickness $t_f = 0.01$ μm. As t_f increases, ω_{max} approaches 50 cm^{-1}.

The separation between the transmittance peaks is called the free spectral range. The peak half-width is the peak width at one-half of the maximum transmittance. The ratio of the free spectral range and the peak half-width is called the finesse $\mathfrak{I}$ of the fringes. It is a measure of the resolution of the device. As the reflectance of the cavity mirrors increases, $\mathfrak{I}$ increases.

8.3 Results and Discussion

The extinction coefficient of the MgO substrates is approximately zero for wavenumbers less than 350 cm^{-1}. In this spectral range, the substrates act as secondary resonator cavities. Figure 8.2 illustrates the strong influence of the substrate thickness t_s on the maximum transmittance τ_{max} of a resonator at 49.2 cm^{-1} for a film thickness t_f = 0.03 μm and t_c = 100 μm. As t_s changes, the wavenumber of the maximum transmittance remains around 50 cm^{-1} but the maximum transmittance oscillates between 0.03 and 0.41. Given the strong t_s-dependence of the transmittance, it would be difficult to construct a good scanning interferometer with this structure unless the parallelism of the substrates was substantially altered. To maximize the transmittance, the substrate must be treated as an antireflection coating. For maximum transmittance, t_s must satisfy (Yeh, 1988):

$$t_s = \frac{(2m_s + 1)}{n_s} \frac{\pi}{2} \frac{c_0}{\omega} \tag{8.4}$$

where m_s is a positive integer denoting the order of resonance in the substrates. For the optimal substrate thickness, ω in Eq. (8.1) is set equal to ω_{max}. Equations (8.3) and (8.4) are combined to relate the optimal t_s to t_c and m_c,

$$t_s = \frac{(2m_s + 1)}{2n_s} \frac{n_c t_c}{m_c} \tag{8.5}$$

The optimal substrate thicknesses for t_c = 100 μm and m_c = 1 are: t_s = 16.28 μm, 48.84 μm, 81.4 μm, etc. The thickness change Δt_s between the maximum and minimum transmittance is 16.28 μm. To investigate the sensitivity of the transmittance and finesse to changes in t_s, the optimal t_s values were varied by 5% of Δt_s, i.e., by ±0.81 μm. The variation did not significantly alter the transmittance of the structure. However, as t_c is decreased, shifting the fundamental transmittance peak to larger wavenumbers, Δt_s decreases and the thickness tolerance requirement for t_s increases.

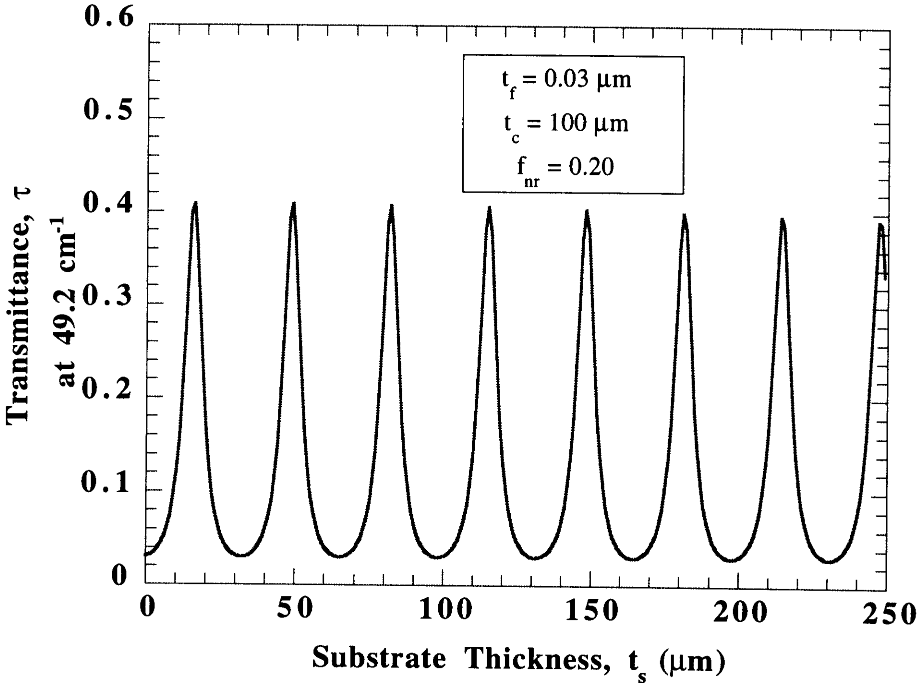

Figure 8.2 Influence of MgO substrate thickness on the Fabry-Pérot resonator maximum transmittance.

The largest $\tau_{\max}$ and $\Im$ are observed for the thinnest substrate $t_s = 16.28\ \mu m$, $m_s = 1$. As m_s is increased, there is a general decrease in the transmittance peak heights. The change in $\tau_{\max}$ at about $50\ cm^{-1}$ for $m_s = 2$ and 3 is small for film thicknesses greater than $0.02\ \mu m$. Results are presented here for $t_s = 81.4\ \mu m$, $m_s = 3$. The maximum transmittance and finesse decrease by about 5-10% from the thinnest substrate values. However, a substrate thickness of $16\ \mu m$ would be technically difficult to achieve, so the thicker substrate is used in the analysis.

As t_s is increased, the sidebands caused by resonance in the MgO substrates (Wiese et al., 1992) becomes noticeable. The sidebands are separated from the main resonance by a wavenumber interval of $(n_s\, t_s)^{-1}$. For thin substrates the separation is so large that the sidebands do not significantly influence the transmittance spectrum.

Figure 8.3 shows the behavior of $\tau_{\max}$ and $\Im$ around $50\ cm^{-1}$ with changing film thickness for $t_s = 81.4\ \mu m$, $t_c = 100$ mm, and $f_{nr} = 0.20$. The frequency of maximum transmittance varies slightly with t_f, occurring between $48.6\ cm^{-1}$ and $50\ cm^{-1}$. As t_f increases, the reflectance of the films increases, decreasing τ_{max} but increasing $\Im$. The best metal mesh structures have $\tau_{\max} \approx 0.5$ and $\Im \approx 120$ (Lang et al., 1989). Comparable performance is achieved when $t_f = 0.03\ \mu m$, where $\tau_{\max} \approx 0.42$ and $\Im \approx 90$. In general, optimal performance is achieved for $0.02\ \mu m < t_f < 0.05\ \mu m$. For $t_f < 0.02\ \mu m$, the absorptance of the film increases which adversely affects the performance of the resonator. For $t_f > 0.05\ \mu m$, the films become increasingly opaque, reducing the maximum transmittance.

Figure 8.4 shows the transmittance spectrum of the optimized structure, with $t_f = 0.03\ \mu m$. The finesse decreases sharply for $m_c > 2$ because the film reflectance decreases. Sidebands begin to disturb the transmittance spectrum for wavenumbers greater than $150\ cm^{-1}$. For $t_s = 16.28\ \mu m$, the sidebands are much less noticeable.

Wiese et al. (1992) obtained a maximum transmittance of approximately 0.15 and a finesse of approximately 55 for the fundamental resonance at $80\ cm^{-1}$ of a Fabry-Pérot structure with

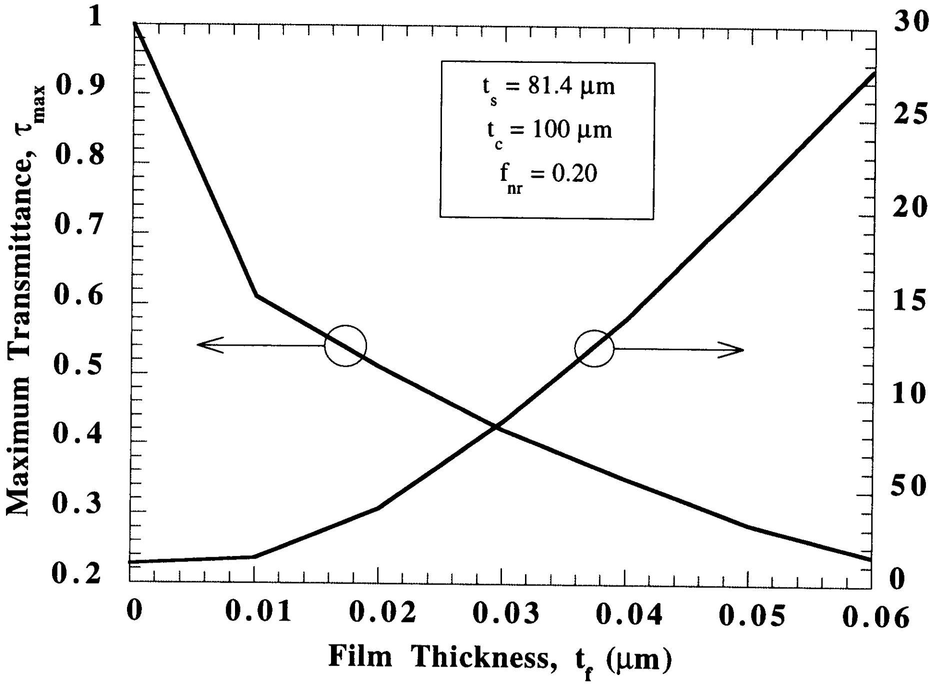

Figure 8.3 Maximum transmittance and finesse of a $YBa_2Cu_3O_7$-on-MgO Fabry-Pérot resonator at 8 K and 49.3 cm^{-1} ±0.7 cm^{-1} for f_{nr} = 0.20.

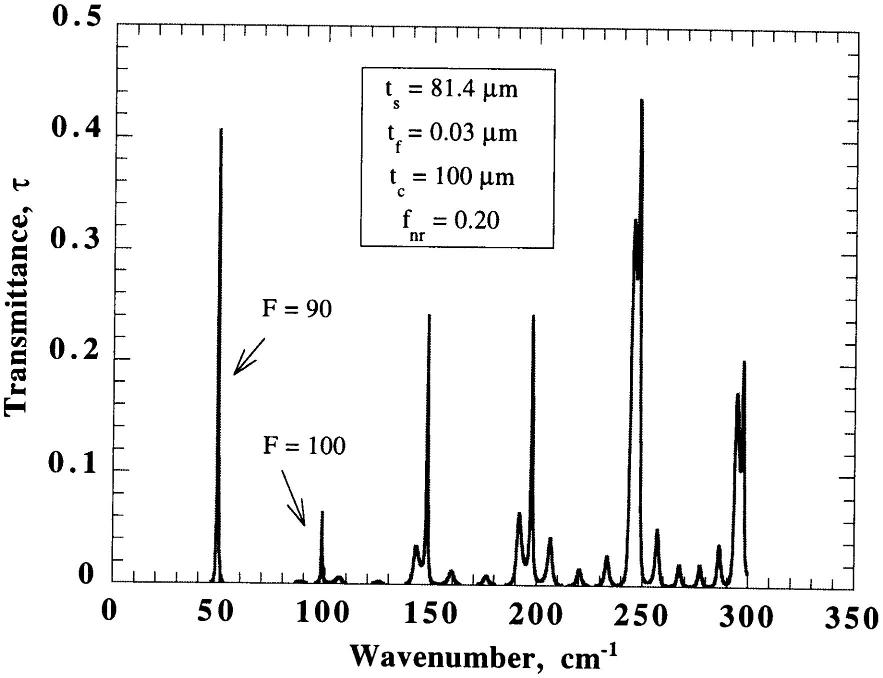

Figure 8.4 YBa$_2$Cu$_3$O$_7$-on-MgO Fabry-Pérot resonator transmittance at 8 K.

$t_c \approx 62.5$ μm, $t_f \approx 0.07$ μm, and unequal substrate thicknesses of 350 μm and 250 μm. When the substrate and film thicknesses are adjusted as recommended in this study, i.e., $t_s = 50.75$ μm ($m_s = 3$) and $t_f = 0.05$ μm, the maximum transmittance increases to approximately 0.37 and the finesse increases to approximately 100 for the same cavity width.

It has been postulated (Zhang et al., 1994) that further improvements in the quality of $YBa_2Cu_3O_7$ films could reduce the fraction of residual normal-state electrons. Figure 8.5 shows the behavior of τ_{max} and $\Im$ with changing film thickness for the same parameters in Fig. 8.3 for frequencies near 50 cm^{-1}, except f_{nr} is changed to 0.05, corresponding to much-improved $YBa_2Cu_3O_7$. The finesse and maximum transmittance increase dramatically as the absorptance losses in the films decrease. For $t_f = 0.04$ μm, $\Im \approx 260$ and $\tau_{max} \approx 0.72$. This performance would represent a major improvement for far-infrared Fabry-Pérot resonators.

8.4 Conclusions

1. The substrate thickness strongly influences the transmittance of the $YBa_2Cu_3O_7$ on MgO Fabry-Pérot resonator.

2. The peak transmittance and finesse of $YBa_2Cu_3O_7$ on MgO Fabry-Pérot resonators fabricated from the best $YBa_2Cu_3O_7$ material available are comparable with that of the best metal mesh resonators in the far-infrared spectral region.

3. A reduction of the fraction of residual normal-state electrons in $YBa_2Cu_3O_7$ films will permit the construction of far-infrared Fabry-Pérot resonators, superior to any existing device.

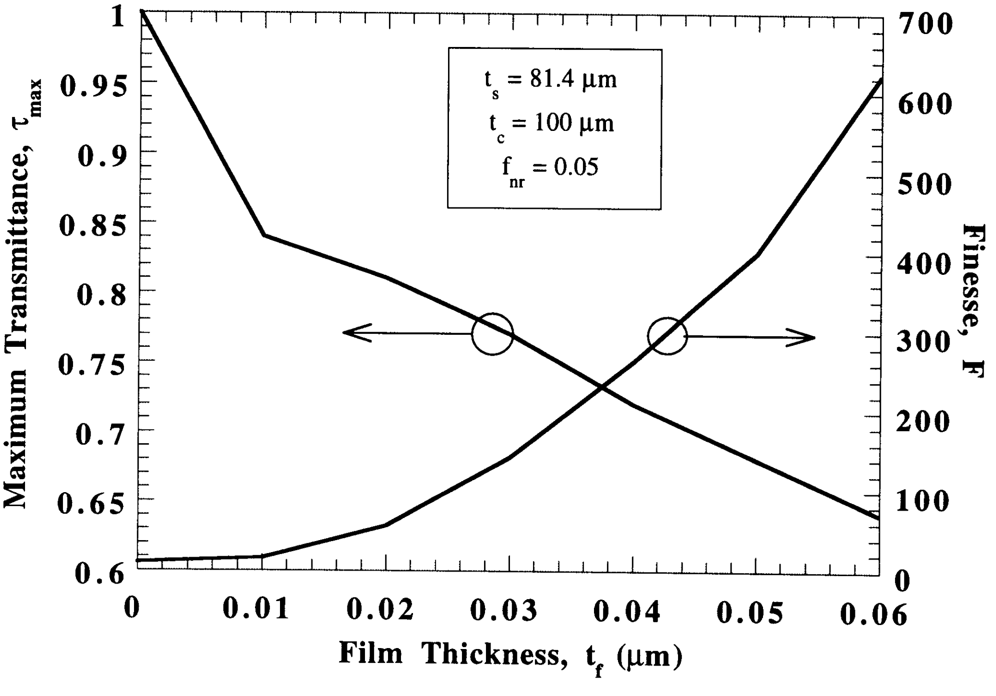

Figure 8.5 Maximum transmittance and finesse of a $YBa_2Cu_3O_7$-on-MgO Fabry-Pérot resonator at 8 K and 49.3 cm^{-1} ±0.7 cm^{-1} for $f_{nr} = 0.05$.

CHAPTER 9

SUMMARY AND FUTURE WORK

9.1 Summary

This work investigates the reflection Fabry-Pérot etalon technique as a method for accurately measuring the absorptance of films of gold and $YBa_2Cu_3O_7$ at room-temperature and 6 K. Radiation shielding and Fabry-Pérot etalons fabricated from $YBa_2Cu_3O_7$ are also analyzed.

Thin-film optics is used to extract the radiative properties of the sample layer from a silicon-on-sample reflection Fabry-Pérot etalon. The errors introduced by air gaps between the silicon and the sample, surface roughness, deviation from parallelism, and non-collimated radiation are examined. Based on this analysis, the predictions made by thin-film optics agree well with experimental results.

A method for extracting meaningful radiative property data from distorted reflection Fabry-Pérot etalon reflectance data is presented. The single-beam spectra for the etalon for metallic systems contains sufficient information to eliminate the need to perform a reference measurement.

The optical constants of the 127 μm-thick silicon used in this work are determined using reflectance and transmittance measured using an FT-IR for the spectral range from 400 to

100 cm^{-1}. For the first time, experimental data are presented which resolves a disagreement in the literature over the value of the absorption coefficient for this spectral range. The absorption coefficient is found to be 0.20 cm^{-1} for 33.5 Ω-cm silicon.

The anomalous skin effect with diffuse electron scattering provides the most accurate prediction of the radiative properties of gold at room temperature and liquid-helium temperature. At room temperature, the discrepancy between the experimental data and the Drude model prediction is small. Given the relative simplicity of this model, it is recommended for room-temperature predictions. The Drude model is not appropriate for predicting liquid-helium temperature radiative properties. The diffuse reflection anomalous skin effect prediction agrees closely with the radiative property measurements across infrared spectral range.

Absorptance data measured at 6 K are presented for two $YBa_2Cu_3O_7$ samples for the spectral range from 420 to ~80 cm^{-1}. These data compare well with the limited set of high-accuracy absorptance data available for this material. A predictive model based on the Zimmermann theory for the BCS free-electron conductivity is developed using the data presented here. The data cannot be accurately represented without employing multiple energy gaps within the model.

An analysis of the radiative heat flux between two surfaces of $YBa_2Cu_3O_7$ reveals that the heat flux is reduced by as much as 90% when compared to a similar system consisting of two surfaces of gold. Considering the strong optical anisotropy of the material changed the heat flux prediction by less than 5% compared with a prediction performed using the *ab*-plane optical constants for the *c*-axis.

A prediction of the performance of a $YBa_2Cu_3O_7$-based Fabry-Pérot resonator shows that MgO is the best choice for a substrate material as it has the highest transparency of any $YBa_2Cu_3O_7$ substrate material. The prediction shows that the peak transmittance and finesse of $YBa_2Cu_3O_7$ on MgO Fabry-Pérot resonators fabricated from the best $YBa_2Cu_3O_7$ material available are comparable with that of the best metal mesh resonators in the far-infrared spectral region, and potentially superior with improvements in material quality.

9.2 Future Work

The reflection Fabry-Pérot etalon offers a relatively simple method for the accurate measurement of the far-infrared radiative properties of metallic and superconducting films. Few metals have been characterized in the spectral range accessible with this technique. A comparison of the absorptance of metals prepared with different deposition conditions using this technique could provide insights into optimal film growth conditions. Absorptance data for a range of metals prepared under different deposition conditions could lead to improved predictive models for these properties.

An experimental investigation of the influence of oxygen depletion on the absorptance of $YBa_2Cu_3O_7$ films might lead to an explanation for the discrepancy between the data presented here and previous work. Applying this technique to films of $Bi_2Sr_2CaCu_2O_8$, for which the superconducting energy gap has been unambiguously identified from other experimental techniques would also be instructive.

There is now a significant amount of high-accuracy data for the radiative properties of $YBa_2Cu_3O_7$. Applying recently developed d-wave-based theories for the infrared conductivity of high-T_c materials to these data might lead to a more satisfying predictive model with fewer fitting parameters.

APPENDIX A

REFLECTANCE AND TRANSMITTANCE OF A MULTILAYER THIN-FILM STACK

Thin film optics is a method for predicting the directional-hemispherical spectral reflectance and the spectral directional transmittance of an electromagnetic wave propagating through a multilayer thin film stack for a particular wavelength and angle of incidence (Yeh, 1988). The method accounts for interference effects within the layers caused by the multiple reflections between the layer interfaces. The main assumptions of the thin film optics are:

- The surface of the stack, and all the film interfaces are optically smooth, with no air gaps. The interface is deemed optically smooth if the rms roughness of the surface is much less than the wavelength of the electromagnetic radiation.
- The interfaces between the films are parallel.
- The planar dimensions of the sample are much larger than the wavelength.
- The complex refractive indices of each layer are constant in the direction perpendicular to the interface.

In this presentation, thin film optics are used in the form of the 2 x 2 matrix method of multilayers outlined by Yeh (1988). This method provides a systematic approach for determining the reflectance and transmittance of a stack with any number of layers. The matrix method is particularly well suited for implementation in a computer program. This presentation additionally assumes the layers are optically isotropic, i.e., the optical constants are not dependent on crystallographic direction.

A generic multilayer stack is shown in Fig. A.1. There are N layer interfaces and N+1 layers, *including* the unbounded transparent media on each side of the actual stack, layers 1 and N+1. Light is incident on interface 1, with an angle of incidence θ_1. A_N and B_N are the amplitudes of the forward and backward propagating electric field vectors on the left side of interface N. Amplitudes on the right side of interface N are indicated by the prime notation on A'_{N+1} and B'_{N+1}. The central equation of the multilayer theory relates the amplitudes on the left side of interface 1 with those on the right side of interface N:

$$\begin{pmatrix} A_1 \\ B_1 \end{pmatrix} = \left[\prod_{i=1}^{N} P_i D_i^{-1} D_{i+1}\right] \begin{bmatrix} A'_{N+1} \\ B'_{N+1} \end{bmatrix} = \begin{bmatrix} m_{11} & m_{12} \\ m_{21} & m_{22} \end{bmatrix} \begin{bmatrix} A'_{N+1} \\ B'_{N+1} \end{bmatrix} \qquad \text{(A.1)}$$

where P_i is the propagation matrix, D_i is the dynamical matrix, and m_{ij} is an element of the transfer function matrix. The propagation matrix accounts for the effect of absorption and interference within a layer i bounded by two interfaces. Because layer 1 is not bound by two interfaces, the propagation matrix has no meaning, and P_1 is set equal to the identity matrix. For layers 2, 3,..., N, the propagation matrix is:

$$P_i = \begin{bmatrix} e^{i\phi_i} & 0 \\ 0 & e^{-i\phi_i} \end{bmatrix} \qquad \text{(A.2)}$$

where $\phi_i = 2\pi \bar{n}_i d_i \cos\bar{\theta}_i / \lambda$ is the phase shift. The complex refractive index is $\bar{n}_i = n_i + i\kappa_i$, where n_i is the refractive index and κ_i is the extinction coefficient. This presentation assumes that the bounding media are non-absorbing, with refractive indices of n_1 and n_{N+1}, respectively. The

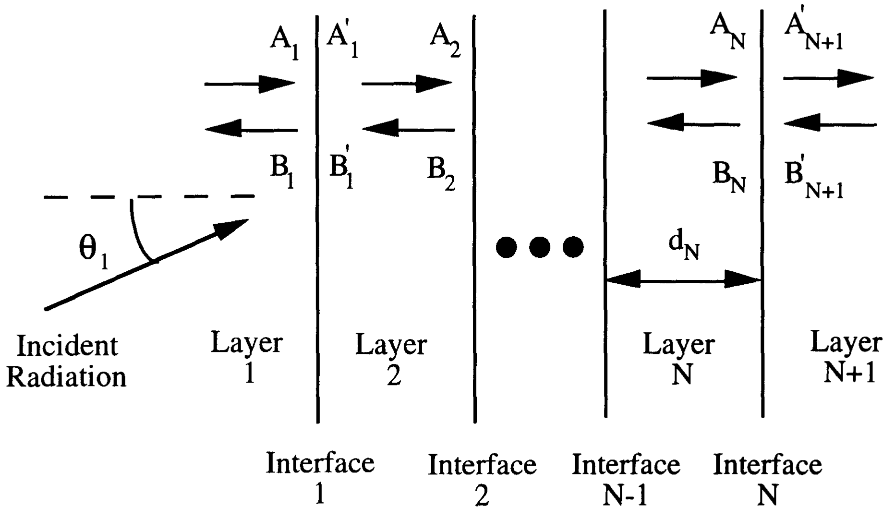

Figure A.1 A schematic of a general multilayer.

thickness of layer i is d_i, $\overline{\theta}_i$ is the complex angle of refraction, and λ is the wavelength of the incident wave in vacuum.

The dynamical matrix accounts for reflection and refraction at the interface i, relating amplitudes of the reflected and refracted waves on either side of the interface. Depending on the state of polarization of the wave, the dynamical matrix is given by:

$$D_{\mathrm{i,s-wave}} = \begin{pmatrix} 1 & 1 \\ \overline{n}_\mathrm{i}\cos\overline{\theta}_\mathrm{i} & -\overline{n}_\mathrm{i}\cos\overline{\theta}_\mathrm{i} \end{pmatrix} \tag{A.3}$$

$$D_{\mathrm{i,p\,wave}} = \begin{pmatrix} \cos\overline{\theta}_\mathrm{i} & \cos\overline{\theta}_\mathrm{i} \\ \overline{n}_\mathrm{i} & -\overline{n}_\mathrm{i} \end{pmatrix} \tag{A.4}$$

where s and p indicate that the electric field vector is perpendicular and parallel to the plane of incidence, respectively.

For non-absorbing layers, the angle of refraction is real and equal to the direction of propagation in the layer. Absorbing layers have complex refractive indices, so they have complex angles which have no direct physical interpretation. Given the angle of incidence in medium 1, the complex angles for the other layers are calculated in succession using Snell's law,

$$\sin\overline{\theta}_{\mathrm{i+1}} = \frac{\overline{n}_\mathrm{i}}{\overline{n}_{\mathrm{i+1}}}\sin\overline{\theta}_\mathrm{i} \tag{A.5}$$

The reflectance of an s- or p-wave for the whole stack is the ratio of the intensities of the forward and backward propagating waves on the left side of interface 1. The transmittance of an s- or p-wave is the ratio of the intensities of the forward propagating wave on the right side of interface N and the forward propagating wave on the left side of interface 1. The intensity of an electromagnetic wave is proportional to the square of its amplitude,

$$R'_{\mathrm{s/p}} = \frac{B_1}{A_1} = \left|\frac{m_{21}}{m_{11}}\right|^2 \tag{A.6}$$

$$T'_{\mathrm{s/p}} = \frac{n_{\mathrm{N+1}}\cos\theta_{\mathrm{N+1}}}{n_1\cos\theta_1}\frac{A'_{\mathrm{N+1}}}{A_1} = \frac{n_{\mathrm{N+1}}\cos\theta_{\mathrm{N+1}}}{n_1\cos\theta_1}\left|\frac{m_{21}}{m_{11}}\right|^2 \tag{A.7}$$

where $R'_{s/p}$ is the reflectance and $T'_{s/p}$ is the transmittance for the *s*- or *p*-polarization. Thermal radiation is usually well approximated as unpolarized, in which case, the spectral directional reflectance and transmittance, R'_λ and T'_λ, may be calculated as a simple arithmetic average of the *s*- and *p*-wave properties (Siegel and Howell, 1992). For normal incidence, the *s*- and *p*-wave reflectances are equal. The subscripts λ and prime indicate a spectral and directional property, respectively, for precisely one wavelength.

Spectroscopic instruments cannot measure radiative properties at one exact wavelength, but average these properties over some finite spectral interval $\Delta\lambda$. To calculate the properties that would be measured experimentally, one must integrate over this spectral interval (Yeh, 1988). For example, the directional-hemispherical spectral reflectance would be calculated by:

$$R'_{\lambda,\Delta\lambda} = \frac{1}{\Delta\lambda} \int_{\lambda-\Delta\lambda/2}^{\lambda+\Delta\lambda/2} R'_\lambda \, d\lambda \tag{A.8}$$

The expression for the spectral directional transmittance is analogous. Implementing the theory in this way makes it general in that predicted properties do not depend on classifying the radiation in a layer as coherent, incoherent, or partially coherent (Chen and Tien, 1992).

The spectral directional absorptance is calculated by subtracting the reflectance and transmittance from unity, and the spectral directional emittance is calculated by invoking Kirchhoff's law:

$$\alpha'_\lambda = \varepsilon'_\lambda = 1 - R'_\lambda - T'_\lambda \tag{A.9}$$

where α'_λ and ε'_λ are the spectral directional absorptance and emittance, respectively. Kirchhoff's law is valid for the spectral properties if the emitting object is in local thermodynamic equilibrium, i.e., it can be characterized by a single temperature (Malone et al., 1993). If there is a significant temperature gradient in the part of the stack that is emitting, or if the phonons and electrons are not in thermal equilibrium (e.g., laser annealing), then Kirchhoff's law is invalid.

REFERENCES

Afsar, M.N. and Hasted, J.B., 1978, 'Submillimetre Wave Measurements of Optical Constants of Water at Various Temperatures,' *Infrared Physics*, Vol. 18, pp. 835-841.

Annett, J.F., Goldenfeld, N., and Renn, S.R., 1990, 'The Pairing State of $YBa_2Cu_3O_{7-\delta}$,' in *Physical Properties of High-Temperature Superconductors II*, D.M. Ginsberg, Ed., World Scientific Publishing Co., Singapore, pp. 571-685.

Ashcroft, N.W., and Mermin, N.D., 1976, *Solid State Physics*, Holt, Rinehart, Philadelphia.

Baltes, H.P., 1976, 'On the Validity of Kirchhoff's Law of Heat Radiation for a Body in a Nonequilibrium Environment,' *Progress in Optics*, Vol. 13, pp. 1-25.

Bardeen, J., Cooper, L.N., and Schrieffer, J.R., 1957, 'Theory of Superconductivity,' *Physical Review*, Vol. 108, pp. 1175-1204.

Bauer, M., 1990, 'Untersuchungen an Hochtemperatursupraleitern von Typ $YBa_2Cu_3O_{7-\delta}$ Mit Hilfe der Infrarot-Spektroskopie,' Dissertation, Universität Tübingen, Tübingen, Germany.

Beach, R.T., and Christy, R.W., 1977, 'Electron-Electron Scattering in the Intraband Optical Conductivity of Cu, Ag and Au,' *Physical Review B*, Vol. 16, pp. 5277-5284.

Beckmann, P., and Spizzichino, A., 1977, *The Scattering of Electromagnetic Waves from Rough Surfaces*, Artech House, Norwood, MA.

Bednortz, J.G. and Müller, K.A., 1986, 'Possible High T_c Superconductivity in the Ba-La-CuO System,' *Zeitschrift für Physik B*, Vol. 64, pp. 189-93.

Bennett, H.E., and Bennett, J.M., 1967, 'Precision Measurements in Thin Film Optics,' in *Physics of Thin Films*, G. Hass and R.E. Thun, Eds., Vol. 14, Academic Press, New York, pp. 1-96.

Bennett, H.E., and Koehler, W.F., 1960, 'Precision Measurement of Absolute Specular Reflectance with Minimized Systematic Errors,' *Journal of the Optical Society of America*, Vol. 50, pp. 1-6.

Bennett, J. M., 1995, 'Polarization,' in *Handbook of Optics*, McGraw-Hill, New York, pp. 5-1 to 5-28.

Bennett, J.M., and Ashley, E.J., 1965, 'Infrared Reflectance and Emittance of Silver and Gold Evaporated in Ultrahigh Vacuum,' *Applied Optics*, Vol. 4, pp. 221-224.

Bergman , T.G., 1970, *Reflectivity of Silver and Gold as a Function of Temperature at Four Micron Wavelength*, Naval Weapons Center Technical Publication # 5043 (NWC TP 5043), China Lake, CA.

Birch, J.R., 1978, 'The Absolute Determination of Complex Reflectivity,' *Infrared Physics*, Vol. 18, pp. 613-620.

Born, M., and Wolf, E., 1980, *Principles of Optics Electromagnetic Theory of Propagation, Interference and Diffraction of Light*, Sixth Edition (with corrections), Pergamon Press, Oxford, UK.

Bozovic, I., Kim, J.H., Harris, Jr., J.H., Hellman, E.S., Hartford, E.H., and Chan, P.K., 1992, "Free-Charge-Carrier Plasmons in $Ba_{1-x}K_xBiO_3$: A Close Relation to Cuprate Superconductors," *Physical Review B*, Vol. 46, pp. 1182-1186.

Bozovic, I.,1990, 'Plasmons in Cuprate Superconductors,' *Physical Review B*, Vol. 42, pp. 1969-1984.

Brandli, G. and Sievers, A.J., 1971, 'Absolute Measurement of the Far-Infrared Surface Resistance of Pb,' *Physical Review B*, Vol. 5, pp. 3550-3557.

Brewster, M.Q., 1992, *Thermal Radiative Transfer and Properties*, John Wiley & Sons, New York.

Burns, G., 1990, *Solid State Physics*, Academic Press, Boston.

Caren, R.P., 1974, 'Thermal Radiation between Closely Spaced Metal Surfaces at Low Temperatures Due to Traveling and Quasi-stationary Components of the Radiation Field,' *International Journal of Heat and Mass Transfer*, Vol. 17, pp. 755-765.

Chen, G., and Tien, C.L., 1992, 'Partial Coherence of Thin Film Radiative Properties,' *Journal of Heat. Transfer*, Vol. 114, p. 636-43.

Collins, J.G., 1958, 'The Theory of the Anomalous Skin Effect in Metals for Obliquely Incident Radiation,' *Applied Science Research*, Vol. B7, pp. 1-40.

Cox, D.L., and Maple, M.B., 1995, 'Electronic Pairing in Exotic Superconductors,' *Physics Today*, Vol. 48, No. 2, pp. 32-40.

Cunsolo S., Dore, P., Lupi, S., Trippetti, R., Varsamis, C.P., and Sherman, A., 'Infrared Conductivity of YBCO from Transmission and Reflection Spectra of Thin Films,' *Physica C*, Vol. 211, pp. 22-28.

Dingle, R.B., 1953, 'The Anomalous Skin Effect and the Reflectivity of Metals. I,' *Physica*, Vol. 19, pp. 311-347.

Domoto, G.A., Boehm, R.F., and Tien, C.L., 1969, 'Prediction of the Total Emissivity of Metals at Cryogenic Temperatures,' *Advances in Cryogenic Engineering,* Vol. 14, pp. 230-239.

Domoto, G.A. and Tien, C.L., 1970, 'Thick Film Analysis of Radiation Transfer between Parallel Metallic Surfaces,' *Journal of Heat Transfer*, Vol. 92, pp. 399-404.

Edwards, D.F., 1985, 'Silicon (Si),' in *Handbook of Optical Constants of Solids*, E. Palik, Ed., Academic Press, New York, pp. 547-569.

Fiory, A.T., Hebard, A.F., Eick, R.H., Mankiewich, P.M., Howard, R.E., O'Malley, M.L., 1990, 'Metallic and Superconducting Surfaces of $YBa_2Cu_3O_7$Probed by Electrostatic Charge Modulation of Epitaxial Films,' *Physical Review Letters*, Vol. 65, pp. 3441-3444.

Flik, M.I., Choi, B.I., Anderson, A.C., and Westerheim, A.C., 1992, 'Thermal Analysis and Control for Sputtering Deposition of High-T_c Superconducting Films,' *Journal of Heat Transfer*, Vol. 114, pp. 255-263.

Flik, M.I., Zhang, Z.M., Goodson, K.E., Siegal, M.P., and Phillips, J.M., 1992, 'The Electron Scattering Rate in Epitaxial $YBa_2Cu_3O_7$ Superconducting Films,' *Physical Review B.*, Vol. 46, pp. 5606-5614.

Fuchs, K., 1938, 'The Conductivity of Thin Metallic Films According to the Electron Theory of Metals,' *Proceedings of the Cambridge Philosophical Society*, Vol. 34, pp. 100-108.

Gammel, P., Bishop, D.J., Dolan, G.J., Kwo, J.R., Murray, C.A., Schneermeyer, L.F., Waszczak, J.V., 1987, 'Observation of Hexagonally Corrected Flux Quanta in $YBa_2Cu_3O_7$,' *Physical Review Letters*, Vol. 59, pp. 2592-2595.

Gatesman, A.J., Giles, R.H., and Waldman, J., 1995, 'High-Precision Reflectometer for Submillimeter Wavelengths,' *Journal of the Optical Society of America B (Optical Physics)*, Vol. 12, pp. 212-219.

Genzel, L., 1991, 'Fourier Transform Spectroscopy for High-T_c Superconductors,' *Proceedings of the 8th International Conference on Fourier Transform Spectroscopy*, Travemünde, Germany, H.M. Heise, E.H. Korte, H.W. Siesler, Eds., SPIE, Vol. 1575, pp. 2-10.

Genzel, L., Barth, K.-L., and Keilmann, F., 1990, 'Precise Determination of High Metallic Reflection in the Far-Infrared: the Reflection-Fabry-Pérot,' *International Journal of Infrared & Millimeter Waves*, Vol. 11, pp. 1133-1161.

Genzel, L., Bauer, M., Habermeier, H.-U., Brandt, E.H., 1993, 'Determination of the Gap Distribution in $YBa_2Cu_3O_7$ Using a Far-Infrared Reflection-Fabry-Pérot Device,' *Zeitschrift für Physik B*, Vol. 90, pp. 3-12.

Genzel, L., Wittlin, A., Bauer, M., Cardona, M., Schönherr, and Simon, A., 1989, 'Phonon Anomalies and Range of Superconducting Energy Gaps from Infrared Studies of $YBa_2Cu_3O_{7-\delta}$,' *Physical Review B*, Vol. 40, pp. 2170-2178.

Goodson, K.E., and Flik, M.I., 1993, 'Electron and Phonon Thermal Conduction in Epitaxial High-Tc Superconducting Films,' *Journal of Heat Transfer*, Vol. 115, pp. 17-25.

Gough, C.E., Colclough, M.S., Forgan, E.M., Jordan, R.G., Keene, M., Muirhead, C.M., Rae, A.I.M., Thomas, N., Abell, J.S., Sutton, S., 1987, 'Flux Quantization in a High-T_c Superconductor,' *Nature*, Vol. 326, p. 855.

Griffiths, P.R., and de Haseth, J.A., 1986, *Fourier Transform Infrared Spectroscopy*, John Wiley & Sons, New York.

Grischkowsky, D., Keiding, S., van Exter, M., and Fattinger, Ch., 1990, 'Far-Infrared Time-Domain Spectroscopy with Terahertz Beams of Dielectrics and Semiconductors,' *Journal of the Optical Society of America B (Optical Physics)*, Vol. 7, pp. 2006-2015.

Guenther, R.D., 1990, *Modern Optics*, John Wiley & Sons, New York.

Gurzhi, R.N.,1958, 'On the Theory of the Infrared Absorptivity of Metals,' *Soviet Physics JETP*, Vol. 6, pp. 506-512.

Hadni, A., Gerbaux, X., Cudraz, H.M., Tazawa, M., Mage, J.C., Marcilhac, B., Mercandalli, L., and Mansart, D., 1995, 'Residual Losses of Superconducting Thin Films of $YBa_2Cu_3O_{7-\delta}$ in the Far Infrared and Microwaves: Applications,' *Physica C*, Vol. 245, pp. 219-230.

Hardy, W.N., Bonn, D.A., Morgan, D.C., Ruixing Liang, Kuan Zhang, 1993,'Precision Measurements of the Temperature Dependence of λ in $YBa_2Cu_3O_{6.95}$,' *Physical Review Letters*, Vol. 71, pp. 2134-2137.

Harshmann, D.R., Schneemeyer, L.F., Waszczak, J.V., Aeppli, G., Cava, R.J., Batlogg, B., Rupp, L.W., Ansaldo, E.J., Williams, D.L., 1989, 'Magnetic Penetration Depth in Single-Crystal $YBa_2Cu_3O_{7-\delta}$,' *Physical Review B*, Vol. 39, pp. 851-854.

Hass and Hadley, 1963, 'Optical Properties of Metals,' in *American Institute of Physics Handbook*, Second Edition, D.E. Gray, Ed., McGraw-Hill, New York, pp. 6-119.

Hebb, J.P., Cravalho, E.G., and Flik, M.I., 1993, 'Thermal Radiation Absorption in Doped Semiconductors Due to Direct Intersubband Transitions,' *Journal of Heat Transfer*, Vol. 117, pp. 948-954.

Hecht, E., and Zajac, A., 1974, *Optics*, Addison-Wesley Publishing Co., New York.

Hernandez, G., 1986, *Fabry-Pérot Interferometers*, Cambridge University Press, Cambridge, U.K.

Holden, J., 1949, 'Multiple-Beam Interferometry: Intensity Distribution in the Reflected System', *Proceeding of the Physical Society*, Vol. 62, pp. 405-417.

Holstein, T., 1954, 'Optical and Infrared Volume Absorptivity of Metals,' *Physical Review*, Vol. 96, pp. 535-536.

Imer, J.-M., 1989, 'High-Resolution Photoemission Study of the Low-Energy Excitations Reflecting the Superconducting State of a Bi-Sr-Ca-Cu-O Single Crystal,' *Physical Review Letters*, Vol. 62, pp. 336-9.

Iye, Y., 1992, 'Transport Properties of High T_c Cuprates,' in *Physical Properties of High-Temperature Superconductors III*, D.M. Ginsberg, Ed., World Scientific Publishing Co., Singapore, pp. 285-361.

Jasperse, J.R., Kahan, A., Plendl, J.N., and Mitra, S.S., 1966, 'Temperature Dependence of Infrared Dispersion in Ionic Crystals LiF and MgO,' *Physical Review*, Vol. 146, pp. 526-542.

Johnson, F.A., 1959, 'Lattice Absorption Bands in Silicon,' *Proceedings of the Physical Society*, Vol. 73, pp. 265-272.

Kamaras, K., Herr, S.L., Porter, C.D., Tache, N., Tanner, D.B., Etemad, S., Venkatesan, T., Chase, E., Inam, A., Wu, X.D., Hegde, M.S., Dutta, B., 1990,'In a Clean High-T_c Superconductor You Do Not See the Gap,' *Physical Review Letters*, Vol. 64, pp. 84-87.

Khoshenevisan, M., Pratt, W.P., Jr., Schroeder, P.A., Steenwyk, S.D., 1979, 'Low-Temperature Resistivity and Thermoelectric Ratio of Copper and Gold,' *Physical Review B*, Vol. 19, pp. 3873-3878.

Kimmitt, M.F., 1970, *Far-Infrared Techniques*, Pion, London.

Kirtley, J.R., and Tsuei, C.C., 1996, 'Probing High-Temperature Superconductivity,' *Scientific American*, Vol. 275, No. 2, pp. 68-73.

Kittel, C., 1976, *Introduction to Solid State Physics, Fifth Edition*, Wiley & Sons, New York.

Kobayashi, Y., and Imai, T.,1991, 'Phenomenological Description of Conduction Mechanism of High-T_c Superconductors by Three-Fluid Model,' *IEICE Transactions*, Vol. E74, pp. 1986-1992.

Koch, B., Dürrler, M., Geserich, H.P., Wolf, Th., Roth, G., and Zachmann, G., 1990, 'Optical Investigation of the Superconducting Phase Transition in $YBa_2Cu_3O_7$ Crystals,' in *Electronic Properties of High-T_c Superconductors and Related Compounds*, H. Kuzmany et al., Eds., Springer Series in Solid-State Sciences, Vol. 99, Springer-Verlag, Berlin, pp. 290-293.

Lang, P.T., Sessler, F., Werling, U., and Renk, K.F., 1989, 'Generation of Widely Tunable Intense Far-Infrared Radiation Pulses by Stimulated Raman Transitions in Methylfluoride Gas,' *Applied Physics Letters*, Vol. 55, pp. 2576-2578.

Lee, W., Rainer, D., and Zimmermann, W., 1989, 'Holstein Effect in the Far-Infrared Conductivity of High T_c Superconductors,' *Physcia C*, Vol. 159, pp. 535-544.

Leung, E.M.W., Fast, R.W., Hart, R.W., and Heim, J.R., 1979, 'Techniques for Reducing Radiative Heat Transfer between 77K and 4.2K,' *Advances in Cryogenic Engineering*, Vol. 25, pp. 489-499.

Liu, R., Thomsen, C., Kress, W., Cardona, M., Gegenheimer, B., de Wette, F.W., Prade, J., Kulkarni, A.D., and Schröder, U., 1988, 'Frequencies, Eigenvectors, and Single-Crystal Selection Rules of k = 0 Phonons in $YBa_2Cu_3O_{7-\delta}$: Theory and Experiment,' *Physical Review B*, Vol. 37, pp. 7971-7974.

Lobo, R.P.S.M., Gervais, F., Champeaux, C., Marchet, P., and Catherinot, A., 1995, 'Unexpected Behavior of IR Reflectivity of a $YBa_2Cu_3O_{7-\delta}$ Oriented Film,' *Material Science and Engineering B*, Vol. 34, pp. 74-79.

Loewenstein, E.V., Smith, D.R., and Morgan, R.L., 1973, Optical Constants of Far Infrared Materials. 2: Crystalline Solids,' *Applied Optics*, Vol. 12, pp. 398-406.

MacDonald, D.K.C., 1956, 'Electrical Conductivity of Metals and Alloys at Low Temperatures,' in *Handbuch der Physik*, Vol. 14, pp. 137-197.

Malone, C.G., Choi, B.I., Flik, M.I., Cravalho, E.G., 1993, 'Spectral Emissivity of Optically Anisotropic Solid Media,' *Journal of Heat Transfer*, Vol. 115, pp. 1021-1028.

Mattis, D.C., and Bardeen, J., 1958, 'Theory of the Anomalous Skin Effect in Normal and Superconducting Metals, ' *Physical Review*, Vol. 111, pp. 412-417.

McBride, D.M., Malone, C.G., Hebb, J.P., Cravalho, E.G., 1997,'The Effect of Temperature Variation on FT-IR Spectrometer Stability,' *Applied Spectroscopy*, Vol. 51, pp. 43-50.

McKay, J.A., and Rayne, J.A., 1976, 'Temperature Dependence of the Infrared Absorptivity of the Nobel Metals,' *Physical Review B*, Vol. 13, pp. 673-685.

Mendelssohn, K., 1960, *Cryophysics*, Interscience Publishers Inc., New York.

Miller, D., Richards, P.L., Etemad, S., Inam, A., Venkatesan, T., Dutta, B., Wu, X.D., Eom, C.B., Geballe, T.H., Newman, N., Cole, B.F., 1993, 'Correspondence Between Microwave and Submillimeter Absorptivity in Epitaxial Thin Films of $YBa_2Cu_3O_7$', *Physical Review B*, Vol. 47, pp. 8076-8088.

Moore, J.H., Davis, C.C., and Coplan, M.A., 1989, *Building Scientific Apparatus: A Practical Guide to Design and Construction*, Second Edition, Addison-Wesley Publishing Co., New York.

Motulevich, G.P., and Shubin, A.A., 1965, 'Influence of the Fermi Surface Shape in Gold on the Optical Constants and Hall Effect,' *Soviet Physics JETP*, Vol. 20, pp. 560-564.

Muller, R.H., 1969, 'Definitions and Conventions in Ellipsometry, *Surface Science*, Vol. 16, pp. 14-33.

Norman, M.R., 1993, 'After Seven Years, Where's the Consensus ?,' *Journal of the Physics and Chemistry of Solids*, Vol. 54, pp. 1165-1168.

Ohba, Tetsuhiko, and Ikawa, Shun-ichi, 1988, 'Far-Infrared Absorption of Silicon Crystals,' *Journal of Applied Physics*, Vol. 64, pp. 4141-4143.

Orlando, T.P., and Delin, K.A., 1991, *Foundations of Applied Superconductivity*, Addison-Wesley Publishing Co., Reading, MA.

Ose, W.,1990, Dissertation, Universität Regensburg, Regensburg, Germany.

Padalka,V.G., and Shklyarevskii, I.N., 1961, 'Determination of the Microcharacteristics of Silver and Gold from the Infrared Optical Constants and the Conductivity at 82 and 295 K,' *Optika i Spektroskopiia*, Vol. 11, pp. 285-288.

Parkins, G.R.,1978, 'Intraband Optical Conductivity $\sigma(\omega, T)$ of Cu, Ag and Au,' Ph.D. Thesis, Dartmouth College, Hanover, NH.

Pham, T., Lee, M.W., Drew, H.D., Welp, U., Fang, Y., 1991, 'Far-Infrared Absorptivity of Single-Domain $YBa_2Cu_3O_{7-x}$,' *Physical Review B*, Vol. 44, pp. 5377-80.

Pham, T., Drew, H.D., Mosely, S.H., and Liu, J.Z., 1990, 'Infrared Absorptivity of $YBa_2Cu_3O_{7-x}$ Crystals,' *Physical Review B*, Vol. 41, pp. 11681-84.

Pipard, A.B., 1947, 'The Surface Impedance of Superconductors and Normal Metals at High Frequencies II. The Anomalous Skin Effect in Normal Metals,' *Proceedings of the Royal Society*, Vol. A191, pp. 385-399.

Polder, D., and Van Hove, M., 1971, 'Theory of Radiative Heat Transfer between Closely Spaced Bodies,' *Physical Review B*, Vol. 4, pp. 3303-3314.

Press, W.H., Flannery, B.P., Teukolsky, S.A., and Wetterling, W.T., 1986, *Numerical Recipes*, Cambridge University Press, Cambridge.

Quinlan, S.M., Hirschfeld, P.J., and Scalapino, D.J., 1996, 'Infrared Conductivity of a $d_{x^2-y^2}$-Wave Superconductor with Impurity and Spin Fluctuation Scattering,' *Physical Review B*, Vol. 53, pp. 8575-82.

Randall, C.M., and Rawcliffe, R.D., 1967, 'Refractive Indices of Germanium, Silicon, and Fused Quartz in the Far Infrared,' *Applied Optics*, Vol. 6, pp. 1889-1895.

Renk, K.F., 1992, 'Far-Infrared Spectroscopy of High Temperature Superconductors,' in *Studies of High Temperature Superconductors*, A.V. Narlikar, Ed., Nova Science Publishers, New York, Vol. 10.

Renk, K.F., Betz, J., Schützmann, J., Prückl, A., Brunner, B., and Lengfellner, H., 1990, 'Use of High-T_c Superconductors for Far-Infrared Fabry-Perot Resonators,' *Applied Physics Letters*, Vol. 57, pp. 2148-2149.

Renk,K.F., and Genzel, L., 1962, 'Interference Filters and Fabry-Perot Interferometers for the Far Infrared,' *Applied Optics*, Vol. 1, pp. 643-648.

Renk, K.F., Ose, W., Zetterer, T., Schützmann, J., Lengfellner, H., Otto, H.H., Keller, J., 1989, 'Far Infrared Reflectivity of $Tl_2Ba_2CaCu_2O_8$ and $YBa_2Cu_3O_7$ Ceramics and of an Oriented $YBa_2Cu_3O_7$ Thin Film,' *Infrared Physics*, Vol. 29, pp. 791-798.

Reuter, G.H.E., and Sondheimer, E.H., 1948, 'The Anomalous Skin Effect in Metals,' *Proceedings of the Royal Society,*, Vol. A195, pp. 336-364.

Ruvalds, J., 1996, 'Theory Prospects for High Temperature Superconductors,' *Superconductor Science & Technology*, Vol. 9, pp. 1-42.

Rose-Innes, A.C., and Rhoderick, E.H., 1978, *Introduction to Superconductivity*, Second Edition, Pregamon Press, New York.

Sakai, K., and Genzel, L., 1983, 'Far Infrared Metal Mesh Filters and Fabry-Perot Interferometry,' in *Review of Infrared and Millimeter Waves*, Vol. 1, K.J. Button, Ed., Plenum Press: New York, pp. 155-247.

Scalapino, D.J., 1995, 'The Case for $d_{x^2-y^2}$ Pairing in the Cuprate Superconductors,' *Physics Reports*, Vol. 250, pp. 329-365.

Schlesinger, Z., Collins, R.T., Holtzberg, F., Feild, C., Koren, G., Gupta, A., 1990, 'Infrared Studies of the Superconducting Energy Gap and Normal-State Dynamics of the High-T_c Superconductor $YBa_2Cu_3O_7$,' *Physical Review B*, Vol. 41, pp. 11237-259.

Shen, Z.-X., Spicer, W.E., King, D.M., Dessau, D.S., and Wells, B.O., 1995, 'Photoemission Studies of High-T_c Superconductors: The Superconducting Gap,' *Science*, Vol. 267, pp. 343-350.

Siegel, R., and Howell, J.R., 1992, *Thermal Radiation Heat Transfer*, Hemisphere Publishing Corporation, Washington, D.C.

Steel, W.H., 1967, *Interferometry*, Cambridge University Press, Cambridge, U.K.

Sun, A.G., Gajewski, D.A., Maple, M.B., Dynes, R.C., 1994, 'Observations of Josephson Pair Tunneling between a High-T_c Cuprate and a Conventional Superconductor (Pb),' *Physical Review Letters*, Vol. 70, pp. 2267-2270.

Tanner, D.B., Gao, F., Quijada, M., Romero, D.B., Rice, J.P., Ginsberg, D.M., Talvacchio, J., Forrester, M.G., Forro, L., Mandrus, D., Mihaly, L., Carr, G., Williams, G.P., 1992, 'Optical Conductivity of the High-T_c's Search for the Energy Gap,' *Journal of the Physics and Chemistry of Solids*, Vol. 53., pp. 1611-1618.

Tanner, D.B., and Timusk, T., 1992, 'Optical Properties of High-Temperature Superconductors,' in *Physical Properties of High-Temperature Superconductors*, D.M. Ginsberg, Ed., World Scientific Publishing Co., Singapore, Vol. 3, pp. 363-469.

Tarrio, C. and Schnatterly, S.E., 1988, 'Inelastic Electron Scattering in the High-T_c Compound $YBa_2Cu_3O_{7-x}$,' *Physical Review B*, Vol. 38, pp. 921-4.

Thomas, G.A., 1991, 'Opical Properties of Insulators and Metals with Copper Oxide Planes,' in *High Temperature Superconductivity, Proceedings of the 39th Scottish Universities Summer School in Physics*, D.P. Tunstall and W. Barford, Eds., Adam Hilger, Bristol, UK.

Timans, P.J., 1996, 'The Thermal Radiative Properties of Semiconductors,' in *Advances in Rapid Thermal and Integrated Processing*, F. Roozeboom, Ed., Kluwer Academic Publishers, The Netherlands, pp. 35-101.

Timusk, T., and Tanner, D.B., 1989, 'Infrared Properties of High-T_c Superconductors,' in *Physical Properties of High-Temperature Superconductors*, D.M. Ginsberg, Ed., World Scientific Publishing Co., Singapore, Vol. 1, pp. 339-407.

Tinkham, M., 1980, *Introduction to Superconductivity*, Robert E. Krieger Publishing Company, Malabar, FL.

Tinkham, M., 1970, 'Far Infrared Absorption in Superconductors,' in *Far-Infrared Properties of Solids*, S.S. Mitra and S. Nudelman, Eds., Plenum Press, New York, pp. 223-246.

Tolansky, S., 1948, *Multiple-Beam Interferometry of Surfaces and Films*, Oxford University Press, London, U.K.

Toscano, W.M., 1973, 'Thermal Radiative Properties of the Nobel Metals at Cryogenic Temperatures,' Ph.D. Thesis, Massachusetts Institute of Technology, Cambridge, MA.

Toscano, W.M., and Cravalho, E.G., 1976, 'Thermal Radiation Properties of the Nobel Metals at Cryogenic Temperatures,' *Journal of Heat Transfer*, Vol. 98, pp. 438-445.

Van Atta, C.M., 1965, *Vacuum Science and Engineering*, McGraw-Hill, New York.

Van Exter, M., and Grischkowsky D., 1990, 'Carrier Dynamics of Electrons and Holes in Moderately Doped Silicon,' *Physical Review B*, Vol. 41, pp. 12140-12149.

De Vaulchier, L.A., Vieren, J.P., El Azrak, A., Guldner, Y., Bontemps, N., Guilloux-Viry, M., Le Paven-Thivet, C., and Perrin, A., 1995, 'Penetration Depth in $YBa_2Cu_3O_7$ Thin Films from Far-Infrared Transmission,' *Physical Review B*, Vol. 52, pp. 564-569.

Vaughan, J.M., 1989, *The Fabry-Pérot Interferometer, History, Theory, Practice, and Applications*, Adam Hilger, Bristol, U.K.

Wagner, G. and Habermeier, H.-U., 1994, 'Substrate Heating and Temperature Measurement for High-T_c Thin Film Preparation,' *Physica C*, Vol. 235-240, pp. 637-8.

Watanabe, Y., Wang, Z.Z., Lyon, S.A., Tsui, D.C., Ong, N.P., Tarascon, J.M., Barboux, P., 1989, 'Mid-Infrared Reflectivity and Ellipsometry Measurements on Single-Crystal $YBa_2Cu_3O_7$ and $Bi_2Sr_2CuO_{6+y}$,' *Physical Review B*, Vol. 40, pp. 6884-89.

Weaver, J.H., 1981, 'Optical Properties of Gold,' in *Physics Data, Optical Properties of Metals, Part I: The Transition Metals*, J.H. Weaver, C. Krafka, D.W. Lynch, and E.E. Koch, Eds., Fachinformationszentrum, Karlsruhe, Germany.

Wiese, P., Riederer, X., Schützmann, J., Gorshunov, B., Betz, J., and Renk, K.F., 1992, 'Far-Infrared Fabry-Perot Filter of High Transmission with High-T_c Superconductor Reflectors,' *International Journal of Infrared & Millimeter Waves*, Vol. 13, pp. 65-70.

Wilson, A. H., 1953, *The Theory of Metals*, Cambridge Press, London.

Wooten, F., 1972, *Optical Properties of Solids*, Academic Press, New York.

Yeh, P., 1988, *Optical Waves in Layered Media*, John Wiley & Sons, New York.

Zeller, A.F., 1990, 'High-T_c Superconductors as Thermal Radiation Shields,' *Cryogenics*, Vol. 30, pp. 545-546.

Zhang, Z.M., Choi, B.I., Le, T.A., Flik, M.I., Siegal, M.P., Phillips, J.M., 1992, 'Infrared Refractive Index of Thin $YBa_2Cu_3O_7$ Superconducting Films,' *Journal of Heat Transfer*, Vol. 114, pp. 644-652.

Zhang, Z.M., Le, T.A., Flik, M.I., and Cravalho, E.G., 1994, 'Infrared Optical Constants of the High-T_c Superconductor $YBa_2Cu_3O_7$,' *Journal of Heat Transfer*, Vol. 116, pp.253-7.

Zhu, Y., Suenaga, M., and Xu, Y., 1990, 'TEM Studies on Twin Boundaries in $YBa_2Cu_3O_7$ and $YBa_2(Cu_{0.98}M_{0.02})_3O_7$ (M = Zn,Al),' *Journal of Materials Research*, Vol. 5, pp. 1380-1387.

Ziman, J.M., 1963, *Electrons and Phonons: The Theory of Transport Phenomena in Solids*, Oxford University Press, London.

Zimmermann, W., Brandt, E.H., Bauer, M., Seider, E., and Genzel, L., 1991, 'Optical Conductivity of BCS Superconductors with Arbitrary Purity,' *Physica C*, Vol. 183, pp. 99-104.